Extending the Modelling Framework for Gas-Particle Systems

Applications of Multiparameter Shape Descriptions to Non-Conventional Solid Fuels in Reacting and Non-Reacting Environments

Rosendahl, Lasse Aistrup

Publication date:
1998

Document Version
Publisher's PDF, also known as Version of record

Extending the modelling framework for gas-particle systems

Applications of multiparameter shape descriptions to non-conventional solid fuels in reacting and non-reacting environments

Lasse Rosendahl
Institute of Energy Technology
Aalborg University, Denmark
e-mail: lar@iet.auc.dk

ISBN 87-89179-25-0

This report was typeset in LaTeX using the WinTeX 95 editing environment.

November 1998

Abstract

An extended Lagrangian particle tracking and combustion model for non-conventional solid fuels such as chopped straw has been developed. Based on an extension of the existing tracking techniques, shapes are based on a superelliptic equation capable of assuming forms ranging from spheres to cylinders, through simple parameter variation. Using a concept of aerodynamical similarity, a drag coefficient accounting for orientability as well as shape variations has been defined.

The model has been applied to two isothermal testcases, where different types of particles are injected into swirling flow configurations. In both cases, the model performs efficiently, and indicates a pronounced difference in terms of the aerodynamic properties of the different particle shapes. For validation purposes, terminal velocity predictions of different shapes have been carried out, and compared to experimental data, with very good results.

Single particle combustion has been tested using a number of different particle combustion models applied to coal and straw particles. Comparing the results of these calculations to measurements on straw burnout, the results indicate that for straw, existing heterogeneous combustion models perform well, and may be used in high temperature ranges.

Finally, the particle tracking and combustion model is applied to an existing coal and straw co- fuelled burner. The results indicate that again, the straw follows very different trajectories than the coal particles, and also that burnout occurs a different locations, as the straw is not re-entrained into the flame zone.

Dansk Synopsis

Denne rapport omhandler udvikling af en udviddet Lagrange model for simulering af partikel-gas systemer, hvor partiklerne ikke kan beskrives som sfæriske. En superelliptisk form funktion anvendes til beskrivelse af partikelformen, der kan variere fra sfærisk til cylindrisk ved simpel parametervariation. Baseret på en antagelse om aerodynamisk ligedannethed, er formuleringen af drag coefficienten udviddet til at omfatte såvel orientabilitet som form ændringer indenfor den superelliptiske form.

Modellen er anvendt på to isoterme testcases, hvor forskellige superellipser trackes i roterende strømninger. Resultaterne herfra viser store forskellige i de aerodynamiske egenskaber af de forskelligt formede partikler. Terminal hastighedsberegninger er også foretaget for generelle superellipser, og med stort sammenfald sammenlignet med eksperimentelle data. Ydermere er udbrændingsberegninger på kul og halm foretaget med eksisterende udbrændingsmodeller, og sammenlignet med forsøgsdata for halm. Resultaterne indikerer, at disse modeller er anvendelige selv på ikke-konventionelle brændsler.

Endeligt er modellen anvendt på en eksisterende combi-brænder, fyret med kul og halm. Igen ses de aerodynamiske egenskaber at have indflydelse på udbrændingsforøbet af halmen, idet halmen følger væsentligt forskellige trajektorier end kulpartiklerne, og ikke bliver ført tilbage i flammezonen for endelig udbrænding.

Preface

This report is submitted in partial fulfilment of the requirements for the Danish Ph.D. degree. It covers research work at the Institute of Energy Technology, Aalborg University, during the period december 1994 to june 1998. The work has been carried out under the supervision of Dr. Thomas Condra, associate professor and senior research engineer Poul Knudsen, ELSAMPRJOEKT A/S, and has been co-funded by I/S ELSAM and the Institute of Energy Technology, Aalborg University.

During the course of the work, inspiration and help has been unselfishly given by many people. In particular, I'd like to thank Dr. Jan Rusaas, Haldor Topsø A/S, for his honest criticism and our many fruitful discussions during his time at the Institute of Energy Technology. Also Søren Knudsen Kær deserves special thanks, for his efforts on the CFD simulation of the MKS1 and Risø furnaces.

The CFD part of this work has been based on the CFX (formerly: CFDS-FLOW3D) suite of programmes from AEA Technology plc, Harwell, United Kingdom, which is made available to the Institute of Energy Technology through an academic license. The numerical models developed in this work are implemented in the separate Lagrangian particle tracking and combustion utility PCOMBUST . A full documentation of this code can be found in Rosendahl (1996b).

During the Ph.D. project period, I spent a trimester under the EUROFLAM programme at the Thermal Research Centre of ENEL, Pisa, Italy, working on CFD modelling of a co-fuelled burner using the commercial CFD code FLUENT. This is documented in a seperate report (Rosendahl 1996a).

Report structure

Chapter 1 introduces biomass as a fuel for energy production, as well as the fundamental modelling concepts used in the report, and discusses the main differences between standard fuels and biomass as applies to modelling. Chapter 2 and 3 contain the main modelling framework, the former, which is the main section of the report, in terms of particle tracking, the latter of particle combustion. Chapter 4 and 5 apply the aerodynamic and combustion models to different types of single particles, in order to validate and discuss the use of these. Chapter 6, 7 and 8 contain the testcases of this work. The first two are iso-thermal, whereas the last is a fully coupled reacting flow.

Appendix A gives an overview of the modelling approaches to non-spherical particle modelling, Appendix B details the implementation of the models into PCOMBUST and Appendix C, D and E outline some mathematical techiques used in this work. Appendix F contains theoretical burn out times of fuel particles. The experimental LSV work done for the project is presented in Appendix G, and finally examples of the output from PCOMBUST are given in Appendix H, followed by a list of publications in Appendix I.

Throughout the duration of this work, my family - Rete, Mikkel and Jonathan - have been a constant proof that not all aspects of life conform to the superelliptic shape formulation - for that I'm very grateful.

Lasse Rosendahl, M.Sc. Mech.Eng.
Aalborg, 1998

Contents

1 Introduction **1**

1.1 Problem statement 2

1.2 The role of CFD in furnace design 3

1.2.1 CFD fundamentals 3

1.2.2 Gas-particle systems 4

1.3 Modelling solid fuels with CFD 6

1.4 Fuel characterisation 7

2 Particle motion **11**

2.1 Generalized equations of motion 12

2.2 Orientability and coordinate systems 13

2.2.1 Particle axes orientation 14

2.3 A general class of particles 16

2.3.1 Areas 17

2.3.2 Constraints and assumptions of the model 18

2.4 Aerodynamic properties of superelliptic particles 18

2.4.1 Aerodynamic response times 20

2.4.2 Drag forces 22

2.4.3 Lift forces . . . 27
2.4.4 Body forces . . . 30
2.4.5 Torques . . . 31
2.5 Interaction of particles and fluid structures . . . 33
2.5.1 Turbulent dispersion . . . 33
2.5.2 Large particles subject to local fluid structures . . . 36
2.6 Influence of combustion on particle aerodynamics . . . 38
2.7 Non-spherical particle tracking methodology . . . 38
2.8 Summary . . . 39

3 Particle combustion 41

3.1 Devolatilization . . . 42
3.1.1 Single equation Arrhenius pyrolysis model . . . 42
3.1.2 Distributed Activation Energy (DAE) model . . . 43
3.2 Solid combustion . . . 43
3.2.1 Mixed control model . . . 44
3.2.2 Gibb's model . . . 45
3.2.3 Reactivity index model . . . 46
3.3 Combustion products . . . 47
3.4 Stefan flow . . . 47
3.5 Diameter changes . . . 49
3.5.1 Swelling . . . 49
3.5.2 The extended shrinking core model . . . 50
3.6 Active surface correction . . . 51
3.7 Heat balance . . . 52

3.8 Gas phase combustion 53
3.8.1 Gas phase source terms - EDC kinetic model 54
3.8.2 Homogeneous reaction kinetics 55
3.8.3 Overall homogeneous reaction rate 56
3.9 Summary 56

4 Terminal velocity calculations 57

4.1 Determination of terminal velocity 58
4.2 Stability of orientation 60
4.3 Summary 63

5 Single particle combustion 65

5.1 Burnout profiles 66
5.2 Theoretical burnout time 71

6 Testcase: AAU/DTU isothermal test rig 73

6.1 Inlet conditions 73
6.1.1 Inlet conditions for small particles 73
6.1.2 Inlet conditions for large particles 74
6.2 Computational configuration 75
6.2.1 Mesh and physical models 75
6.3 CFD results 76
6.4 LDA measurements 78
6.5 Particle trajectories 78
6.5.1 Small particles 78
6.5.2 Large particles 79

6.6 Summary 80

7 Testcase: Risø tunnel furnace 83

7.1 Standard operating conditions 83

7.2 Computational configuration 83

7.3 Dispersed phase boundary conditions 85

7.4 Results 86

7.4.1 Flow patterns 86

7.4.2 Particle trajectories 87

7.5 Summary 90

8 Testcase: MKS1 single combined burner 91

8.1 Standard operating conditions 91

8.2 Model configuration 91

8.2.1 Computational configuration 92

8.2.2 Dispersed phase boundary conditions 93

8.3 Results 95

8.3.1 Isothermal flow patterns in coal and combined burners 95

8.3.2 Coupled flow patterns 96

8.3.3 Particle trajectories 96

8.3.4 Particle combustion patterns 97

8.4 Summary 97

9 Conclusions and Perspective 101

APPENDICES

A Approaches to non- spherical particle modelling 109

A.1 The ellipsoid at Stokes conditions 109

A.2 Disks and octahedrons 111

A.3 The 2D ellipsoid under general flow conditions 113

A.3.1 Force definition 113

A.3.2 Torque definition 115

B Simulation methodology 117

B.1 Particle area and volume 117

B.2 Coordinate systems 119

B.2.1 Cartesian coordinates 119

B.2.2 The topological coordinate system 120

B.2.3 Local coordinates 120

B.3 Domain topology 121

B.3.1 Patches 122

B.4 Flow variable interpolation 122

B.5 Adaptive time stepping 125

B.6 Wall collisions 126

B.7 Calculating particle temperature 128

B.8 Particle ignition - initial combustion calculations 129

C Integrating the equations of motion 131

C.1 Translation and rotation 131

C.2 Position and orientation 133

D c_i for different models of motion 135

D.1 Ellipsoid 135

D.2 Superellipsoid 138

E Partial differentiation of numerical quantities 141

F Burnout times 143

F.1 All models, diffusion control 144

F.2 Mixed control model, kinetic control 144

F.3 Reactivity index model, kinetic control 144

G Laser Sheet analysis 145

G.1 Experimental setup 145

G.2 Numerical setup 147

G.3 Results 148

G.3.1 Experimental results 148

G.3.2 Numerical results 149

G.4 Summary 153

H Sample PCOMBUST command and log file 155

H.1 Command file 155

H.2 Log file 157

I List of publications and presentations 167

Nomenclature

Greek letters

α_i	Incidence angle	$[rad]$ or $[^o]$
α_{rim}	Exponent in Reactivity index model	$[-]$
β	Axis aspect ratio	$[-]$
γ	Particle swelling index	$[-]$
ε	Turbulent dissipation	$[m^2/s^3]$
	Emissivity	$[-]$
ε_{Gk}	Particle void fraction	$[-]$
ϵ_0	Initial particle porosity	$[-]$
θ_{ij}	Direction cosine	$[rad]$
λ	$\frac{\pi}{2} - \alpha_i$	$[rad]$
	Heat transfer coefficient	$[W/m^2K]$
μ_g	Molecular viscosity	$[kg/ms]$
μ_t	Turbulent viscosity	$[kg/ms]$
μ_{eff}	Effective viscosity	$[kg/ms]$
ν_g	Kinematic viscosity	$[m^2/s]$
ρ_C	Fixed carbon density	$[kg/m^]$
ρ_g	Gas density	$[kg/m^3]$
ρ_{O_2}	Oxygen density	$[kg/m^3]$
ρ_p	Particle density	$[kg/m^3]$
σ	Stefan-Boltzmann's constant	$[W/m^2K^4]$
σ_t	Turbulent Prandtl number	$[-]$
τ_b	Burnout time	$[s]$
$\tau_{p,t}$	Particle translational response time	$[s]$
$\tau_{p,r}$	Particle rotational response time	$[s]$
τ_s	System time scale	$[s]$
ϕ	Dependent variable	
	Sphericity	$[-]$
	Stoichiometry factor	$[-]$
$\vec{\omega}_i$	Angular velocity in co-rotational system	$[rad/s]$
Γ	Diffusion coefficient	$[kg/ms]$
$\vec{\Omega}_i$	Angular velocity in inertial system	$[rad/s]$

Roman letters

a	Particle minor semi-axis	$[m]$
a_{rim}	Constant in Reactivity index model	$[-]$
b	Particle major semi-axis	$[m]$
b_{rim}	Constant in Reactivity index model	$[-]$
b'	Non-dimensional mass transfer parameter	$[-]$
c_i	Coefficients in equation of motion	
c_p	Specific heat capacity	$[J/kgK]$
d_*	Non-dimensional particle diameter (eq. 4.5)	$[-]$
d_p	Particle diameter	$[m]$
$\bar{d}_p$	Equivalent particle diameter (eq. 3.4)	$[m]$
f	Drag correlation factor	$[-]$
	Oscillation frequency	$[Hz]$
	$\frac{CO}{CO_2}$ ratio	$[-]$
f_o	Mass fraction of oxygen in oxidant	$[-]$
f_{sel}	Superelliptic drag correlation factor	$[-]$
$f_{1\beta}, f_{2\beta}$	Superelliptic drag correlation factors	$[-]$
f_β	Lift force factor	$[-]$
f_n	Superelliptic drag correlation factor	$[-]$
$\vec{g}$	Gravity vector	$[m/s^2]$
h_{fg}	Volatile latent heat	$[J/kg]$
i	Stoichiometric reaction ratio	$[-]$
k	Turbulent kinetic energy	$[m^2/s^2]$
	Heating rate	$[K/s]$
k_0	Frequency factor	$[s^{-1}]$
l_e	Dissipation length scale	$[m]$
m_c	Mass of char in particle	$[kg]$
m_v	Mass of volatiles in particle	$[kg]$
m_a	Mass of ash in particle	$[kg]$
m_w	Mass of water in particle	$[kg]$
m_p	Particle mass	$[kg]$
m_F	Mass fraction of gaseous fuel	$[-]$
m_{O_2}	Mass fraction of oxygen in oxidant	$[-]$
m_{CO}	Mass fraction of CO	$[-]$
n	Superelliptic exponent	$[-]$
n_a, n_b, n_c	Homogeneous reaction constants	$[-]$
p_{dyn}	Dynamic pressure	$[Pa]$
p_{O_2}	Oxygen partial pressure	$[Pa]$
t	Time	$[s]$
t_e	Eddy lifetime	$[s]$
t_t	Eddy transit time	$[s]$
$\vec{u}_g$	Gas velocity vector	$[m/s]$
u_r	Relative (slip) velocity between particle and gas	$[m/s]$
u_t	Terminal velocity	$m/s]$
u_*	dimensionless terminal velocity	$[-]$
$\vec{v}_p$	Particle velocity vector	$[m/s]$
x_{cp}	Distance from centre of mass to centre of pressure (eq. 2.48)	$[m]$
z_{pg}	Fraction of heat remaining in particle (eq. 3.38)	$[-]$
A_p	Projected area	$[m^2]$
A_s	Surface area	$[m^2]$
$A_{\alpha i}$	In-line area	$[m^2]$
A_k	Kinetic reaction pre-exponential factor	$[kg/(m^2 sPa)]$

Roman letters cont'd

A_v	Devolatlisation pre-exponential factor	$[s^{-1}]$
C_μ	Constant in $k-\varepsilon$ turbulence model	
C_D	Drag coefficient	$[-]$
C_L	Lift coefficient	$[-]$
C_N	Normal force coefficient	$[-]$
D	Diffusion coefficient (eq. 3.9)	$[m^2/s]$
	Cylinder diameter	$[m]$
E_v	Devolatilisation activation energy	$[J/kg]$
E_k	Kinetic reaction activation energy	$[J/kg]$
E_Γ	Activation energy for $\frac{CO}{CO_2}$ ratio	$[J/kg]$
E_{rim}	Reactivity index activation energy	$[J/kg]$
$\vec{F}$	Force vector	$[N]$
$\vec{F}_{buoy}$	Buoyancy force	$[N]$
$\vec{F_D}$	Drag force vector	$[N]$
$\vec{F}_{\bar{D}}$	Mean drag force	$[N]$
$\vec{F}_g$	Gravity force	$[N]$
$\vec{F}_{\nabla P}$	Pressure gradient force	$[N]$
$\vec{F_L}$	Lift force vector	$[N]$
$\vec{F_N}$	Normal force vector	$[N]$
H_{reac}	Heat of reaction for char+oxygen reaction	$[J/kg]$
I_i	Moment of inertia, $i=[x',y',z']$	$[kgm^2]$
I_p	Radiative flux	$[W/m^2]$
J_0	Total gas flux at particle surface	$[kg/m^2s]$
J_t	Gas flux	$[kg/m^2s]$
K_1	Constant in simplified drag coefficient (eq. 4.7)	$[-]$
K_ω	Constant in viscous torque formulation	$[-]$
K_v	Devolatilisation rate	$[s^{-1}]$
K_k	Kinetic char oxidation rate (eq. 3.5 or 3.6)	$[kg/m^2sPa]$
	Kinetic char oxidation rate (eq. 3.12)	$[K/s]$
K_D	Diffusion rate (eq. 3.7)	$[kg/(m^2sPa)]$
K_{Gk}	Internal diffusion and reaction rate (eq. 3.13)	$[s^{-1}]$
L_{char}	Characteristic geometric length scale	$[m]$
L_h	Turbulent length scale	$[m]$
M_C	Carbon molecular mass	$[kg/kmol]$
M_F	Gaseous fuel molecular mass	$[kg/kmol]$
P	Pressure	$[Pa]$
	Period of oscillation	$[s]$
$\dot{Q}_{rad}$	Radiative heat flux	$[W/m^2]$
R_C	Carbon gas constant	$[J/kgK]$
R_v	Volatile gas constant	$[J/kgK]$
R_{ref}	Reference profile for random grain (eq. 3.17) or pore (eq. 3.18) model	$[-]$
S_{act}	Active surface factor (eq. 3.34)	$[-]$
S_{EDC}	Eddy Dissipation mixing rate (eq. 3.43)	$[kg/m^3s]$
$\vec{T}$	Particle torque	$[Nm]$
T_p	Particle temperature	$[K]$
T_m	Mean boundary layer temperature	$[K]$
$\vec{T}_{viscous}$	Viscous torque	$[Nm]$
$\vec{T}_{\nabla u}$	Torque cause by macroscopic velocity gradients	$[Nm]$
$\vec{T}_{pitch}$	Pitching moment	$[Nm]$
V	Volatile content	$[kg/kg]$
V_p	Particle volume	$[m^3]$
X	Degree of conversion	$[-]$

Chapter 1

Introduction

Når de store elektron-regnemaskiner ikke arbejder med konkrete opgaver, står de og tænker på tal i al almindelighed.
Piet Hein

In recent years, attention has focused increasingly on man's use of energy as well as the means of energy production available and their consequences. Phenomena such as the greenhouse effect, ozone layer depletion and acid rain have become accepted facts of life and common household terms.

One of the main greenhouse gases is carbon dioxide, CO_2. CO_2 is an unavoidable product of any form of combustion involving fossil and bio-fuels, and, as such material forms the main basis of the worlds non-nuclear energy production, CO_2 reduction has become not only a technical issue, but very much also a political one. Thus, a number of new technologies have been initiated, or sustained through their maturing process, by political initiative, and amongst these ranks the use of so-called "CO_2-neutral" biofuels in energy production. The characteristic of these fuels is, that the amount of CO_2 emitted during combustion corresponds to that absorbed during the growth of the biofuel, thereby not increasing the amount of CO_2 in the atmosphere[1].

In 1992, the Danish government imposed upon the power utilities ELKRAFT (responsible for the eastern part of Denmark) and ELSAM (responsible for the central and western parts of Denmark), that by the year 2000, 1.2 million tons of straw and 200,000 tons of wood chips were to be used annually as fuel. Furthermore, the power utilities were obliged to reduce CO_2 emissions by 20% relative to the 1988-level by 2005. In order to comply with this, ELSAM and ELKRAFT have taken several initiatives, both in the design of new plants but also in retrofitting existing plants with equipment to be able to handle biofuels. For ELSAM, the main initiatives have been:

[1]This is only strictly true when considering the combustion of the biofuel as an isolated event; preparation and transportation of the fuel from the field to the power plant should also strictly be considered.

- Full-scale testing of chopped straw and pulverised coal co-firing, MIDTKRAFT ENERGY COMPANY, 1996-1998.
  Retrofitting of an existing full-scale 150 MW utility boiler with modified burners, enabling the co-firing of up to 20% straw (by energy) and pulverised coal.

- Construction and commissioning of straw and wood chip fired plant, Sønderjyllands Højspændingsværk, 1997.

- Proposal of a straw and coal co-fired CFB plant, MIDTKRAFT ENERGY COMPANY.
  Proposal rejected by the Danish Department of Energy, 1997, due to the partial coal basis and the moratorium of new coal plants.

- Participation in the Interflow project, MIDTKRAFT ENERGY COMPANY, 1996-1998.
  Numerical analysis of the fouling of heat exchanger surfaces when firing straw. Conducted at the Danish Maritime Institute, Copenhagen.

- Funding academic work to develop suitable models for the simulation of biofuels in Computational Fluid Dynamics (CFD).
  The funding covers the work documented in this report as well as work done by the CHEC[2] group on chemical modelling of biofuel combustion, the Danish Institute of Biotechnology and the Department of Combustion Research, Risø National Laboratory, on biofuel characterisation.

1.1 Problem statement

It is the purpose of the current work to bridge the modelling gap between the different fuels in terms of developing a model, within the Lagrangian framework of gas-particle systems, general enough to be able to account for the different aerodynamic properties of these fuels, and apply this model to characteristic reacting environments in order that our knowledge concerning the co-combustion of diverse fuels may increase.

In the following sections, the fundamentals of the Computational Fluid Dynamics technique as well as the common models used in gas-particle systems and solid fuel modelling is outlined, with emphasis on the use of biofuels such as chopped straw, in order to provide the basic foundation of the new models developed in this report.

[2]Centre for Combustion and Harmful Emission Control, Institute of Chemical Engineering, Technical University of Denmark.

1.2 The role of CFD in furnace design

Computational Fluid Dynamics has been developing since the early 1970's, to have become in the 1990's a real analysis tool in furnace design, supplementing and in some cases even replacing, expensive test rigs. This "coming of age" can be attributed to a number of factors, not least of which is the incredible increase in sheer computer power seen during this decade. Numerical algorithms have improved, as have the physical models describing fluid motion as well as chemical reactions, gas-particle interaction, radiation, and finally, geometry handling has come from command file driven mesh generation to state-of-the-art GUI/CAD[3]-based mesh generation.

1.2.1 CFD fundamentals

Although it is beyond the scope of this work to detail the basis of CFD, a short introduction will be given here[4], based on the finite volume method. A more complete description of the CFD-basis for the current work is given in chapters 6-8.

Two basic approaches to CFD exist, the finite element approach and the finite volume approach. Principaly, both divide the flow-domain up into a number of small control volumes or elements (as shown in figure 1.1), but whereas the finite element technique concentrates on solving the governing equations in the grid points, the finite volume method integrates these over a control volume, and supplies the solution at the centre of these volumes. Of the two approaches, it is the finite volume method which has become most popular and used, and it is also the approach used in the current work to solve for the fluid phase.

The governing equations are generally termed transport equations, although for the special case of the velocity components, they are known as the Navier-Stokes equations:

$$\underbrace{\rho_g \frac{\partial \phi}{\partial t}}_{Time\ dependent\ term} + \underbrace{\nabla(\rho_g \vec{u}_g \phi)}_{Convective\ term} - \underbrace{\nabla\left(\frac{\mu_{eff}}{Pr}\nabla\phi\right)}_{Diffusive\ term} = \underbrace{S}_{Source\ term} \tag{1.1}$$

ρ_g: fluid density $[kg/m^3]$

t: time $[s]$

$\vec{u}$: flow velocity vector $[m/s]$

μ_{eff}: effektive viscosity ($\mu_{laminar} + \mu_{turbulent}$) $[kgm/s]$

Pr: Prandtl number $[-]$

ϕ: dependent variable (i.e. the quantity being solved for). ϕ can take on velocity components, temperature, chemical species, turbulent quantities etc.

The solution process becomes one of iteration, as equation 1.1 for most engineering flows cannot be solved analytically due to its non-linearity (the convective term). Equation

[3]Graphical User Interface and Computer Aided Design

[4]For the interested reader, the book by Versteeg and Malalasekera (1995) is recommended.

1.1 is therefore transformed to a set of algebraic equations of the form (in 2D)

$$a_N\phi_N + a_S\phi_S + a_W\phi_W + a_E\phi_E + S_u = a_P\phi_P \tag{1.2}$$

forming a so-called "amoeba" or "molecule", which is valid for each node in the domain (figure 1.2). This transformation, or discretisation, is based on a so-called difference scheme, relating cell-face fluxes across the computational mesh. These schemes can vary in complexity and accuracy, and care must be taken selecting an appropriate difference scheme for the flow to be solved.

Using various solution techniques, the system of equations is solved iteratively, until the residual error has reached an acceptable level, whence the iteration process has reached a converged solution.

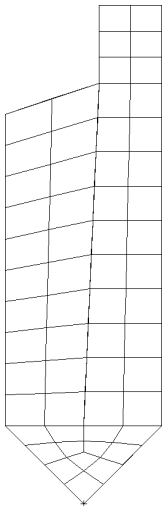

Figure 1.1: Schematic of a 2D structured mesh in a typical industrial furnace. The element size shown here is exaggerated for clarity.

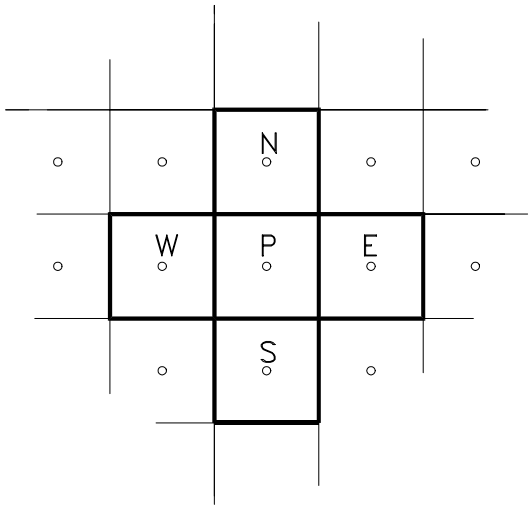

Figure 1.2: Schematic of a simple "amoeba" or "molecule" used to determine the value of ϕ at point P. More complex differencing schemes use more complex amoebas, with more neighbouring volumes, to determine ϕ at point P.

1.2.2 Gas-particle systems

Using CFD in the context of furnace design falls into the general category of gas-particle systems, characterized by two distinct phases, the gas -continuous - phase and the particle - dispersed - phase. Two main approaches to the simulation of such systems, the Euler/Euler and Euler/Lagrange methods, have become generally accepted. As the names indicate, it is not in the formulation of the continuous phase that the models differ - here both use the Euler, or field, formulation. It is in the formulation of the dispersed phase that the models differ, by applying either a field formulation once again, or by tracking representative particles as they move around in the flow domain.

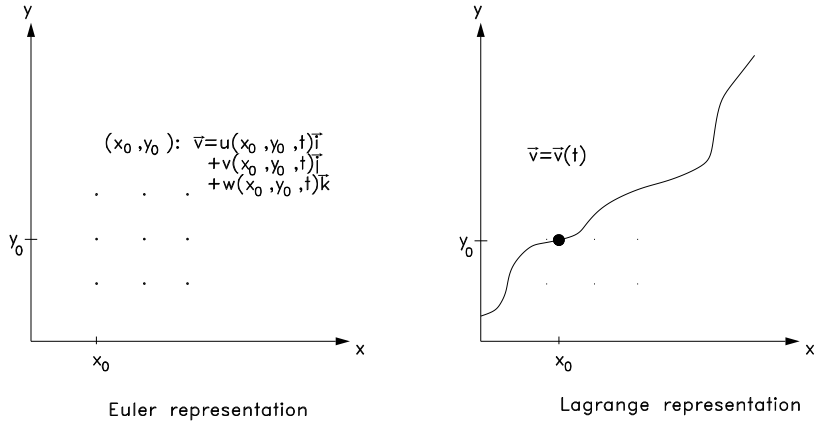

Figure 1.3: Schematics of the difference in using the Euler and Lagrange formulations.

The Euler/Euler method treats both phases as continua, and solves for the motion of the phases in an inertial frame of reference, describing this using a field formulation (see figure 1.3, left):

$$\vec{v} = u[x(t), y(t), z(t), t]\vec{i} + v[x(t), y(t), z(t), t]\vec{j} + w[x(t), y(t), z(t), t]\vec{k} \tag{1.3}$$

and

$$\vec{a} = \frac{\partial \vec{v}}{\partial t} + u\frac{\partial \vec{v}}{\partial x} + v\frac{\partial \vec{v}}{\partial y} + w\frac{\partial \vec{v}}{\partial z} \tag{1.4}$$

$\vec{i}, \vec{j}, \vec{k}$: unit coordinate vectors

u, v, w: cartesian velocity components $[m/s]$

This method is suitable for high particle concentrations, where the particle phase can be considered continuous due to the relative proximity of neighbouring particles. For systems with a wide spectrum of particle sizes, the Euler/Euler method becomes very costly, because a transport equation needs to be set up for each size class, with subsequent need for discretization and linearisation. Furthermore, formulating an Euler description of the interface between two reacting phases is very complicated, though examples of such formulations do exist, e.g. Simonin (1996).

The Euler/Lagrange method is perhaps the most widely used model of the two in the current context. Here, only the continuous phase is treated as such and solved through discretization. The dispersed phase, characterized by relatively distant neighbouring particles, is solved by tracking a number of discrete, representative particle streams through the geometry, and monitoring their effect on the continuous phase and vice versa along the way (see figure 1.3, right). The change in particle composition, diameter, temperature etc. is readily obtained by applying suitable models for the different combustion processes. The relative ease of implementation and high level of information regarding single particle as well as global combustion characteristics, coupled with the

computational cost effectiveness of the Lagrangian description, has made it common in furnace applications.

1.3 Modelling solid fuels with CFD

Solid fuels, or more generally, gas-particle systems, have been modelled with CFD for several years, and the models describing the different sub-processes date back several decades. The most commonly used solid fuel is pulverised coal, hence this fuel has received the greatest attention, both from a chemical standpoint, but also in terms of more engineering-oriented models suitable for modelling of large systems. Very standardised models exist for devolatilisation, evaporation and char combustion, which are the dominant processes in pulverised coal combustion (see figure 1.4), and an almost universal assumption is that coal dust particles are spherical and homogeneous.

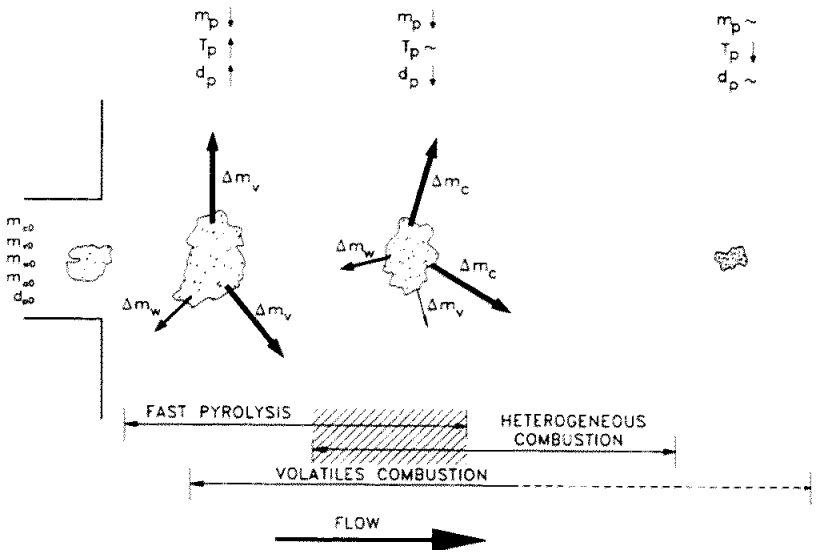

Figure 1.4: Schematic of the processes occuring as a coal particle enters a furnace. As the particle heats up, devolatilization and evaporation occurs. The volatile gases burn in the vicinity of the coal particle, and when the particle has reached a high enough temperature, it ignites and burns. From Zachariassen & Rosendahl (1994).

Also from an aerodynamical standpoint, coal dust lends itself to a spherical description, simplifying the equations of motion considerably due to the lack of orientability. This assumption is not entirely unreasonable when considering coal dust, as can be seen in figure 1.5.

With the increased focus on environmental aspects of power generation, focus has shifted from standard to alternative fuels, such as straw, wood chips or pellets, waste,

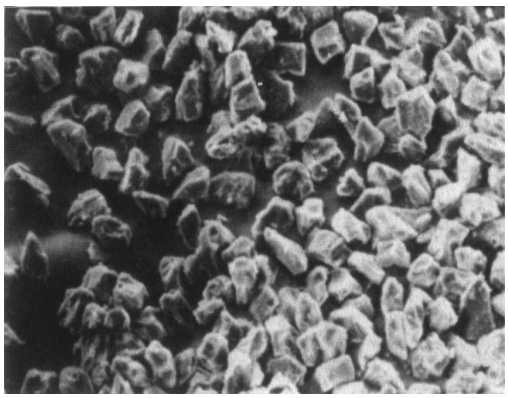

Figure 1.5: Pulverised coal shown enlarged. (Smoot and Smith 1985).

Figure 1.6: Chopped straw from the Studstrup power plant. The specimen is typical in its structure, with a knee at one end, and a crushed straw tube at the other.

sewage sludge, etc., and new models have to be developed, where the existing models can be shown to fail. Considering the case of straw (see figure 1.6), it is obvious that the aerodynamics of these particles are very different from those of coal dust. A further typical characteristic of biofuels is that they are not homogeneous, and their chemical constituents are present in amounts and species very different from those of coal. Even amongst themselves, the "mean biofuel", although theoretically defineable, represents something which doesn't exist, and therefore combustion models for biofuels will have to be somewhat more diverse, and something to be improved upon.

1.4 Fuel characterisation

A requirement for succesful modelling of the combustion of any fuel is knowledge of its chemical composition, heating value, moisture and volatile content. These are determined by laboratory analysis, and presented as either an ultimate analysis, with detailed analysis on all chemical species found in any significant amount, or a proximate analysis, with information on the contents of moisture, volatiles, char and ash.

Comparison between the normal fuels, i.e. coal, and the alternative fuels such as wood and straw shows large differences, not only in the chemical species present, but also in the amounts they are present in. Further complicating the determination of initial parameters for the fuel particles, is the differences even between the same type of biofuel. Rainfall, proximity to oceans and soil type plays an important role in the final composition of a biofuel. Ultimate analysis for Columbian Cerrejon coal and Danish wheat straw, and a comparison between a "mean" Danish straw and wood chips is shown in tables 1.1-1.2.

From an energy producing point of view, a more relevant basis for comparison is by referring the composition to the heating value of the fuel (see table 1.3). This gives a

	Columbian Cerrejon coal	Danish wheat straw
Effective heating value $[MJ/kg]$	27.56	15.82
Volatiles [% *mass*]	34.5	69.6
Hydrogen (H) [% *mass*]	4.7	5.2
Carbon (C) [% *mass*]	69.1	42.5
Ash [% *mass*]	10.8	5.8
Sulphur (S) [% *mass*]	0.88	0.15
Nitrogen (N) [% *mass*]	1.5	0.6
Chlorine (Cl) [% *mass*]	0.019	0.15
Silicon (Si) [% *dry mass*]	3.1	1.8
Aluminium (Al) [% *dry mass*]	1.1	0.054
Iron (Fe) [% *dry mass*]	0.62	0.086
Calcium (Ca) [% *dry mass*]	0.15	0.36
Magnesium (Mg) [% *dry mass*]	0.079	0.066
Sodium (Na) [% *dry mass*]	0.035	0.016
Potassium (K) [% *dry mass*]	0.19	0.7
Phosphorous (P) [% *dry mass*]	0.0087	0.067

Table 1.1: Heating values and composition of a typical coal used in Danish power plants and 1994 wheat straw. Notice that the unit changes from "as is" to dry mass.

	Wood chips	Straw
Effective heating value $[MJ/kg]$	19.4	17.9
Volatiles [% *mass*]	81.0	79.0
Hydrogen (H) [% *mass*]	5.8	6.3
Carbon (C) [% *mass*]	50.0	48.0
Ash [% *mass*]	1.0	4.0
Sulphur (S) [% *mass*]	0.05	0.15
Nitrogen (N) [% *mass*]	0.3	0.8
Chlorine (Cl) [% *mass*]	0.02	0.4
Silicon (Si) [% *mass*]	0.1	0.6
Aluminium (Al) [% *mass*]	0.015	0.005
Iron (Fe) [% *mass*]	0.015	0.01
Calcium (Ca) [% *mass*]	0.2	0.4
Magnesium (Mg) [% *mass*]	0.04	0.07
Sodium (Na) [% *mass*]	0.015	0.06
Potassium (K) [% *mass*]	0.1	0.9
Phosphorous (P) [% *mass*]	0.02	0.08

Table 1.2: Typical values of composition and heating values of wood chips and straw (ELSAMPROJEKT 1994).

clearer picture of the implications of using the different fuels.

	Wood chips	Straw	Coal
Ash	600	2300	3500
Sulphur (S)	30	90	400
Nitrogen (N)	200	450	500
Chlorine (Cl)	10	230	20
Sodium (Na)	10	30	20
Potassium (K)	60	500	50

Table 1.3: Composition values of wood chips (50% moisture), straw (15% moisture) and coal. Units: $[mg/MJ]$. (ELSAMPROJEKT 1994)

Evident from the above tables is that on an energy-production basis, straw is not without problems, containing much more Chlorine and Alkali than coal and wood chips. From a modelling standpoint, the differences in composition of the various types of solid fuels, indicate that the models describing the conversion of these at the very least take different parameters, if not completely different models altogether. Furthermore, the lower heating values of the biofuels, combined with their lower densities compared to coal necessitates a much larger volume of solid fuel particles per unit time to be injected into the furnace, which will influence the gas flow in the near-burner zone. Apart from the exchange of momentum between the phases, which is also present when firing coal, a much greater degree of displacement occurs, resulting in a changed flow pattern.

.

Chapter 2

Particle motion

Determination of solid particle motion in fluid flow is a well-established field of investigation, experimentally as well as numerically and analytically, and has been so for the duration of this century and before. Although a wide range of issues have been adressed, almost everything has been based on spherical particles, due to the absence of particle orientability. With this obstacle removed, several well-documented, coefficient-based formulations of forces acting upon spherical particles have been published[1].

Concurrently, a smaller amount of work has been done on non-spherical particles, shaped as ellipsoids. Although similar in scope, the formulations of the equations of motion of the ellipsoidal particles are very different from those normally used for spherical particles, not only in terms of the final form of these equations but also in terms of the inherent assumptions and analytical or experimental foundation. This is one of the main causes of the low level of transfer of knowledge between these two areas, something which has been particularly detrimental to the development of models of motion of non-spherical particles.

The onset of non-spherical particle modelling can be ascribed to the paper by Jeffery (1922), in which he derived the equations of motion for an ellipsoid under Stokes conditions. This paper forms the basis even for current work as that by Gallily and Cohen (1979), Maxey (1990) and Fan and Ahmadi (1995), where the equations of motion as derived by Jeffery have been used to predict the motion of non-spherical particles. A main contribution to the work of Jeffery has been the work of Brenner (1964a)[2], removing some of the shape-limiting assumptions, and allowing more general non-spherical particles, in the sense that the particle shape has to be a slight "perturbation", or deformation, of the sphere or ellipsoid, to be modelled.

[1] It is an exhaustive task to review the work within the field of gas-particle modelling due to the sheer amount of publications, and for this reason it is not undertaken here. For an up-to-date discussion of gas-particle systems, analytically, numerically and experimentally, please refer to Crowe et al. (1998).

[2] This is the first of a series of publications on the motion of non-spherical particles (Brenner 1964b), (Brenner 1964c) and (Brenner 1964d)

Besnard and Harlow (1986) were the first to attempt to bridge the gaps between the two particle tracking techniques, by setting up a model for 2D motion of an ellipsoid in stochastic turbulence, using a coefficient formulation of the equations of motion with the forced based on particle orientation as well as the flow characteristica.

In the following, the geometric and aerodynamical basis for a non-spherical particle model will be developed, based on the approach outlined by Besnard and Harlow (1986) and founded on theoretical considerations as well as experimental data from different types of particles.

In setting up a general coefficient-based Lagrangian model for the motion of arbitrary particles, there are a number of conditions which must be clearly defined. First of all, a description of the particle shape has to be expressed mathematically. After that, the methods of describing particle motion must be set up and evaluated.

2.1 Generalized equations of motion

The motion of a solid particle generally consists of translation as well as rotation, allowing the particle six degrees of freedom in a three-dimensional space. The motion is governed by the following set of equations:

$$\frac{d(m_p\vec{v}_p)}{dt} = \sum_i \vec{F}_i \tag{2.1}$$

$$\frac{d(I_{x'}\omega_{x'})}{dt} = \sum_i T_{x',i} + \omega_{y'}\omega_{z'}(I_{y'} - I_{z'}) \tag{2.2}$$

$$\frac{d(I_{y'}\omega_{y'})}{dt} = \sum_i T_{y',i} + \omega_{z'}\omega_{x'}(I_{z'} - I_{x'}) \tag{2.3}$$

$$\frac{d(I_{z'}\omega_{z'})}{dt} = \sum_i T_{z',i} + \omega_{x'}\omega_{y'}(I_{x'} - I_{y'}) \tag{2.4}$$

m_p: particle mass $[kg]$

$\vec{v}_p$: particle centre-of-mass velocity $[m/s]$

$\sum_i \vec{F}_i$: summation of forces acting on the particle $[N]$

$I_{m'}$: mass moment of inertia around main axis m' $[kgm^2]$. $m' = [x', y', z']$ (see figure 2.1)

$\omega_{m'}$: particle angular velocity $[rad/s]$

$\sum_i T_{m',i}$: summation of torques $[Nm]$ acting on the particle around main axis m'

In the case of a sphere, only translation is normally included, as the effect of rotation on a sphere generally does little to alter its trajectory. However, rotational effects are important when considering orientable particles, such as ellipsoids or cylinders. In this case, equation 2.2-2.4 must be included in the calculation, as equation 2.1 depends directly on them.

As equations 2.1 and 2.2-2.4 are the same types of equation, a general scheme of integration can be set up (see Appendix C). These equations can be re-written as

$$f'(t) = c_1(f(t) - c_2) + c_3 \tag{2.5}$$

where the left hand side corresponds to the derivative term of the left hand side of the equation of motion in question, and the right hand side is a rewritten form of the terms on the right hand side, such that the active variable is isolated.

Assuming constant fluid velocity and slip velocity during a time step t, equation 2.5 can be intregrated once in time to yield the velocity ($\vec{v}_p$ or $\vec{\omega}_{i'}$):

$$f(t) = c_2 + (f(t_0) - c_2)\exp(c_1 t) - \frac{c_3}{c_1}(1 - \exp(c_1 t)) \tag{2.6}$$

and once more to yield the position ($\vec{x}_p$ or $\vec{\theta}_{i'}$):

$$F(t) = F(t_0) + c_2 t - \frac{1}{c_1}(f(t_0) - c_2)[1 - \exp(c_1 t)] - \frac{c_3}{c_1}\left[t - \frac{1}{c_1}(1 - \exp(c_1 t))\right] \tag{2.7}$$

$-c_1$ is identified as the reciprocal of the aerodynamic response time (to be defined later in this chapter), or, more generally, the resistance coefficient, c_2 contains the fluid velocity, and c_3 terms which can be considered conservative with regard to the active variable, such that they are independent of orientation and velocity.

2.2 Orientability and coordinate systems

Almost all the above forces and torques depend in some way on the orientation of the particle. The drag forces depend on the projected area of the particle normal to the flow, the lift forces on the projected area of the particle in the same plane as the flow, and so on. Thus, a method of expressing particle orientation in terms of the inertial system must be devised. Such a method will almost invariably base itself on the use of direction cosines, which express the orientation of a line given by two points, P_1 and P_2, and length, d, as:

$$\theta_i = \arccos\left(\frac{x_{i,2} - x_{i,1}}{d}\right) \tag{2.8}$$

The incidence angle is defined as the angle between the particle major axis and the flow velocity vector. Using direction cosines, this can be written as the "dot" product of the direction cosines of the two vectors:

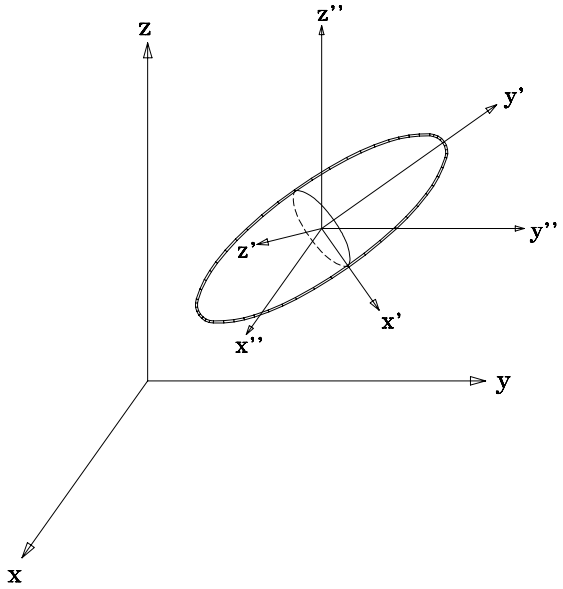

Figure 2.1: The relationship between the inertial $[x, y, z]$, the co- rotational $[x', y'z']$ and the co-moving $[x'', y'', z'']$ coordinate systems.

$$\alpha_{i,n} = \arccos \sum_{i=1}^{3} (\cos\theta_{iy'} \cos\theta_{i\vec{u}}) \tag{2.9}$$

n: x, y or z

$\theta_{iy'}$: direction cosines of the major particle axis y'

$\theta_{i\vec{u}}$: direction cosines of the velocity vector $\vec{u}$

For the current formulation, where the incidence angle is determined between each of the three velocity components and the particle major axis, equation 2.9 reduces to:

$$\alpha_i = \theta_{iy'}, \qquad i = 1, 2, 3 \tag{2.10}$$

The area needed for the lift calculation is in the plane of the velocity vector. Again, splitting the velocity into its components, the three projections becomes those which are orthogonal to the projected area, and determining the size of each merely becomes a matter of substituting the angle of incidence with $\frac{\pi}{2} + \alpha_i$.

2.2.1 Particle axes orientation

In order to describe the rotation of the particle, it is necessary to know the orientation of the particle at any given time. The moments of inertia used in equations 2.2 - 2.4

are the moments of inertia in the particle coordinate system, so in order to describe particle rotation in the inertial system, the relationship between these two systems must be know at all times. This means that the direction cosines given in equation 2.8 have to be re- calculated after each time step, using the angular velocities of the particle.

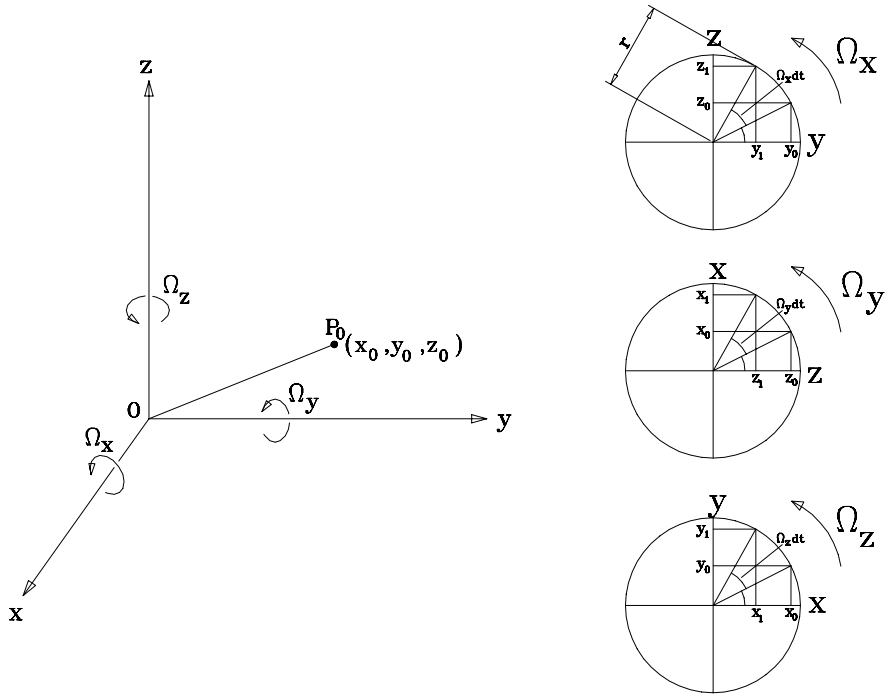

Figure 2.2: Rotation of an arbitrary line with coordinates $O(0,0,0)$ and $P_0(x_0, y_0, z_0)$ in the inertial system $[x, y, z]$.

Considering figure 2.2, an arbitrary line OP_0 of length $d = 1$ is rotated in the inertial system by the rotation vector $[\Omega_x, \Omega_y, \Omega_z]$. This gives rise to the following changes in coordinates of P_0, as indicated on the right hand side of figure 2.2:

$$\begin{aligned}
\Delta x &= \cos\theta_{01}\left[\cos(\Omega_y dt) + \cos(\Omega_z dt) - 2\right] - \cos\theta_{02}\sin(\Omega_z dt) + \cos\theta_{03}\sin(\Omega_y dt) \\
\Delta y &= \cos\theta_{01}\sin(\Omega_z dt) + \cos\theta_{02}\left[\cos(\Omega_x dt) + \cos(\Omega_z dt) - 2\right] - \cos\theta_{03}\sin(\Omega_x dt) \\
\Delta z &= -\cos\theta_{01}\sin(\Omega_y dt) + \cos\theta_{02}\sin(\Omega_x dt) + \cos\theta_{03}\left[\cos(\Omega_x dt) + \cos(\Omega_y dt) - 2\right]
\end{aligned} \tag{2.11}$$

$\theta_{01}, \theta_{02}, \theta_{03}$: original direction cosines of the line OP_0

Transforming Δx, Δy and Δz to changes in direction cosines, and referring to eq. 2.8, the new direction cosines of the line after the rotation $[\Omega_x, \Omega_y, \Omega_z]$ are:

$$\begin{aligned}
\theta_{11} &= \cos^{-1}(\cos\theta_{01} + \Delta x) \\
\theta_{12} &= \cos^{-1}(\cos\theta_{02} + \Delta y) \\
\theta_{13} &= \cos^{-1}(\cos\theta_{03} + \Delta z)
\end{aligned} \tag{2.12}$$

Thus, in order to rotate the particle coordinate system, the above equations must be applied to each of the particle axes.

2.3 A general class of particles

Apart from a few specialized academic codes, particle tracking codes have been designed exclusively to handle spherical particles. The academic codes, in their turn, have been designed almost explicitly to ellipsoids. Thus, none of these categories of codes are able to handle arbitrarily shaped particles. One common way to remedy this shortcoming, is to introduce a "sphericity factor", which conveys information of the degree of deviation of the particle from the spherical shape. In various ways, this factor is then included in the equation of motion. Obviously, although a simple correction (and thus attractive), this is a "quick and dirty" solution without much physical basis, with a large amount of information loss. Furthermore, it becomes almost impossible to compare particles which can have entirely different shapes and therefore different aerodynamic behaviours, although they have the same sphericity.

When defining a more general class of particles, it is desirable to draw upon the knowledge concerning these two shapes, without losing the ability to describe a wide range of shapes with essentially the same set of equations. Therefore, the surface formulation must be based on mathematical similarity, and this immediately rules out cylinders and irregular shapes.

Keeping in mind that a sphere is a special case of an ellipsoid, a further generalization of the ellipsoid-concept is chosen as the overall shape function of the general particle class. Such a shape function was proposed in the 1960s by the Danish mathematician Piet Hein, who named his shape class the superellipsoid[3]. The superellipsoid is characterized by having an exponent not necessarily equal to 2:

$$\left(\frac{x}{a}\right)^n + \left(\frac{y}{b}\right)^n + \left(\frac{z}{c}\right)^n = 1, \qquad n \geq 2 \tag{2.13}$$

As can bee seen, both the sphere and the ellipsoid as well as a very close approximation to the cylinder for sufficiently high exponents are included in this formulation. By varying the exponent as well as the minor and major axes, a wide range of shapes can be prescribed, all basing themselves on the same mathematical formulation. Examples of this are shown in figure 2.3.

Although it would be possible to use equation 2.13 as it is written, essentially allowing the particle to be superelliptic in all three directions, the current model does place one important constraint on the shape, namely that it is a regular body of revolution about

[3](Hein 1964) The superellipsoid has been used extensively in Danish furniture design, as well as for one of the main squares in Stockholm, Sveaplatsen.

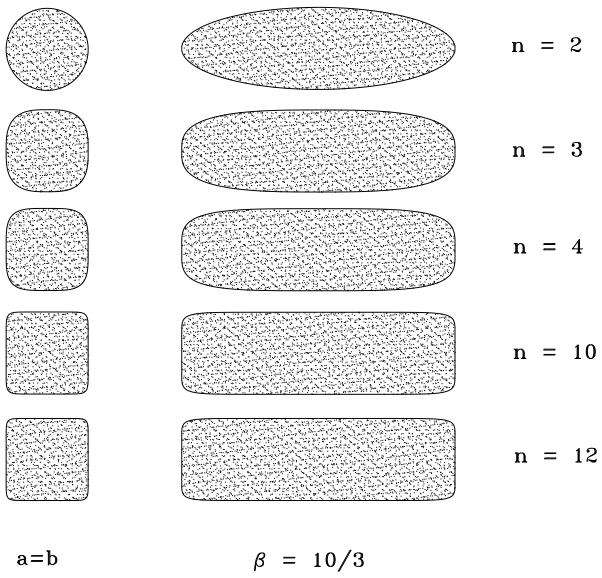

Figure 2.3: The effect of changing the superelliptic exponent for $\beta = 1$ and $\beta = 10/3$.

the major axis, such that $a = c$ and equation 2.13 becomes:

$$\left(\frac{x}{a}\right)^n + \left(\frac{y}{b}\right)^n = 1 \tag{2.14}$$

In the following, the shapes generated by equation 2.14 will be referred to as spheres for $n = 2$ and $\beta => 1$, ellipsoids for $n = 2$ and $\beta > 1$, cylinders for $n \to \infty$ and $\beta \geq 1$, and general superellipsoids for $\infty > n \geq 2$ and $\beta \geq 1$.

Having dealt now with the shape of the general particle, based on mathematical similarity, it is necessary to turn to a general description of particle-fluid interaction, based on the more complicated concept of aerodynamical similarity.

2.3.1 Areas

The projected area of a superellipsoid revolving around one of it's minor axes can be based on the expression proposed by Besnard and Harlow (1986):

$$A_p = \pi a^2 (\cos^2 \alpha_i + \beta^2 \sin^2 \alpha_i)^{1/2} \tag{2.15}$$

α_i: angle of incidence with regard to the velocity vector $[rad]$

a, b: minor and major semi-axis dimensions $[m]$

β: axes aspect ratio $\frac{b}{a}$ $[-]$

In equation 2.15, it is utilized that the ratios of the projected areas at zero and ninety degrees incidence, respectively, corresponds to the square of the axis aspect ratio.

Employing the same methodology, the current formulation becomes a matter of replacing β by R_β:

$$A_p = \pi a^2(\cos^2\alpha_i + R_\beta^2 \sin^2\alpha_i)^{1/2} \tag{2.16}$$

R_β: ratio of projected areas at $\alpha_i = 90$ and $\alpha_i = 0$ degrees $[-]$

Projecting the area of a superellipsoid onto a velocity vector thus becomes a question of determining the angle between the major axis of the particle and the velocity vector

2.3.2 Constraints and assumptions of the model

The model is constrained by the following:

- The equations of motion for a sphere must be resolved for $\beta \to 1$, where β is the ratio of the major to the minor semiaxis, and for $n \to 2$.
- For angles of incidence of $0, \frac{\pi}{2}, \pi$ and $\frac{3\pi}{2}$ $[rad]$, the lift must vanish due to symmetry.
- The lift must be invariant under an angle of incidence rotation of π $[rad]$
- The pitching moment must vanish for angles of incidence of $0, \frac{\pi}{2}, \pi$ and $\frac{3\pi}{2}$ $[rad]$.
- The particle is assumed to be rigid, solid and homogeneous.

2.4 Aerodynamic properties of superelliptic particles

Defining the forces which act on discrete particles in a flow field has been a great challenge to researchers, and quite a number of more or less exotic forces have been defined. Although the method of obtaining these forces is similar in most investigations, in that two velocity distributions are considered, one at the centre of the particle, and one at infinity, which are matched assymptotically at the particle surface, there is some confusion as to whether some forces are really distinct or just different ways of expressing the same thing and therefore simply adding them can be erroneous (Astrup 1992). Not nearly the same amount of work has been done regarding the torques on discrete particles, as a very common assumption has been to assume that the particle does not rotate.

In the present work, attention will be centered on just those forces which are known to influence the motion of the particle. The determination of these forces for non-spherical

particles will be based on the spherical expressions, where the characteristic dimensions will be rewritten, and subject to the above constraints.

Almost all forces relate to the relative velocity between the particle and surrounding fluid, one of the notable exceptions is the "Faxen force". The Faxen force is a viscous force, which derives from the curvature of the velocity field. It is defined as:

$$\vec{F}_{Faxen} = \frac{3}{4} V_p \mu_g \nabla^2 \vec{u}_g \tag{2.17}$$

V_p: particle volume $[m^3]$
μ_g: gas molecular viscosity $[kgm/s]$
$\vec{u}_g$: gas velocity vector $[m/s]$

According to (Maxey and Riley 1983) and as will become apparent in the following, several of the particle forces contain this force as a so-called "Faxen term", which is $k\nabla^2\vec{u}_g$, where k is a constant, depending on the force.

The forces which will be discussed in the following are:

- A total drag force, consisting of viscous and form drag.
- A lift force due to the orientability of the particle.
- A lift force due to fluid velocity gradients (Saffmann force).
- A transverse lift force due to particle rotation (Magnus force).
- A body force due to the displacement of fluid (buoyancy).
- A pressure gradient force.
- A viscous torque due to the vorticity of the flow field.
- A form torque due to velocity gradients on the particle surface.

For most engineering systems, where the density of the dispersed phase is much larger than that of the continuous phase, the drag and gravity forces are generally thought to be dominant (see for instance Rusaas (1998), who has shown that for combusting coal particles, the drag force accounts for more than 90% of the forces acting upon the particle during its lifetime), but for non-isotropic particles[4] lift forces must also be considered.

[4]Particles which have one or more dominant dimension.

2.4.1 Aerodynamic response times

The aerodynamic response time of a particle τ_p, expresses the "dead time" of the particle, i.e. the time it takes for a particle to react to a change in the surrounding fluid velocity, and reach a velocity corresponding to 63% (or $1-e^{-1}$) of the fluid velocity.

For translation of arbitrary particles[5] this can be expressed as:

$$\tau_{p,t} = \frac{2m_p}{\rho_g C_D A_p |\vec{u}_g - \vec{u}_p|} \tag{2.18}$$

ρ_g: gas density $[kg/m^3]$
C_D: drag coefficient $[-]$
$\vec{u}_g$: gas velocity vector $[m/s]$
$\vec{v}_p$: particle velocity vector $[m/s]$

For rotation, the fluid vorticity replaces the velocity, and the response time becomes:

$$\tau_{p,r} = \frac{I}{K_\omega \mu_g V_p} \tag{2.19}$$

I: mass moment of intertia $[kgm^2]$
μ_g: gas molecular viscosity $[kg/ms]$

For arbitrary particles, which have different moments of inertia around the co-rotational coordinate system (see figure 2.1), the rotational response time is referred to the main axis of rotation.

The aerodynamic response time is quite fundamental to the description of single particle aerodynamics, as it combines inertial and dimensional parameters to produce a single, unambiguous quantity on which to base system comparisons and results upon. The uniqueness of the aerodynamic response time is shown in figure 2.4, where the aerodynamic response time of different types of superellipsoids in a swirling flow within an isothermal combustion chamber (see Chapter 6) is shown. The large peaks for the particles with large aspect ratios clearly indicate the different aerodynamic properties, as the particles not only rotate with the swirling flow, but also about themselves. Finally, the aerodynamic response time represents a means of characterizing gas- particle systems in terms of coupling between the two phases. By defining the ratio known as the Stokes number Sk the coupling of the phases in the system can - on an average scale - be classified according to table 2.1:

$$Sk = \frac{\tau_p}{\tau_s} \tag{2.20}$$

τ_s: Characteristic system time scale

[5] The aerodynamic response time for spheres is often shown in it's most reduced form, $\tau_p = \frac{4\rho_p d_p^2}{3\mu_g C_D Re_p}$

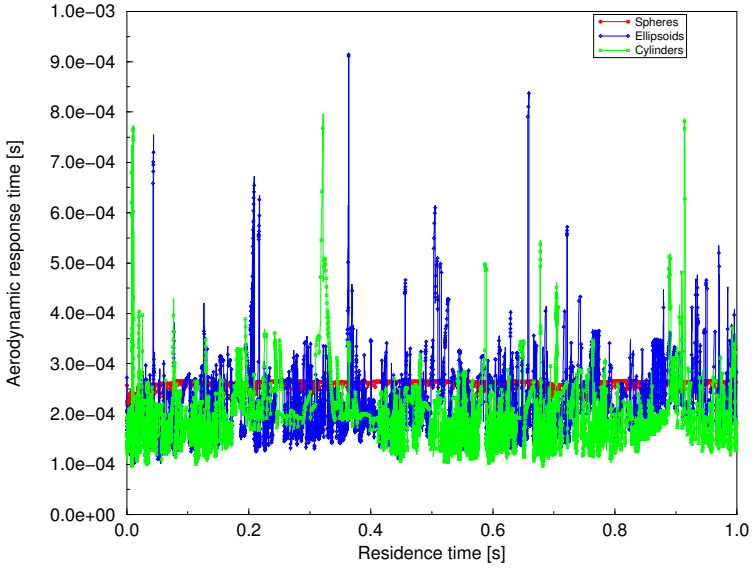

Figure 2.4: The aerodynamic response time ($\tau_{p,t}$) of different particle shapes in swirling isothermal flow in a tubular combustion chamber (see Chapter 6). Sphere: $n = 2.0,\ \beta = 1.0$; ellipsoid: $n = 2.0,\ \beta = 10.0$; and cylinder: $n = 50.0,\ \beta = 10.0$.

$$\tau_s = \frac{L_{char}}{\bar{u}_{char}} \tag{2.21}$$

L_{char}: Characteristic length $[m/s]$

u_{char}: associated characteristic velocity $[m/s]$

For reacting gas-particle systems, the coupling mechanisms become more complex, as not only inertial coupling, but also thermal and chemical coupling must be considered. Thus, although most reacting systems have a loading ratio (the mass flow ratio of the dispersed phase to the continuous phase) of approximately 0.1 and below, they must be considered two-way coupled regardles of the value of the Stokes number.

$Sk \leq 10^{-2}$	Single phase mixture
$10^{-2} \leq Sk \leq 10^{2},\ \frac{m_p}{m_f} \leq 0.1$	Gas-to-particle one-way coupling
$10^{-2} \leq Sk \leq 10^{2},\ \frac{m_p}{m_f} \geq 0.1$	Two-way coupling
$Sk \geq 10^{2}$	Particle-to-gas one-way coupling

m_f: gas mass flow times unit time $[kg]$
m_p: particle mass flow times unit time $[kg]$

Table 2.1: System charactization using Stokes number and mass loading ratios (Dall 1988).

2.4.2 Drag forces

The drag force consists of two contributions, a viscous (friction) and a form (pressure) drag, and is commonly expressed over the entire Reynolds number spectre as:

$$\vec{F}_D = \frac{1}{2} C_D \rho_g A_p |\vec{u}_g - \vec{v}_p| (\vec{u}_g - \vec{v}_p) \tag{2.22}$$

C_D: drag coefficient
ρ_g: fluid density $[kg/m^3]$
A_p: projected particle area $[m^2]$

The drag coefficient $C_{D,sphere}$ of a sphere is normally expressed as some form of Reynolds number based modification of the Stokes drag coefficient $C_{D,Stokes}$:

$$C_{D,sphere} = C_{D,Stokes} f = \frac{24}{Re_p} f \tag{2.23}$$

Re_p: particle Reynolds number $[-]$:

$$Re_p = \frac{|\vec{u}_g - \vec{v}_p| d_p}{\nu_g} \tag{2.24}$$

d_p: particle diameter $[m]$
ν_g: fluid viscosity $[m^2/s]$

For low Reynolds numbers, the correction factor reduces to unity, and the linear relationship between drag force and slip velocity of Stokes flow is resolved. In the current work, the modification factor f is due to A. Kaskas (Brauer 1971):

$$f = 1 + \frac{\sqrt{Re_p}}{6} + \frac{Re_p}{60} \tag{2.25}$$

This form has been chosen rather than the more common form of $f = 1 + 0.15 Re_p^{0.687}$ due to its superiority in the Reynolds number range greater than 10^3 (see Smoot and Pratt (1979) or Rusaas (1995)).

The formulation of a general drag coefficient in the current work will thus be based on additional modification factors applied to $C_{D,Stokes}$, such that the resulting drag coefficient will be applicable to all shapes within the scope of the model, ranging from spheres to cylinders, as well as to a wide range of Reynolds numbers and incidence angles from zero to 90 degrees. For the general particle, the Reynolds number is given as:

$$Re_p = \frac{2|\vec{u}_g - \vec{v}_p| a}{\nu_g} \tag{2.26}$$

a: minor semi-axis of particle $[m]$

Further, the shape limiting cases must be resolved, such that the drag coefficient of a superellipsoid with $n = 2$ and $\beta = 1$ is that of a sphere, and the drag coefficient of a superellipsoid with $n = \infty$ and $\beta = \infty$ equals that of an infinitely long cylinder[6].

Studies of the drag coefficients of various spheres, cylinders and ellipsoids at right angles of incidence as functions of the Reynolds number show a large degree of similarity (see figure 2.5), and indicate that a general shape dependent correlation can be formulated, essentially making an assumption of what might be termed aerodynamical similarity. Using the bounding cases, as stated above, of the sphere and cylinder, and assuming a linear dependency on both n and β, the following shape correlations are defined:

$$C_D = C_{D,Stokes} f f_{sel} \tag{2.27}$$

with the shape correlation f_{sel} defined as:

$$f_{sel} = \left[\frac{Re_p}{(\beta - 1) + f_{1\beta} Re_p} \right]^{f_{2\beta}} f_n \tag{2.28}$$

$$\begin{aligned} f_n &= 0.857 + 1.46 \times 10^{-3}(n - 2.0) \\ f_{1\beta} &= 0.067 + 2.65 \times 10^{-3}(100.0 - \beta) \\ f_{2\beta} &= 0.142 + 5.68 \times 10^{-4}(\beta - 5.0) \end{aligned} \tag{2.29}$$

These correlations now make it possible to trace the Reynolds number dependency of the drag coefficient for all superellipsoids, as plotted in figure 2.5.

For all the shapes shown in figure 2.5, three distinct boundary layer transition points, separating different boundary layer regimes, can be determined. In the range $Re_p \leq 0.1$, the so-called Stokes regime, where a linear relationship between resistance and Reynolds number exists and viscous drag dominates, the boundary layer is laminar, and the streamlines of the surrounding fluid are aligned with the particle surface, such that these are equivalent in front of and behind the particle. As the Reynolds number moves into the range $[0.1; 1.0]$, the boundary layer at the back of the particle begins to separate, and at Reynolds numbers between 1.0 and approximately $10^4 - 2 \times 10^4$, a wake builds up behind the particle, with the separation point moving forward along the particle surface with increasing Reynolds number. In this range (above $Re_p \approx 250$), the relationship between form and pressure drag changes, such that the pressure drag becomes dominant. At Reynolds numbers greater than approximately 2×10^4, the drag coefficient assumes a near-constant value, and the build-up of the wake behind the particle is complete[7].

The final distinct transition point occurs at the critical Reynolds number, which is approximately 3×10^5. At this Reynolds number, the laminar boundary layer on the forward part of the particle becomes turbulent, with the resulting abrupt decrease of the drag coefficient caused by the higher resistance of the turbulent boundary layer to separation.

[6] In the current formulation, ∞ is defined as 100.0.

[7] This does not mean that the wake is stationary. At Reynolds numbers greater than 500, the wake

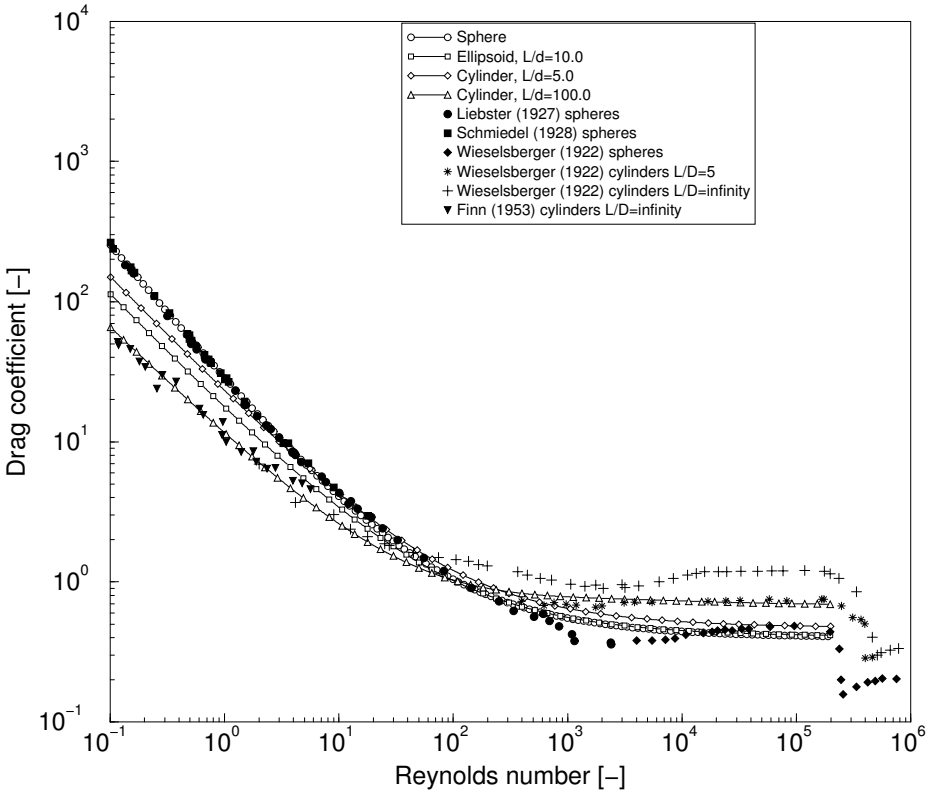

Figure 2.5: The calculated (eq. 2.27-2.28) and measured drag coefficient (C_D) of various regular shapes at right angles of incidence as a function of particle Reynolds number (Re_p).

Equation 2.27 as well as the wakes shown in figure 2.6 at different Reynolds numbers are all shown at right angles of incidence. In order to account for incidence angles different from ninety degrees, the above set of equations must be extended, by introducing correction factors based on geometric and physical considerations.

An investigation of the aerodynamic properties of different superellipsoids (see Appendix G or (Rosendahl 1997)) using Laser Sheet Visualisation (LSV) techniques has shown that there is quite a large difference in the flow patterns around the particles, as shown in figure 2.7. Notably for large superelliptic exponents and aspect ratios, i.e. going toward cylinders, there are two distinct wake zones behind the particle. These are caused by two geometric features, the sharp "corners" due to the high superelliptic exponent, and the relatively large aspect ratio. The former causes the flow to detach from the upper and lower rear sides of the particle with elements of vortex shedding, and the latter, at incidence angles different from zero or ninety degrees, projects an elliptical obstacle for the flow around the central part of the particle, which allows the flow to remain attached on the entire surface section.

---

behind a sphere assumes an unsteady character, with vortex shedding. This is also evident in figure 2.7, particularly for the cylinder.

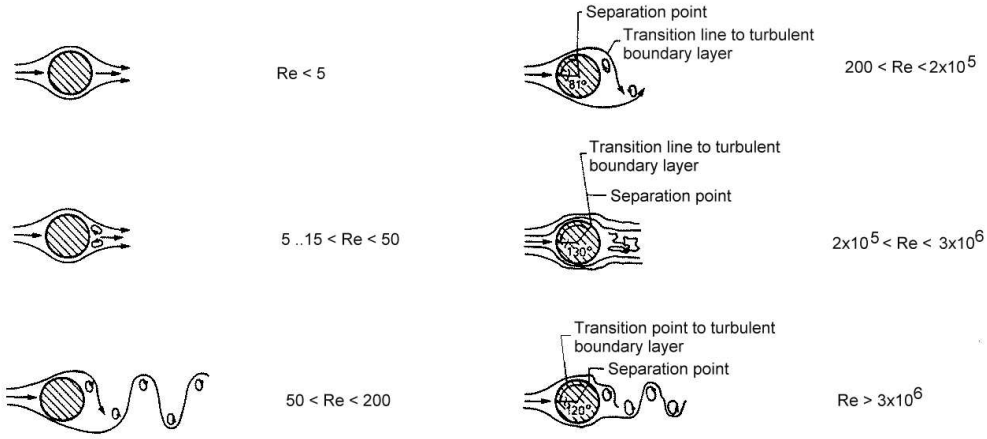

Figure 2.6: Development and structure of the boundary layer on a cylinder as the Reynolds number increases. The flow is perpendicular to the main axis of the cylinder. From Nielsen (1986)

In order to investigate the effect of different flow patterns on the lift and drag properties, CFD calculations of the flow situations have been made. The results of these, shown in figure 2.8, indicate that these differences make themselves very clear in the aerodynamic properties. As shown, the sharp edges of the cylinder causes the drag coefficient to behave differently, particularly at low angles of incidence.

The incorporation of the aerodynamic dissimilarities into a single model is based upon the following formulation.

- The drag coefficient changes within the limits of a base and a top drag coefficient, defined by the limiting shapes of the superellipsoid formulation. The base drag coefficient, forming the lower limit, is defined to be the drag coefficient at zero degrees incidence. The top drag coefficient, forming the upper limit, is defined to be the drag coefficient at 90 degrees incidence. As mentioned previously, the top drag coefficient will often be determined experimentally. If this is not the case, equation 2.27 is used[8].

- Where no experimental data is available, the base drag coefficient is given by the expression

$$C_{D,base} = C_{D,top} \frac{A_s}{A_{p,\alpha=0^\circ}} \frac{R_\beta}{\beta \exp\left(\frac{-n}{n_{max}}\right)} \tag{2.30}$$

  This is based on a consideration of the influential parameters, which are the surface and projected areas, to give the two types of drag, viscous and pressure

[8]In order to provide experimental data for the base drag coefficient, and further improve equation 2.27 as well as experimentally validating the cross-flow principle, LDA/strain gauge measurements of the aerodynamic properties of different superellipsoids are planned for late summer 1998.

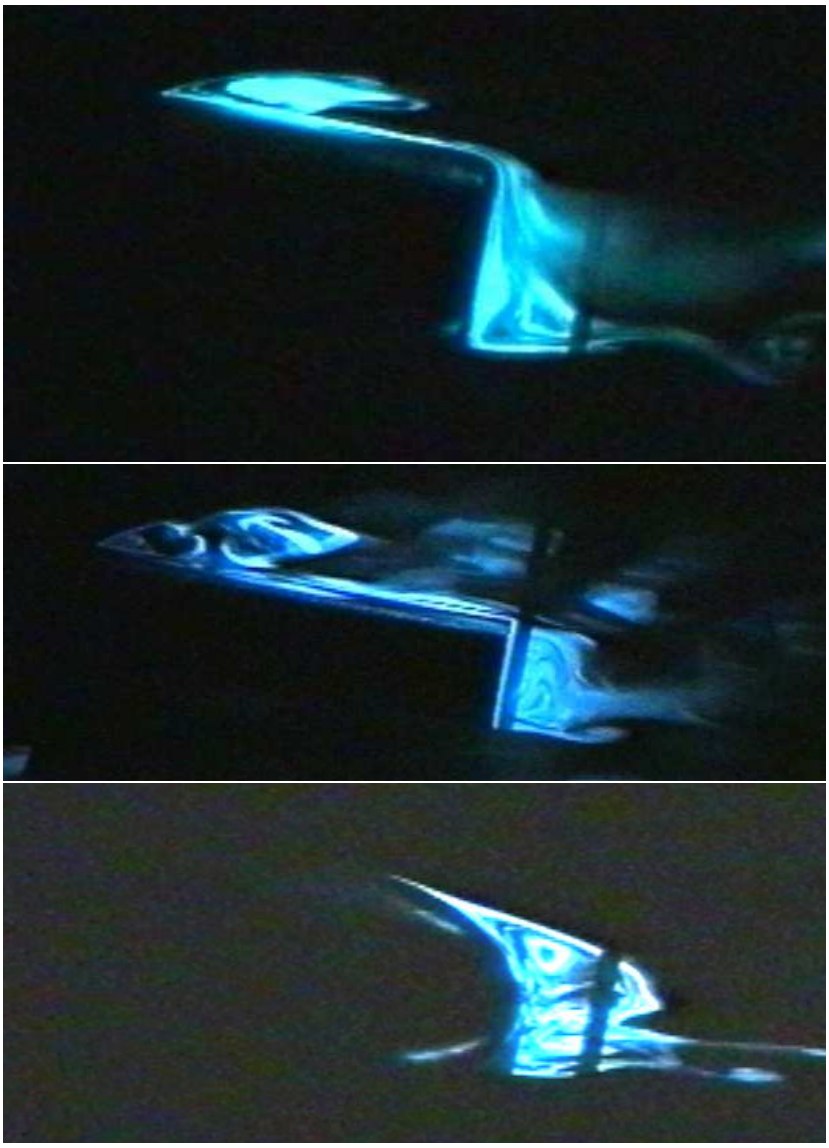

Figure 2.7: Laser Sheet pictures of the wakes of superellipsoids at 10° incidence and $Re_p = 1000$, showing the different flow characteristics of the shapes. From top: general superellipsoid, $\beta = 1.86,\ n = 25.0$; cylinder, $\beta = 3.86,\ n = 100.0$; and ellipsoid, $\beta = 2.0,\ n = 2.0$. Flow direction is from left to right.

drag, as well as the superelliptic exponent and aspect ratio.

- The relationship between drag coefficient and incidence angle is given by the expression

$$C_D(\alpha_i) = C_{D,base} + (C_{D,top} - C_{D,base}) \sin^3 \alpha_i \tag{2.31}$$

Equation 2.31 is shown in figure 2.9, and although the C_D-peak of the cylinder at 0° incidence is not captured, the main features of the three shapes are well reproduced.

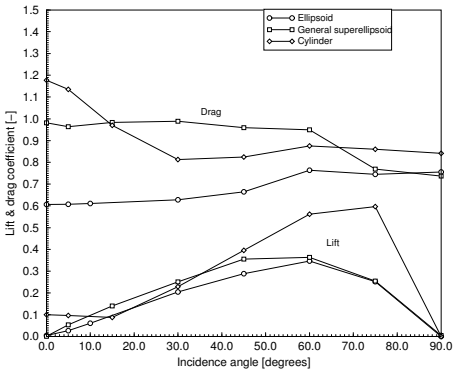

Figure 2.8: Drag ($C_D(\alpha_i)$) and lift ($C_L(\alpha_i)$) coefficients at $Re_p = 1000$ as determined by the CFD calculations. A general feature is an overprediction of the drag coefficient.

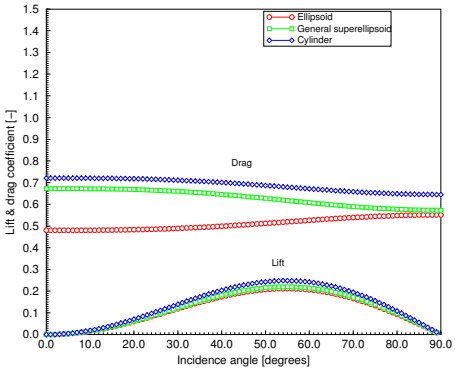

Figure 2.9: Drag ($C_D(\alpha_i)$) and lift ($C_L(\alpha_i)$) coefficients at $Re_p = 1000$ using equation 2.31.

2.4.3 Lift forces

The lift forces which act on a particle in a velocity field arise due to a number of factors. The most common type of lift is the profile lift, which stems from the orientability of the particle. This is the lift which is commonly used in connection with aerodynamic profiles, and, for large particles, it is the dominant lift force. For smaller particles, other lift forces must also be considered, such as the Saffmann and Magnus lift forces.

Profile lift

For Reynolds numbers less than 10^3, the profile lift can be estimated from the drag coefficient using the cross-flow principle of Hörner (1965). From figure 2.10, it can be seen that a normal force can be calculated from the drag coefficient and incident velocity perpendicular to the major axis of the particle. Thus, the profile lift coefficient can be expressed as:

$$C_{L,profile} = C_D f_\beta \sin^2 \alpha_i \cos \alpha_i \tag{2.32}$$

f_β : $f_\beta = 0$ for $\beta = 1$ and $f_\beta = 1$ for $\beta > 1$

The profile lift force is then:

$$\vec{F}_{L,profile} = \frac{1}{2} C_{L,profile} \rho_g A_{\alpha_i} |\vec{u}_g - \vec{v}_p| (\vec{u}_g - \vec{v}_p) \tag{2.33}$$

A_{α_i}: projected particle area perpendicular to the direction of the force $[m^2]$

Due to an absence of data at high Reynolds numbers, the current work will assume that the cross-flow principle is valid for all Reynolds numbers. For the Reynolds numbers

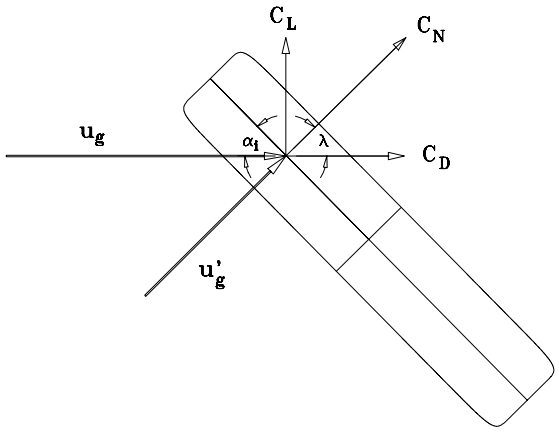

Figure 2.10: The determination of lift from a normal force based on incident velocity and drag coefficient. The forces are shown to attack in a point along the major axis corresponding to 0.25×chord length in aerofoil theory.

500, 1000 and 1500, the validity of the cross-flow principle is qualitatively corroborated (see figure 2.11).

Saffmann lift force

The Saffmann lift force, or the "slip-shear" force, arises due to velocity gradients in the flow, typically near solid boundaries, but also in areas characterized by shear layers, as for example recirculation zones. The direction of the force is perpendicular to the velocity gradient in the direction of higher fluid velocities. For a slow shear flow, the force is given by Saffmann (1965) as:

$$F_{L,Saffmann} = 6.46\mu_g|\vec{u}_g - \vec{v}_p|\frac{d_p^2}{4}\sqrt{\frac{|\kappa|}{\nu_g}} \tag{2.34}$$

κ: undisturbed fluid velocity gradient $[s^{-1}]$

As a more general formulation, Astrup (1992) proposes:

$$\vec{F}_{L,Saffmann} = 6.46\rho_g\frac{d_p^2}{4}\sqrt{\frac{\nu_g}{|\nabla\times\vec{u}_g}}\,(\vec{u}_g - \vec{v}_p)\times(\nabla\times\vec{u}_g) \tag{2.35}$$

The geometric dependence of the Saffmann force on a spherical particle is the projected area, and it is assumed that the same is true for nonspherical particles, and for general non-spherical particles, the Saffmann lift force thus becomes:

$$\vec{F}_{L,Saffmann} = \frac{6.46}{\pi}\rho_g A_{\alpha_i}\sqrt{\frac{\nu_g}{|\nabla\times\vec{u}_g|}}(\vec{u}_g - \vec{v}_p)\times(\nabla\times\vec{u}_g) \tag{2.36}$$

A_{α_i}: projected particle area perpendicular to the direction of the force $[m^2]$

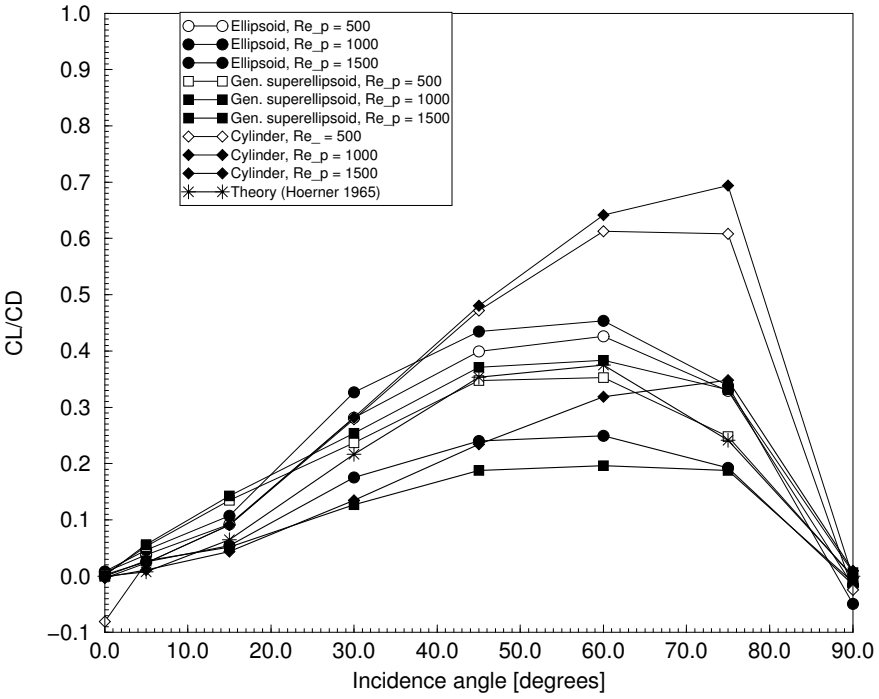

Figure 2.11: The ratio of lift and drag coefficients (glide numbers) as a function of incidence angle (α_i) for different superelliptic particles. Ellipsoid: $\beta = 2.0,\ n = 2.0$; general superellipsoid: $\beta = 1.86,\ n = 25.0$; and cylinder: $\beta = 3.83,\ n = 100.0$.

Magnus lift force

The Magnus lift force is caused by particle rotation. Due to entrainment of the fluid as the particle rotates, a velocity difference arises between the sides of the particle, and the particle will tend toward the side with the higher velocity. For a sphere, the Magnus force is given by

$$\vec{F}_{L,Magnus} = \rho_g \frac{\pi}{8} d_p^3 (\vec{u}_g - \vec{v}_p) \times \vec{\omega}_p (1 + O(Re_p)) \tag{2.37}$$

For a non-isotropic particle, rotation about the major axis (y' in figure 2.1) results in the same type of Magnus force as for the sphere, but rotation about the minor axes (x' or z' in figure 2.1) gives an additional contribution to the Magnus force. Rotation about the minor axes causes a low pressure zone to develop behind the particle, and a high pressure zone in front, as shown in figure 2.12. Thus, for non-spherical particles, the Magnus force can, in part, assume characteristics of the pressure gradient force, which is a body force, and profile lift as discussed previously.

As it is unclear to what extent the Magnus force is included in other forces for non-isotropic particles, the Magnus force can tentatively be re-formulated in the same man-

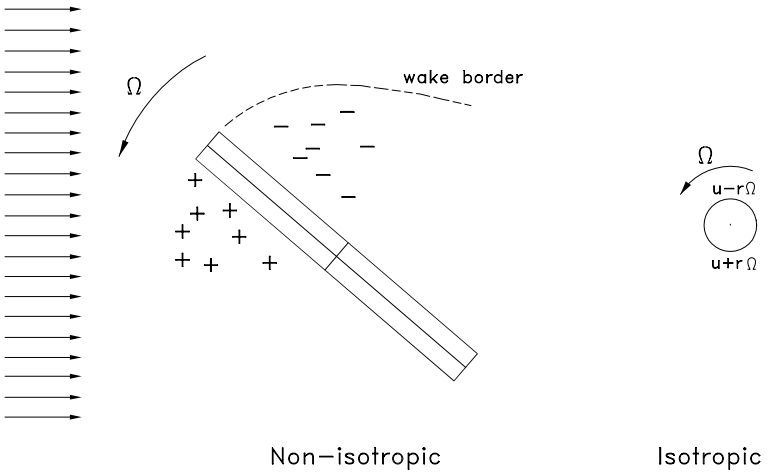

Figure 2.12: A non-isotropic particle rotating about the minor (left side) and major (right side) axis. In the former situation, the particle causes a low pressure zone behind it and a high pressure zone in front of it. In the latter, "spherical" Magnus force characteristics are retained.

ner as the Saffmann lift force. Being a lift force, the characteristic particle dimension is the projected area perpendicular to the force, and the remaining particle diameter (in the case of spheres) is related to the angular velocity at the surface of the particle. Thus, for non-spherical particles, the Magnus force for rotation about the minor axes may be re-written as:

$$\vec{F}_{L,Magnus} = \frac{1}{2} A_{\alpha_i} \rho_g \bar{d}_p (\vec{u}_g - \vec{v}_p) \times \vec{\Omega}_p (1 + O(Re_p)) \tag{2.38}$$

A_{α_i}: particle area perpendicular to the direction of the force $[m^2]$

$\bar{d}_p$: mean "spherical" diameter $[m]$, based on particle sphericity (see eq. 2.39).

$\vec{\Omega}_p$: particle rotation expressed in inertial system $[rad/s]$

$$\bar{d}_p = \sqrt{4ab} \tag{2.39}$$

2.4.4 Body forces

The body forces discussed here include buoyancy and pressure gradient forces. The buoyancy depends exclusively on the volume, and not the shape of the particle, so the standard expression is valid here:

$$\vec{F}_{buoyancy} = V_p \rho_p \left(1 - \frac{\rho_g}{\rho_p}\right) \vec{g} \tag{2.40}$$

The pressure gradient force stems from static pressure differences on opposing sides of a particle. Thus, the characteristic dimensions are projected area, and distance between

the opposing sides. With this, the pressure gradient force is expressed as:

$$\vec{F}_{\nabla P_g} = -A_p \bar{d}_p \nabla P \tag{2.41}$$

2.4.5 Torques

The torques acting on a particle stem from two main sources:

- The vorticity of the general flow field $\left(\frac{1}{2}\nabla \times \vec{u}_g\right)$
- Macroscopic velocity gradients on the particle surface $\left(\frac{\partial \vec{u}_g}{\partial \vec{x}}\right)$
- Aerodynamic torque on the cylinder (also known as pitching moment), arising from the pressure distribution on the cylinder

Vorticity

It can be shown that practically all general flows posses some measure of vorticity (see for instance Fredsøe (1991)). A particle suspended in a fluid possessing vorticity will experience this as a viscous torque, causing the particle to rotate around its axes. The torque can be expressed as:

$$\vec{T}_{viscous} = K_\omega \mu_g A_s \bar{d}_p \left(\frac{1}{2}\nabla \times \vec{u}_g - \vec{\Omega}_p\right) \tag{2.42}$$

K_ω: constant of the order of unity (Besnard and Harlow 1986)
A_s: surface area of particle $[m^2]$
$\vec{\Omega}_p$: particle rotation expressed in inertial system $[rad/s]$

Macroscopic velocity gradients

When considering particles of all size classes, it is necessary to allow for macroscopic velocity gradient effects. Referring to figure 2.13, the situation depicted will give rise to a moment around the minor axis of the particle. Assuming linear variation in velocity on the particle surface, and considering the two halves of the particle separately, a resulting force on each half can be written as:

$$F_{\nabla u} = p_{dyn} A = \frac{1}{4}\rho_g |\bar{u}_g - v_p|(\bar{u}_g - v_p) A_p \tag{2.43}$$

p_{dyn}: dynamic pressure $[Pa]$
A_p: projected area of particle $[m^2]$
$\bar{u}_g$: mean fluid velocity on the half section:

$$\bar{u}_g = 0.5(u_2 + u_1) \tag{2.44}$$

The torque then becomes:

$$T_{\nabla u} = \frac{1}{3}(2F_{\nabla u12} - F_{\nabla u23})b\cos\lambda \tag{2.45}$$

$F_{\nabla u12}$, $F_{\nabla u23}$: resulting forces on the upper and lower section of the particle, respectively (refer to figure 2.13) $[N]$

b:particle major semi-axis $[m]$

λ: $\frac{\pi}{2} - \alpha_i$ $[rad]$

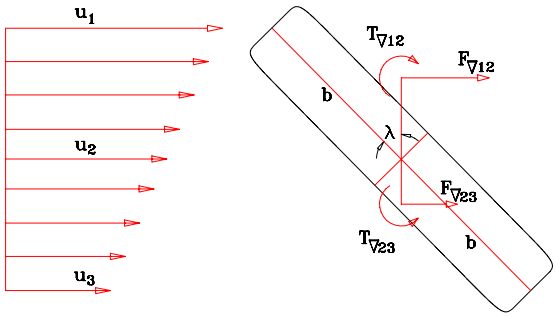

Figure 2.13: A large particle subject to a macroscopic velocity gradient, causing a resulting moment about the minor axis.

Pitching moment

The pitching moment is a common factor in aerofoil theory, and stems from the lift and drag forces. Referring to figure 2.10, it is immediately apparent that the lift and drag forces, which act in the aerodynamic centre, will give rise to a torque about the minor axis of the particle. Although it is a common assumption that the aerodynamic centre is located a distance behind the leading edge corresponding to $0.25 \times chord\ length$, this distance is in reality a function of incidence angle and profile shape. For aerodynamic profiles, it is common to include this in a coefficient-formulation, akin to the lift and drag forces, so that the pitching moment becomes the product of a coefficient, the dynamic pressure and area, on which it acts. However, such a coefficient representation is not possible for arbitrary particles, as correlations simply do not exist.

Another approach is to re-use the crossflow principle (although still keeping in mind the limitation of this principle to $Re_p \leq 10^3$) to define the pitching force. Referring, once again, to figure 2.10, the normal force coefficient, C_N, can be written as:

$$C_N = C_D \sin^2\alpha_i \tag{2.46}$$

The pitching force thus becomes:

$$\vec{F}_{pitch} = \frac{1}{2}C_N\rho_g A_{\alpha_i}|\vec{u}_g - \vec{v}_p|(\vec{u}_g - \vec{v}_p) \tag{2.47}$$

What remains now is to define the centre of pressure (or aerodynamic centre) for arbitrary particles and incidence angles. The limiting cases are (see figure 2.14):

- At $\alpha_i = 0$ $[rad]$, $\beta \neq 1$, the centre of pressure of a regular body of revolution is located at $0.5 \times major\ axis$ from the leading edge, i.e. at the particle centre of mass.
- At $\alpha_i = \frac{\pi}{2}$ $[rad]$, $\beta \neq 1$, the centre of pressure of a regular body of revolution is located at $0.0 \times major\ axis$ from the leading edge, i.e. at the particle centre of mass.
- For $\beta = 1$ and all values of α_i, the centre of pressure is located at the particle centre of mass.

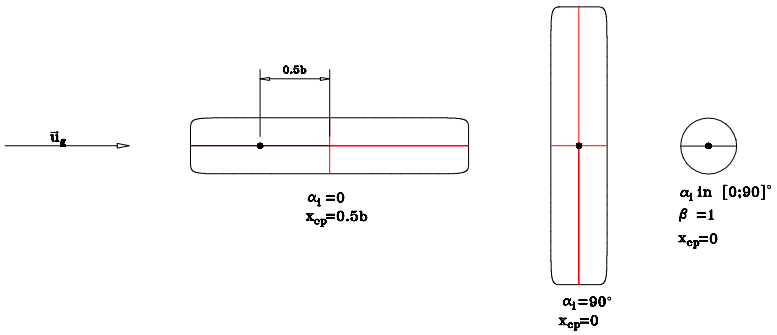

Figure 2.14: Centre of pressure for $\alpha_i = 0$ and $\alpha_i = 90$ degrees for particles with $\beta = 10$ and $\beta = 1$.

Assuming an exponential dependency of the location of the centre of pressure on the aspect ratio β, and a $\sin^3$ dependency on incidence angle, the location of the centre of pressure is:

$$x_{cp} = 0.5b[1.0 - \exp(1.0 - \beta)](1.0 - \sin^3 \alpha_i) \tag{2.48}$$

Figure 2.15 and 2.16 shows eq. 2.48 as a function of incidence angle and aspect ratio, respectively. Finally, the pitching moment can be written as:

$$\vec{T}_{pitch} = \vec{F}_{pitch} x_{cp} \tag{2.49}$$

2.5 Interaction of particles and fluid structures

2.5.1 Turbulent dispersion

Most engineering flows can be classified as turbulent. This is particularly true of the flow in most pulverised fuel burners, which utilize the high degree of turbulence generated through swirling one or more of the burner air streams to obtain a high level of mixing. This high degree of turbulence is also felt by the dispersed phase as a combination of a stochastic change in velocity and a misalignment of particle and fluid trajectories.

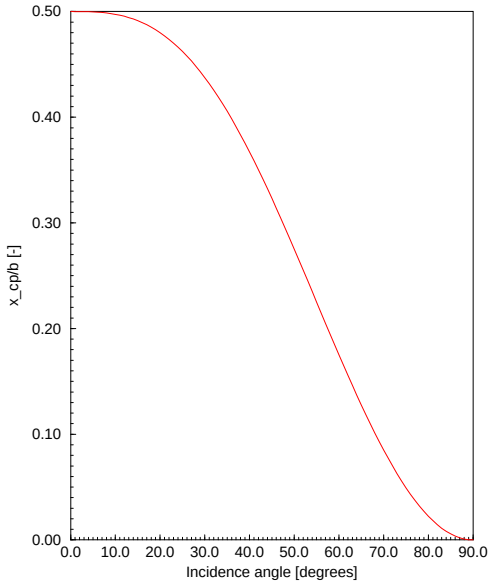

Figure 2.15: Location of centre of pressure as a function of incidence angle. $\beta = 10.0$.

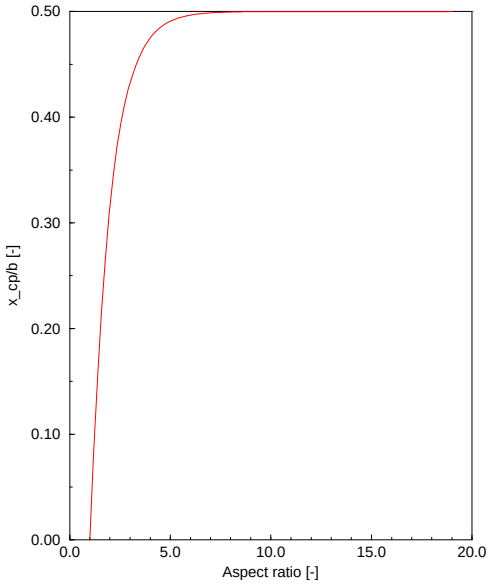

Figure 2.16: Location of centre of pressure as a function of aspect ratio β. $\alpha_i = 0$.

Turbulent particle dispersion is one of the primary research topics in gas- particle flows, particularly when the coupling between the phases in terms of gas turbulence modulation is included (see, for instance, Kenning and Crowe (1997) for a recent review of this subject). However, figure 2.17, which shows the impact of turbulence modulation using the models of Shuen et al. (1985) and Mostafa and Mongia (1988) in previous calculations of the Risø tunnel furnace using a spherical particle model (see Zachariassen and Rosendahl (1994)), indicates that as far as engineering models of reacting multiphase environments are concerned, the inclusion of turbulence modulation is perhaps of lesser importance, accounting locally for less than 2% of the advection coefficients of equation 1.2.

	Shuen et al. (1985)	**Mostafa and Mongia (1988)**
k equation	$S_k = \bar{u}\bar{S}_{pu} - \bar{u}\bar{S_{pu}}$	$S_k = 2kf\alpha_p\left(1 - \frac{\tau_L}{\tau_L+\tau_p}\right)$
ε equation	$S_\varepsilon = -2C_{\varepsilon 3}\mu_t\frac{\varepsilon}{k}\frac{\partial \bar{S_{pu}}}{\partial r}$	$S_\varepsilon = -C_{\varepsilon 3}\frac{\varepsilon}{k}S_k$

S_{pu}: momentum source term due to the presence of particles $[N]$

$\bar{u}\bar{S_{pu}}$: time averaged product of instantaneous velocity and momentum source term $[Nm/s]$

$\bar{u}\bar{S}_{pu}$: product of time averaged velocity and momentum source term $[Nm/s]$

$C_{\varepsilon 3}$: constant in the interval 0.1-5.0 [.]

μ_t: turbulent viscosity $[m^2/s]$

τ_L: carrier phase Lagrangian time scale $[s]$

τ_p: aerodynamic response time $[s]$

f: friction coefficient $[-]$

α_p: volumetric particle concentration $[m^3/m^3]$

Table 2.2: Source term formulations for turbulence modulation models.

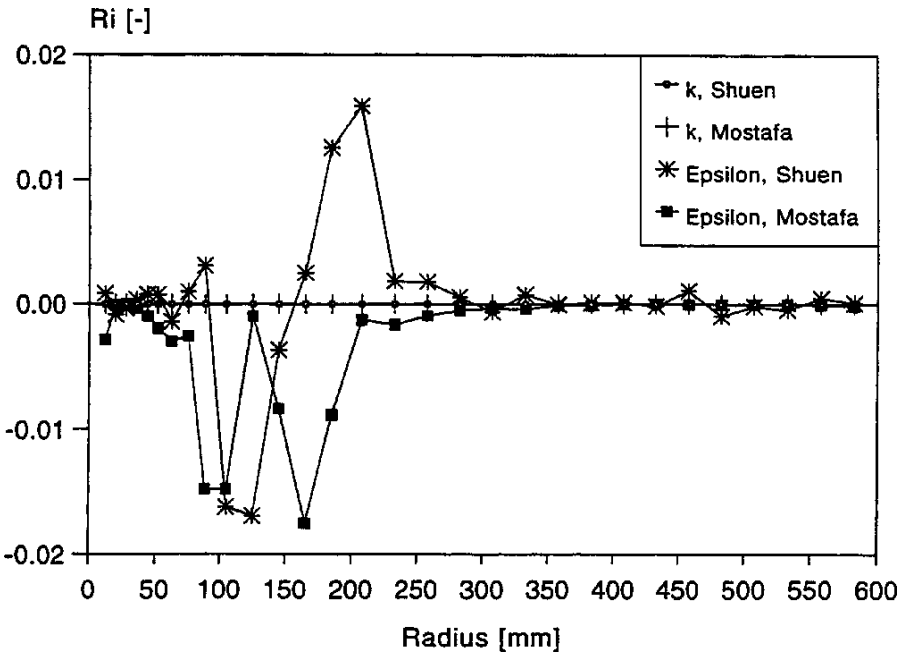

Figure 2.17: Turbulence modulation results just outside the quarl mouth of the Risø tunnel furnace ($x = 250mm$). The ratio R_i is defined as $\frac{S}{a_p}$ for source terms including the dependent variable and $\frac{S}{a_p \phi_p}$ for source terms not including the dependent variable. a_p is the coefficient at point p (see equation 1.2). From Zachariassen & Rosendahl (1994).

One of the oldest and most widely used dispersion models is the eddy lifetime model of Shuen et al. (1983). The model is isotropic in space, and assumes that a particle is influenced by an eddy over a period corresponding to the eddy's lifetime or the particle transit time, whichever is smallest. The strength of the eddy is given through a Gaussian distribution with standard deviation $\sigma = \sqrt{\frac{2}{3}k}$. Assuming that the characteristic eddy size is the dissipation length scale l_e, the eddy lifetime becomes

$$t_e = \frac{l_e}{\sqrt{\frac{2}{3}k}} \tag{2.50}$$

l_e: characteristic eddy length scale $[m]$, given by

$$l_e = C_\mu^{0.75} \frac{k^{1.5}}{\varepsilon} \tag{2.51}$$

$C_\mu^{0.75}$: constant from the $k - \varepsilon$ turbulence model

The other limiting parameter, the transit time t_t, is found from

$$t_t = -\tau_p \ln \left(1 - \frac{l_e}{\tau_p |\vec{u_g} - \vec{v_p}|} \right) \tag{2.52}$$

The eddy lifetime model in its current form suffers from a number of shortcomings. It does not consider temporal and spatial effects, e.g. from misalignment of trajectories, and assumes that the particle is much smaller than the eddy infuencing it's velocity, such that the particle is only influenced by one isotropic eddy. For small particles, this is not entirely unreasonable, as the smaller eddies approach isotropy, and less size classes of eddies exist within the eddy represented by the eddy lifetime model. However, for larger particles, the eddy lifetime model becomes increasingly inaccurate, not only due to the particle overlapping several eddies, but also due to the anisotropy of the fluctuating components of most turbulent flows. For several types of flow, especially swirling flows, large scale turbulence is strongly anisotropic, and as the particles increase in size, they are affected by this anisotropy.

More advanced models, such as that by Zhou and Leschziner (1991), account for this anisotropy by determining the fluctuating velocity as the sum of a time- correlation part and a non-correlated part.

2.5.2 Large particles subject to local fluid structures

When considering particles of size classes of the order of millimeters or centimeters, it is necessary to modify the form of the fluid velocity used in the force and torque expressions. Referring to figure 2.18, it is immediately apparent, that the situation indicated will give rise to a non- constant local drag and lift on the particle surface as well as a moment due to uneven loading on the surface.

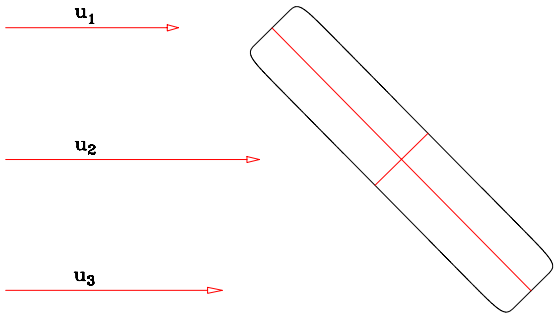

Figure 2.18: A large particle subject to a macroscopic velocity gradient.

The fluid velocity to be used in this situation is given by partial integration along the major particle axis y':

$$\tilde{\vec{u}} = \frac{\int_0^{2b} \vec{u}_g \partial y'}{2b} \tag{2.53}$$

Numerically, this would correspond to evaluating the slip velocity at more than one location, or station, along the particle major axis, as shown in figure 2.19. At stations

not coincident with the center of mass, the rotational velocity of the particle has to be included in the determination of the local slip velocity such that, referring to the symbols in figure 2.19:

$$u_r = |\vec{u}_g| \pm \frac{\Omega r}{2\pi} \sin \alpha_i \tag{2.54}$$

u_r: slip velocity $[m/s]$

$\vec{u}_g$: gas velocity vector $[m/s]$

Ω: angular velocity $[rad/s]$

r: distance along major particle axis from centre of mass to evaluation station $[m]$ (see figure 2.19)

α_i: incidence angle $[rad]$

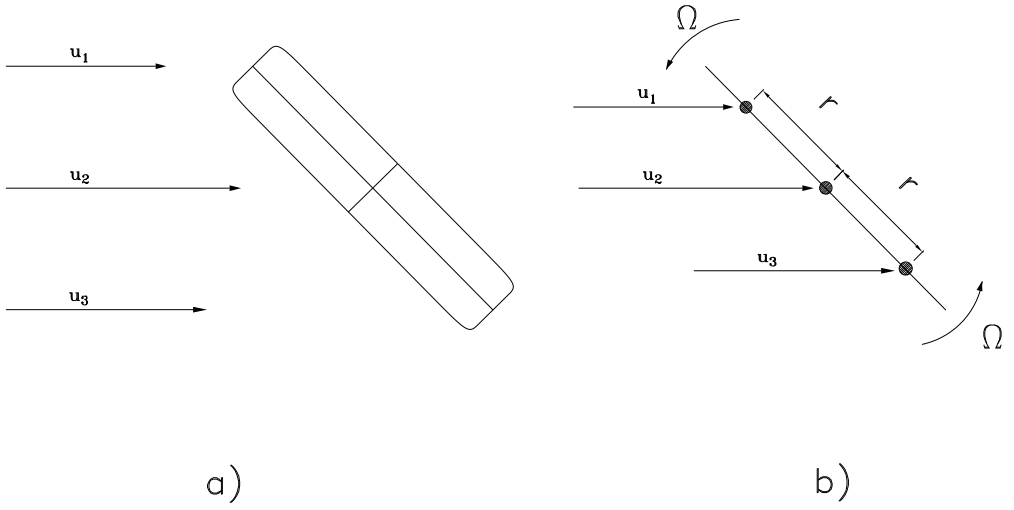

Figure 2.19: Determination of slip velocity at multiple stations. a) shows the original particle, b) the stations at which the velocities might be determined.

Due to the added computational effort involved in this, it is desirable to set up a criterion to evaluate the necessity for this for the individual particle. Such a criterion could be based on the turbulent length scale of the flow:

$$n_u = \frac{L_h}{2b} = \frac{C_\mu^{0.75} k^{1.5}}{2b\varepsilon} \tag{2.55}$$

L_h: turbulent length scale of the flow $[m]$

b: particle major semi-axis $[m]$

$C_\mu^{0.75}$: constant used for calculating the turbulent viscosity. Default 0.09 $[-]$

k: turbulent kinetic energy $[m^2/s^2]$

ε: turbulent dissipation $[m^2/s^3]$

A suitable limit for n_u would then be:

$$n_u \quad \begin{cases} < 2.5 & \textit{Multiple stations} \\ \geq 2.5 & \textit{Single station} \end{cases} \tag{2.56}$$

2.6 Influence of combustion on particle aerodynamics

Particles undergoing chemical reactions with the surrounding gas often experience a change in their aerodynamic behaviour. As gas - volatiles being released, oxygen flowing to the surface of the particle or combustion products flowing away from the surface - moves away or toward the particle, the structure of the boundary layer changes, causing the drag and lift forces to change. For spherical particles, this is often accounted for by assuming a symmetrical secondary flow field around the particle (Stefan flow), and the drag coefficient is modified using a form of mass Peclet number, in a simple manner similar to the Nusselt number (see Appendix 3) or possibly in more complex correlations as given by, for example, Sirignano (1993) or Chiang et al. (1992) (see Kær and Nielsen (1996) for a discussion of these models).

For a non-homogeneous particle such as straw, the above assumption of spherical symmetry is unapplicable when attempting to account for aerodynamic changes due to combustion. Not only the non-sphericity of the particle, but also the non- homogenity of the straw and temperature differences of the surrounding fluid, will account for localised jets, which influence the orientation of the particle and hence the motion. Furthermore, the fluid temperature differences will be felt by the particle as a force due to the density gradient of the fluid.

Needless to say, accounting for the complex mechanisms of combustion in systems of biomass fuels involves an excessive and prohibitive amount of detail of each individual particle, and is therefore inapplicable in an engineering model based on current computer resources.

2.7 Non-spherical particle tracking methodology

In order to sum up, the following is a step-by-step description of the current model.

1. Determine the aspect ratio β, the minor axis a and the superelliptic exponent n, in order to define the shape of the particle.
2. Calculate the superelliptical area and volume of the particle.
3. Determine the initial orientation, angular and translational velocities and starting position of the particle.
4. Determine an initial time step.
5. Calculate the incidence angles of the three velocity components (eq. 2.10).
6. Calculate the local fluid velocity.
7. Calculate the particle Reynolds number (eq. 2.26) in all three directions.

8. Determine the drag coefficient (eq. 2.31) and lift coefficient (eq. 2.32).
9. Calculate the coefficients $c1$, $c2$ and $c3$ of eq. 2.6 for translation to include the desired forces.
10. Use eq. 2.6 to determine the new velocity components of the particle.
11. Use eq. 2.7 to determine the new position of the particle.
12. Determine the normal force coefficient (eq. 2.46).
13. Calculate the moment arms of the particle (eq. 2.48).
14. Calculate the local fluid vorticity.
15. Calculate the coefficients $c1$, $c2$ and $c3$ of eq. 2.6 for rotation to include the desired torques.
16. Use eq. 2.6 to determine the new rotational components of the particle.
17. Use eq. 2.7 to determine the new orientation of the particle.
18. Repeat steps 4-17 until a predetermined stop criterion is reached.

2.8 Summary

This chapter contains the aerodynamic modelling foundation for single superelliptic particles, based on a combination of existing measurements on different particle shapes, and a geometry based interpolation between these shapes to obtain drag and lift data for the superelliptic shape of interest.

A number of forces are introduced, and for som the formulation is uncertain and tentative, pending further analytical and experimental analysis. Also, an investigation akin that of Rusaas (1998) regarding the relative importance of the different forces, and following the discussion of the previous sections, would be very helpful as a further step in the formulation of the equations of motion of non-spherical particles.

Incidence angle variations are based on an assumed third power Sine relationship between the drag and lift coefficients at zero and right angles of incidence. Finally, the profile lift is deduced from the drag using the cross-flow principle.

Turbulent dispersion is included using an un-modified eddy lifetime model.

The implementation of the models developed in this chapter is discussed in Appendix B, as are the additional models, such as wall collisions, time stepping, etc., necessary for a complete Lagrangian simulation tool.

.

Chapter 3

Particle combustion

As the particle enters the combustion chamber, a number of processes occur (these are indicated in figure 1.4). The first process to start is that of devolatilization and evaporation of water vapour, followed by the heterogeneous combustion of the particle. As shown on figure 1.4, some overlap between these processes occurs toward the end of devolatilization, when the flux of volatile gases from the particle surface abates enough to allow oxygen to flow to the surface.

In terms of the models used, there are a couple of important points to be made:

- Throughout the following, it will be assumed that there is a homogeneous temperature profile within the particle, such that particle and surface temperature are identical, and may be interchangeable.

- As all models have been developed based on spherical particles, around which there are homogeneous conditions, this will be assumed to apply also to non-spherical particles.

Another important aspect is that the predominant amount of work done on particle combustion has concerned pulverised coal combustion. Regarding straw, or even the more general area of biomass, almost no data or models are available, and very little information on the reaction schemes of both the homogeneous and heterogeneous reactions occuring around and on biomass particles can be found. Thus, for the most part, the following consists of well-proven models for the devolatilization and combustion of high volatile coals - it is assumed, that, using appropriate parameters, these can represent the devolatlization and combustion of biomass particles as well.

3.1 Devolatilization

Devolatilization occurs when the particle temperature becomes high enough to raise the energy level of the volatile gas within the particle to such a level that it is able to break free and leave the particle. During this process, some coal particles increase their diameter - swell - whilst becoming more porous, as the escaping gases rip the particle up, and even carrying away solid carbon. The diameter change due to pyrolysis is described in section 3.5.1. The importance of accurately modelling the pyrolysis process has been subject to a lot of discussion, with different investigators arguing diametrically opposite standpoints (Lau and Niksa 1992), (Niksa 1995), (Rasmussen 1986). What remains indisputable, however, is that due to the very short time-span of devolatilization, the quality of the pyrolysis model is directly linked to the grid spacing at the burner mouth, where this process takes place. If a relatively coarse mesh is used, the effect of the devolatilization on the fluid phase will be transferred as source terms in the centre of the few cells traversed during devolatilization, and much detail will thus be lost. If, however, a fine mesh is used, and interest is focused on this process and the dispersion and combustion location of the volatile gases, a more detailed pyrolysis model is appropriate.

Another factor influencing the choice of devolatilization model is the amount of volatiles in the solid fuel. For straw, volatiles account for up to 70% of the mass of the straw, and therefore devolatilization becomes more important than for coal, which at most has approximately 30% volatile mass.

Devolatilization is commonly assumed to follow a first order reaction, regardles of model complexity:

$$\frac{dV}{dt} = k_v(m_{v0} - m'_v) \tag{3.1}$$

m'_v: amount of volatiles released from the particle $= \frac{m_{v0}-m_v}{m_{v0}}$ $[-]$

m_{v0}: total mass of volatiles to be released $[-]$

3.1.1 Single equation Arrhenius pyrolysis model

Proposed by Badzioch and Hawksley (1970), this is one of the most simple pyrolysis models, assuming that the volatile gases can be described as a single gas with a single devolatilization rate based on an activation energy and a pre-exponential factor:

$$K_v = A_v \exp\left(-\frac{E_v}{R_v T_p}\right) \tag{3.2}$$

A_v: pre-exponential factor $[s^{-1}]$

E_v: activation energy $[J/kg]$

R_v: volatile gas constant $[J/kgK]$

T_p: particle temperature $[K]$

Despite its simplicity, the single equation Arrhenius model has the characteristics of more complex models, it's main shortcoming being the single volatile gas assumed.

3.1.2 Distributed Activation Energy (DAE) model

The DAE model is essentially an extension of the Arrhenius model, introducing a measure of stochasticity in the rate expression to account for variations within the fuel particles as well as allowing for multiple components in the volatile gas:

$$K_v = A_{v,i} \exp\left(-\frac{\hat{E}_{v,i}}{R_{v,i}T_p}\right) \tag{3.3}$$

index i: each volatile component considered

$\hat{E}_{v,i}$: normally distributed activation energy $[J/kg]$ with deviation $\sigma_{v,i}$ and mean $E_{v,i}$

This model is intended to be used when a complex volatile composition is considered, where two or more components - although chemically identical - can have chemical bonds of different strengths, and thus their devolatilization behaviour differs (Serio et al. 1987). The implementation of the DAE model in the current work only allows for a single volatile component.

3.2 Solid combustion

The solid combustion models in the following are all derived using a spherical particle shape, and, except the Reactivity Index Model, they all consider the reaction to be a function of the surface area of the particle. One main reason for the spherical formulation is that spherical symmetry can be assumed for each particle, simplifying the derivations considerably. Furthermore, it is very difficult - in an engineering context even impossible - to generalize for example the distribution of oxygen at the surface of a particle which is not spherical.

As one of the main features of the current model is the superellipsoidal shape, which, although able to, only in specific cases is cast as spheres, special treatment is necessary to preserve the validity of the combustion models. Thus, a *mean diameter based on surface area* $\bar{d}_p$ is defined, such that a fictitious spherical particle, with the same surface area as the superellipsoid it represents, is used during the combustion calculations:

$$\bar{d}_p = \sqrt{\frac{A_s}{\pi}} \tag{3.4}$$

It is important to emphasize that this diameter is **only** used to predict the rate of change of the particle composition; the particle dimensions used for all other calculations, such as the tracking, are based on the volume of the particle.

3.2.1 Mixed control model

Being one of the most used coal combustion models, the mixed control model (or Field model) assumes that the slower of two rates govern the reaction speed, the rate of oxygen diffusion to the particle surface and the kinetic reaction rate of the char and oxygen reaction at the surface.

In the range up to 1650K, the kinetic reaction rate is described by an Arrhenius equation (Smoot and Smith 1985):

$$K_k = A_k \exp\left(-\frac{E_k}{R_c T_p}\right) \tag{3.5}$$

R_c: carbon gas constant $[J/kgK]$

A_k: pre-exponential factor $[kg/(m^2 sPa)]$

Above 1650K, the standard Arrhenius expression yields excessive rates, and a linear relationship based on temperature is used (Smoot and Smith 1985):

$$K_k = -4.84 \times 10^{-2} + 3.80 \times 10^{-5} T_p \tag{3.6}$$

The bulk diffusion rate is defined as (Zachariassen and Rosendahl 1994):

$$K_D = \frac{2 M_c \phi D}{\bar{d}_p R T_m} \tag{3.7}$$

M_c: carbon molecular mass $[kg/mol]$

ϕ: stoichiometry factor in the reaction 3.8. $\phi = 2$ if the product is CO and $\phi = 1$ if the product is CO_2. $[-]$

$$\phi C + O_2 \rightarrow 2(\phi - 1)CO + (2 - \phi)CO_2 \tag{3.8}$$

$\bar{d}_p$: mean particle diameter based on surface area (equation 3.4) $[m]$

R: universal gas constant $[J/kgK]$

T_m: arithmetic mean temperature between particle and surrounding fluid $[K]$

D: diffusion coefficient of oxygen in the bulk gas $[m^s/s]$, at constant pressure given by:

$$D = D_0 \left(\frac{T_m}{T_0}\right)^{1.75} \tag{3.9}$$

$D_0 = 3.49 \times 10^{-4} [m^2/s] \;\; at \; T_0 = 1600[K]$

These rates, which are functions of particle surface area and oxygen partial pressure, are weighted and combined to form the rate of carbon consumption:

$$\frac{dm_c}{dt} = \left(\frac{1}{K_k} + \frac{1}{K_D}\right)^{-1} p_{O_2} A_s \tag{3.10}$$

p_{O_2}: oxygen partial pressure $[Pa]$

A_s: particle surface area $[m^2]$

m_c: mass of char in the particle $[kg]$

3.2.2 Gibb's model

Gibb's combustion model (Gibb 1985) is one of few to include pore diffusion in the formulation of the char conversion rate. The conversion rate is assumed to depend on three seperate rates, the rate of oxygen diffusion to the particle surface, the surface kinetic reaction rate and the internal rate of diffusion and reaction. The first two are defined in a non-conventional manner:

$$K_D = \frac{4D}{\bar{d}_p^2} \tag{3.11}$$

$$K_k = \frac{(1-\varepsilon_{Gk})}{\bar{r}_p} A_{Gk} T_p \exp\left(-\frac{T_{Gk}}{T_p}\right) \tag{3.12}$$

D: oxygen diffusion coefficient, given by equation 3.9 $[m^2/s]$

ε_{Gk}: particle void fraction $[-]$

A_{Gk}: pre-exponential factor $= 14.0$ $[m/s]$

T_{Gk}: activation temperature $= 21580$ $[K]$

The third, and most complex, rate is the internal diffusion and reaction rate. Gibb (1985) expresses it as:

$$K_{Gk} = A_{Gk} T_p \exp\left(-\frac{T_{Gk}}{T_p}\right) \frac{F(\beta)}{a_{Gk}} \tag{3.13}$$

a_{Gk}: mean pore size $[nm]$

$$F(\beta) = \frac{(\beta \coth \beta - 1)}{\beta^2} \tag{3.14}$$

$$\beta = \bar{r}_p \sqrt{\frac{A_{Gk} T_p \exp\left(-\frac{T_{Gk}}{T_p}\right)}{D_{Gk} \varepsilon_{Gk} a_{Gk}}} \tag{3.15}$$

D_{Gk}: pore diffusion coefficient, typically an order of magnitude less than D $[m^2/s]$

Typical values for high volatile coal particles are a void fraction of 0.5 and pore size of 5 $[nm]$. With this, the rate of char conversion according to Gibb's model can be written as:

$$\frac{dm_c}{dt} = \frac{3\phi M_C \rho_g}{(1-\varepsilon_{Gk}) M_{O_2} \rho_C} \left(\frac{1}{K_D} + \frac{1}{K_k + K_{Gk}}\right)^{-1} \tag{3.16}$$

3.2.3 Reactivity index model

The reactivity index model is a new model, developed at the Department of Combustion Research at Risø National Laboratory, Denmark, which can be applied to a wide range of pulverised fuels, as its development is not based on coal (as is true of the two preceding models discussed).

The model is based on a reference reactivity profile of the solid fuel, which is determined experimentally with well-defined reference temperatures and partial oxygen pressures. The reference profile is then approximated with a form based on the appropriate pore or grain model (Sørensen et al. (1994) and Sørensen (1996)):
Random grain model:

$$R_{ref} = \frac{a_{rim}}{1-X}\frac{\epsilon_0 + (1-\epsilon_0)X}{\epsilon_0}\left(\frac{\ln(\epsilon_0 + (1-\epsilon_0)X)^{\alpha}_{rim}}{\ln(\epsilon_0)}\right)\exp(-b_{rim}X) \tag{3.17}$$

Random pore model:

$$R_{ref} = a_{rim}\left(1 + \frac{\ln(1-X)}{\ln(1-\epsilon_0)}\right)^{\alpha}_{rim} \tag{3.18}$$

Whilst the total conversion rate is still governed by the slower of the oxygen diffusion and kinetic reaction rates, it is the latter which is re-formulated in the reactivity index model.

The rate of carbon conversion is given as (Jensen, Stenholm, and Jørgensen 1994):

$$\frac{1}{1-X}\frac{dX}{dt} = f(X)k_0\exp\left(-\frac{E_{rim}}{RT_p}\right)p_{O_2}^{n_c} \tag{3.19}$$

X: converted mass fraction of char, $\frac{m_{c0}-m_c}{m_{c0}}$ $[-]$
p_{O_2}: oxygen partial pressure $[Pa]$
n_c: reaction order $[-]$
$f(X)$: change in reactivity
k_0: frequency factor
ϵ_0: initial porosity $[-]$

The product $f(X)k_0$ is given as a polynomium:

$$f(X)k_0 = a_1 + a_2X + a_3X^2 + a_4X^3 \tag{3.20}$$

with the coefficients $a_1 - a_4$ depending on the type of fuel.

In the complete formulation of the model, the mixed control concept is utilized, allowing for diffusion control. Equation 3.19 is re-written to express the kinetic rate of char conversion:

$$\frac{dm_c}{dt} = m_c f(X)k_0\exp\left(-\frac{E_{rim}}{RT_p}\right)p_{O_2}^{n_c} \tag{3.21}$$

Then, the total rate of change of carbon is defined using the conversion rate due to diffusion alone and the above expression for the rate of change due to fuel reactivity:

$$\frac{dm_c}{dt} = \left(\frac{1}{K_D p_{O_2} A_s} + \frac{1}{m_c f(X) k_0 \exp\left(-\frac{E}{RT_p}\right) p_{O_2}^{n_c}} \right)^{-1} \tag{3.22}$$

3.3 Combustion products

Measurements have shown that the composition of the combustion products changes with temperature, with the $C + O_2 \rightarrow CO_2$ reaction dominating in the lower temperature regimes, and the $2C + O_2 \rightarrow 2CO$ reaction dominating in the upper regimes. The ratio f of the two products can be shown to follow an Arrhenius expression (Biede, Sørensen, and Peck 1992):

$$f = \frac{moles\ CO}{moles\ CO_2} = A_\Gamma \exp\left(-\frac{E_\Gamma}{RT_p}\right) \tag{3.23}$$

Equation 3.23 must now be introduced into equation 3.7, as the stoichiometry factor of that equation, ϕ, no longer remains constant. ϕ can be expressed as:

$$\phi = \frac{2(f+1)}{2+f} \tag{3.24}$$

3.4 Stefan flow

Stefan flow is commonly associated with the flow near the surface of submerged ice. It is defined as a secondary flow, issuing from a solid surface, entering the primary flow at right angles (see figure 3.1). This situation also arises in particle combustion, as volatile gases and combustion products leave the particle surface and flow into the primary flow of the surrounding gases.

Based on film theory (Bird, Stewart, and Lightfoot 1960), Rasmussen (1986) has developed a model to include Stefan flow in the reaction rate formulation. However, this model only considers the flow of volatiles from the particle surface, and in the following, the total flow, consisting of volatile gases, water vapour and combustion products, is included.

The mass flow of gases at the surface of the particle is equal to the mass flow at radius r, allowing the flux at this radius J_t to determined:

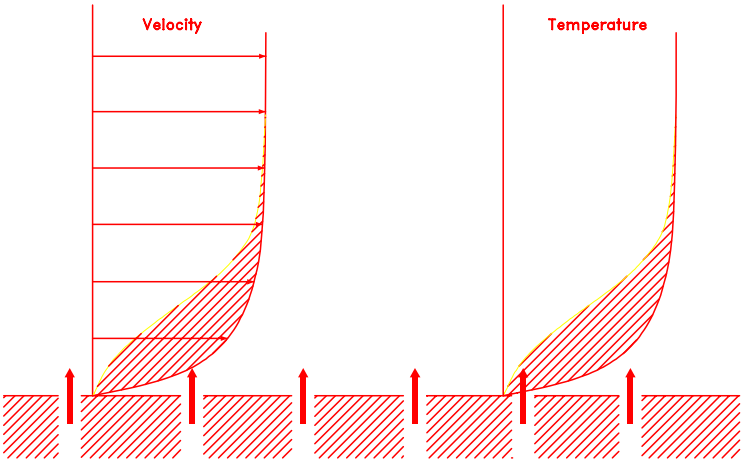

Figure 3.1: Schematic representation of Stefan flow. The primary flow profiles parallel to the porous surface are influenced by secondary flow through that surface.

$$\begin{aligned} 4\pi\bar{r}_p^2 J_0 &= 4\pi r_p^2 J_t \\ J_t &= J_0 \frac{\bar{r}_p^2}{r^2} \end{aligned} \tag{3.25}$$

$\bar{r}_p$: mean particle radius based on surface area (equation 3.4) $[m]$

r: radial distance from centre of particle $[m]$

J_0: gas flux at particle surface $[kg/m^2 s]$, consisting of volatile flux (J_v), water vapour flux (J_{H_2O}) and combustion products flux (J_{cs})

Utilizing Fick's law of diffusion, the flow of oxygen to the particle can be expressed as:

$$(u_{O_2} - u_t)\rho_{O_2} = -D\frac{d\rho_{O_2}}{dr} \tag{3.26}$$

u_{O_2}: oxygen velocity away from the particle $[m/s]$

u_t: gas flow velocity away from the particle $[m/s]$

ρ_{O_2}: oxygen density at the arithmetic mean temperature $[kg/m^3]$

D: diffusion coefficient $[m^2/s]$

Rearranging equation 3.26, using the ideal gas equation, the oxygen flux can be determined in terms of the flux of gases away from the particle, and, finally, a non-dimensional mass transfer parameter can be defined:

$$b' = \frac{(J_v + J_{H_2O} + J_{cs})\bar{r}_p}{D\rho_g} \tag{3.27}$$

ρ_g: density of surrounding gas at the arithmetic mean temperature $[kg/m^3]$

This non-dimensional transfer parameter, which essentially is a mass-Peclet number, can now be used in the mass transfer rate equations of the different models, each of which subsequently takes the following form:

- The Mixed Control model (equation 3.10):

$$\frac{dm_c}{dt} = \left(\frac{\exp(b')}{K_k} + \frac{\exp(b') - 1}{b' K_D} \right)^{-1} p_{O_2} A_s \tag{3.28}$$

- Gibbs model. Stefan flow not implemented in the current version of PCOMBUST.
- Reactivity Index model. Stefan flow not implemented in the current version of PCOMBUST.

Stefan flow also influences the convective heat transfer rate, which is governed by the Nusselt number. The Nusselt number can be expressed empirically as (Crowe et al. 1977):

$$Nu = 2 + 0.654 Re_p^{0.25} Pr^{0.33} \tag{3.29}$$

Re_p: particle Reynolds number [–]

Pr: Prandtl number, evaluated at the arithmetic mean temperature [–]

Rather than using film theory to correlate the Nusselt number with Stefan effects (film theory fails when slip velocities become large), an empirical correlation is used (Smoot and Smith 1985):

$$Nu' = Nu \exp(-0.6 b') \tag{3.30}$$

3.5 Diameter changes

In this section, the size changes in the particle will be related to the minor axis dimension, which henceforth will be termed the particle diameter.

3.5.1 Swelling

During devolatilization, it is common for certain coal types, bituminous coal in particular, to swell, sometimes to a size twice the original. The extent of the swelling is expressed by the swelling index, such that the diameter as a function of this index and the stage of the devolatilization process is:

$$d_p = d_{p0}\left[1 + (\gamma - 1)\frac{m_{v0} - m_v}{m_{v0}}\right] \tag{3.31}$$

γ: particle swelling index $[-]$

m_v: mass fraction of volatiles in the particle at the time of evaluation $[-]$

m_{v0}: mass fraction of volatiles in the particle at time $t = 0$ $[-]$

d_{p0}: initial particle diameter $(2a_0)$ at time $t = 0$ $[m]$

3.5.2 The extended shrinking core model

The shrinking core model of Yagi and Kunii from 1955 (Levenspiel 1972) is one of two models commonly used to describe particle combustion, the other being the progressive conversion model, which is only applicable at low temperatures. The progressive conversion model assumes, that the carbon and oxygen reaction takes place within the particle matrix, considering the kinetic reaction the rate limiting factor. Thus, the particle burns in a volumetric homogeneous manner, leaving the diameter unchanged whilst the particle composition is changed, ultimately into an ash particle.

In most furnace environments, the temperatures are high enough that typically the kinetic reaction will not be the rate limiting factor, but rather the oxygen diffusion to the particle surface. Thus, the carbon+oxygen reaction takes place at the particle surface, with limited diffusion into the matrix, and the diameter of the particle will decrease, as more and more carbon is removed from the particle. Ultimately, all that will be left is ash, and the reaction will stop.

Assuming constant density during heterogeneous combustion, the shrinking core model establishes the following relation between instantaneous and initial particle diameter:

$$\frac{d_p}{d_{p0}} = \left(\frac{V_p}{V_{p0}}\right)^{1/3} \tag{3.32}$$

V_p: particle volume $[m^3]$

V_{p0}: initial particle volume $[m^3]$

Re-expressing the above equation in terms of mass fractions, and including it in equation 3.31, the final form of the instantaneous particle diameter becomes:

$$d_p = d_{p0}\left[1 + (\gamma - 1)\frac{m_{v0} - m_v}{m_{v0}}\right]\left(\frac{m_a + m_c}{m_a + m_{c0}}\right)^{1/3} \tag{3.33}$$

m_{v0}, m_v: initial and instantaneous volatile mass $[kg]$

m_a: ash mass $[kg]$

$m_c c0, m_c$: initial and instantaeous fixed carbon mass $[kg]$

As can be seen in figure 3.2, this relationship is also valid for superellipsoids with constant n and aspect ratio.

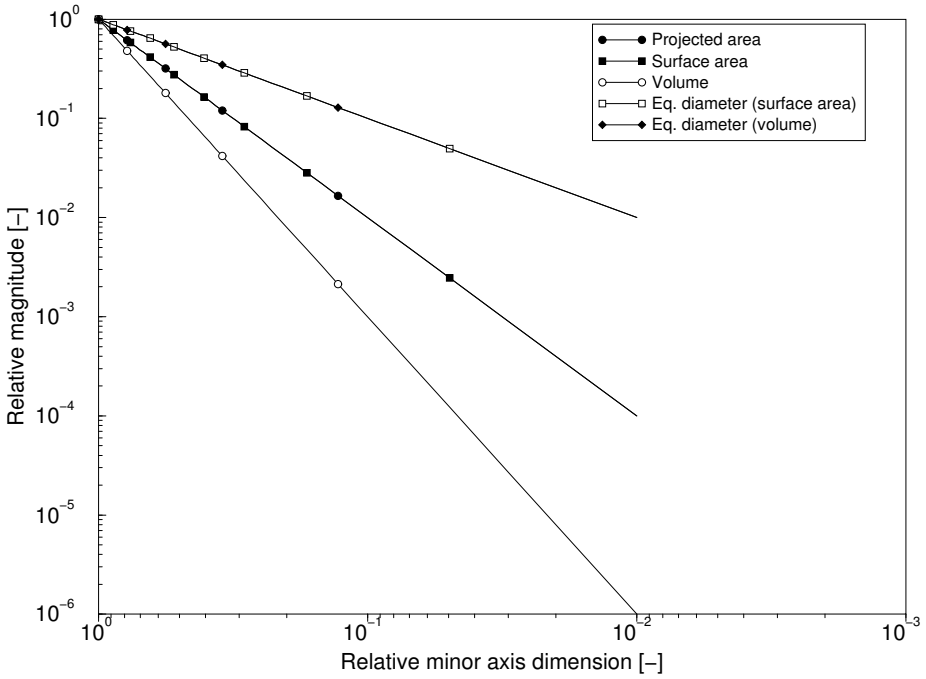

Figure 3.2: Relative volume ($\frac{V}{V_0}$) and areas ($\frac{A}{A_0}$) as functions of the relative axis size ($\frac{a}{a_0}$). Equivalent spherical diameters based on surface area (eq. 3.4) and volume are also shown. All corroborate equation 3.32 for general superellipsoids.

3.6 Active surface correction

As the fixed carbon in the particle is consumed, a relatively greater amount of ash resides in the particle, creating non-reacting sections. This causes the surface reaction rate to slow down, as not all, and progressively less, of the surface is available for reaction. Rasmussen (1986) has proposed the following correction, which has been shown to be valid for coal:

$$S_{act} = \frac{m_c}{m_c + m_a} \tag{3.34}$$

The kinetic reaction rate is then multiplied by S_{act}:

$$K'_k = K_k S_{act} \tag{3.35}$$

to provide the form of the kinetic reaction rate used in the current model.

3.7 Heat balance

The particle heat balance includes radiative preheating and convective and reactive heat sources and sinks as well as sinks arising from devolatilization. Neglecting radiative preheating, it is written as:

$$m_p c_{pp} \frac{dT_p}{dt} = \frac{NuA_s\lambda}{\bar{d}_p}(T_g - T_p) + \frac{dm_v}{dt}h_{fg} + z_{pg}\frac{dm_c}{dt}H_{reac} \tag{3.36}$$

m_p: particle mass $[kg]$

c_{pp}: particle heat capacity (equation 3.39) $[J/kgK]$

Nu: Nusselt number as given be either equation 3.29 or 3.30 $[-]$

λ: convective heat transfer coefficient$[W/m^2K]$

T_g: gas temperature $[K]$

A_s: particle surface area $[m^2]$

$\frac{dm_v}{dt}$: rate of volatiles release $[kg/s]$

$\frac{dm_c}{dt}$: rate of fixed char release $[kg/s]$

h_{fg}: latent heat of the volatiles $[J/kg]$

H_{reac}: heat of reaction of the char+oxygen reaction $[J/kg]$

z_{pg}: fraction of heat of reaction to remain in particle $[-]$

Radiative preheating expresses the energy transferred to the particle through wall and gas radiation, and is mainly important during the early stages of the particle residence time. At this point, the particle is surrounded by the relatively cold transport air, and the rates of convective and reactive heat transfer are close to zero.

$$\dot{Q}_{rad} = \pi\varepsilon d_p^2 \left(I_p - \sigma T_p^4\right) \tag{3.37}$$

ε: emissivity $[-]$

I_p: radiative flux $[W/m^2]$

σ: Stefan-Boltzmann's constant $[W/m^2K^4]$

Radiative preheating is not included in the current formulation of the particle heat balance, but rather substituted by a less physical, but computationally faster, formulation as discussed in Appendix B.8.

Regarding the fraction of the heat of reaction, which remains in the particle, it is recommended that this be set to 0.3, if the product is CO, and 1.0, if the product is CO_2 (Boyd and Kent 1986). Like the other product-dependent parameters, it can be expressed as a function of the ratio of combustion products f:

$$z_{pg} = 1.0 - \frac{0.7}{1+f} \tag{3.38}$$

The particle specific heat capacity is determined as a function of composition and temperature:

$$c_{pp}(m_i, T) = \frac{m_c c_{pc} + m_v c_{pv}(T) + m_w c_{pw} + m_a c_{pa}}{m_p} \tag{3.39}$$

m_c: fixed carbon mass $[kg]$

c_{pc}: specific heat capacity of carbon $[J/kgK]$

m_v: volatiles mass $[kg]$

$c_{pv}(T)$: specific heat capacity of volatiles as a function of temperature $[J/kgK]$

m_w: water mass $[kg]$

c_{pw}: specific heat capacity of water $[J/kgK]$

m_a: ash mass $[kg]$

c_{pa}: specific heat capacity of ash $[J/kgK]$

The temperature dependent specific heat capacity of the volatile gases is determined using a polynomium representation (Biede, Sørensen, and Peck 1992).

3.8 Gas phase combustion

In a reacting gas-particle system, only part of the reactions occur as heterogeneous reactions on the surface or within matrix of the particles. Homogeneous reactions account for a large part of the processes occuring in such a system, as not only the volatile gases released, but also CO produced at high temperatures at the particle surface (cf. section 3.3), reacts with oxygen in the surrounding gas. For high volatile coals, the volatiles can account for up to 30% of the particle mass, and for straw even more than half the particle mass. As the combined heating values of the volatiles and CO are greater than for the char, homogeneous reactions normally account for the largest fraction of the total heat release in the system, and some attention should therefore be devoted to the modelling of the homogeneous reactions.

In order to achieve as much information as possible about the environment within the reacting gas-particle system, it does not suffice to employ a standard single- step combustion model. This only treats the total reaction of a general volatile gas to completely oxidized combustion products, such as H_2O and CO_2. An important quantity in combustion applications is the level of CO in the furnace, as this gives an indication of the combustion quality.

Consider the complete oxidation of an arbitrary hydrocarbon:

$$C_c H_h O_o + I O_2 \longrightarrow c CO_2 + \frac{h}{2} H_2 O \tag{3.40}$$

I: number of O_2 molecules required for complete combustion. $I = c + \frac{h}{4} - \frac{o}{2}$

This reaction can be divided into a hydrocarbon-to-carbon monoxide part and a carbon

monoxide-to-carbon dioxide part:

$$C_cH_hO_o + (I_1 + I_2)O_2 \longrightarrow cCO + \tfrac{h}{2}H_2O + I_2O_2 \longrightarrow cCO_2 + \frac{h}{2}H_2O \quad (3.41)$$

$$I_1 = \frac{c}{2} + \frac{h}{4} - \frac{o}{2} \qquad I_2 = \tfrac{c}{2} \qquad I_1 + I_2 = I$$

Before deriving the reaction and mixing rates, it is necessary to clarify the basis of the homogeneous combustion model:

- All species involved have the same diffusion coefficients and turbulent Prandtl numbers
- Viscosity and thermal conductivity are not functions of concentration, but only of temperature
- N_2 serves as an inert background fluid

The problem now is one of determining the rates of change of the species involved in the chemical reactions, or rather the *source terms* of the relevant transport equations. For turbulent flow[1], these equations all take the general form

$$\rho_g \frac{\partial \phi}{\partial t} + \nabla(\rho_g \vec{u}_g \phi) - \nabla\left(\Gamma_t \nabla \phi\right) = S_\phi \quad (3.42)$$

ρ_g: background fluid density $[kg/m^3]$

ϕ: dependent variable, ie. the quantity being transported

$\vec{u}_g$: fluid velocity $[m/s]$

Γ_t: effective (turbulent) diffusion coefficient $[kg/ms]$

S_ϕ: source term

In order to completely describe the system, it would be necessary to define a transport equation for the mass fractions of each of the hydrocarbon (fuel), oxygen, carbon monoxide, carbon dioxide, water and nitrogen concentrations, but by some manipulation, a *mixture fraction* ((Kær and Nielsen 1996), (CFDS 1994)), relating the fuel, oxygen and products, can be used to reduce the number of non-linear transport equations from 7 to a combination of 3 transport equations and 4 algebraic expressions, thereby reducing the computational effort considerably.

3.8.1 Gas phase source terms - EDC kinetic model

Homogeneous combustion can be thought of as occuring in two separate steps. First, the reactants must mix together from a macroscale right down to molecular levels.

[1]For laminar flow, the diffusion coefficient becomes the laminar, or molecular, viscosity, which usually is much lower than the turbulent diffusivity.

Then, once they have been brought together on a molecular level, a chemical reaction occurs, governed by a kinetic reaction rate.

One of the most general formulations of turbulent mixing is the Eddy Dissipation Concept (EDC) of Magnussen and Hjertager (1976). The EDC model formulates a mixing rate through the eddy cascade of turbulence, until the reactants have entered the smallest (Kolmogorov) eddy, whence the mixing is complete. The mixing rate is given as

$$S_{EDC} = -23.6 Re_t^{-0.25} \rho_g \frac{\varepsilon}{k} \min\left(m_F, \frac{m_{O_2}}{i_n f_o}\right) \tag{3.43}$$

Re_t: turbulent Reynolds number $[-]$:

$$Re_t = \frac{\rho_g k^2}{\mu_g \varepsilon} \tag{3.44}$$

k: turbulent kinetic energy $[m^2/s^2]$
ε: turbulent dissipation $[m^2/s^3]$
μ_g: molecular viscosity $[kg/ms]$
m_F: mass fraction of fuel (hydrocarbon) $[kg/kg\ fluid]$
m_{O_2}: mass fraction of oxygen $[kg/kg\ fluid]$
f_o: mass fraction of oxygen in oxidant $[kg/kg\ fluid]$
i: amount of oxidant needed for complete combustion of 1 kg fuel

$$1\ kg\ fuel + i\ kg\ oxidant \longrightarrow (1+i)\ kg\ products \tag{3.45}$$

$$i_1 = \frac{32}{M_F}\frac{I_1}{f_o} \quad i_2 = \tfrac{4}{7}\tfrac{1}{f_o} \quad i = i_1 + \frac{28c}{M_F} i_2 \tag{3.46}$$

n: 1 for the $C \longrightarrow CO$ reaction, 2 for the $CO \longrightarrow CO_2$ reaction
M_F: molecular mass of the fuel. $M_F = 12c + h + 16o$ $[kg/kmol]$

Equation 3.43 can be modified by the inclusion of a product term, such that the min() term of the fuel and CO consumption source terms become, respectively:

$$\min\left(m_F, \frac{m_{O_2}}{i_1 f_o}, \frac{m_{H_2O}}{M_{H_2O}}\right) \qquad \min\left(m_{CO}, \frac{m_{O_2}}{i_2 f_o}, \frac{28}{44} m_{CO_2}\right) \tag{3.47}$$

M_{H_2O}: molecular mass of water $[kg/kmol]$

Including the product term in either source term serves as a reaction maintainer, as it indicates that where products exist, a reaction must have occurred, and therefore there is a sufficiently high temperature for the reaction to progress.

3.8.2 Homogeneous reaction kinetics

Once the reactants have been mixed at a molecular level, chemical kinetics take over the reaction speed. This is normally expressed using an Arrhenius equation. For the

two reactions considered these expressions are:

$$\frac{d[fuel]}{dt} = A \exp\left(-\frac{E}{RT}\right)[fuel]^{n_a}[O_2]^{n_b} \quad [kg/s] \tag{3.48}$$

$$\frac{d[CO]}{dt} = A \exp\left(-\frac{E}{RT}\right)[CO]^{n_a}[O_2]^{n_b}[H_2O]^{n_c} \quad [kg/s] \tag{3.49}$$

A: Arrhenius constant

E: activation energy $[kJ/kmol]$

n_a, n_b, n_c: reaction constants $[-]$

3.8.3 Overall homogeneous reaction rate

The overall reaction rate is governed by the slowest of the mixing and kinetic rates. Different investigators report different methods of combining these rates, but the method used in the current consists of a parallel combination of the rates:

$$S_{hom} = \left(\frac{1}{S_{EDC}} + \frac{1}{S_k}\right)^{-1} \tag{3.50}$$

3.9 Summary

This chapter concerns the modelling of the combustion reactions, homogeneous as well as heterogeneous. Different solid combustion models are discussed, emphasizing the applicability of each model to either coal or biomass combustion. Specifically, only the reactivity index model (section 3.2.3) is suited for straw combustion, whereas the mixed control model (section 3.2.1) as well as Gibb's model (section 3.2.2), with the modifications described, are well suited for coal combustion. The reason for the differences in applicability to fuels is primarily based upon the availability of kinetic data.

The homogeneous reactions are modelled using the Eddy Dissipation Concept (section 3.8.1) coupled with a kinetic rate, whichever solid fuel is prescribed. The model is a two-step model, with an intermediate production and subsequent consumption of CO.

Chapter 4

Terminal velocity calculations

Verification of a non-spherical particle model is hampered by the abscence of suitable data. One of the few parameters, on which experimental data exists also for non-spherical particles, is terminal velocities. Although the terminal velocity is an integral quantity, which includes directional information, comparison between measurements and numerical prediction gives a measure of the "average" aerodynamic quality of the model. Furthermore, as terminal velocities are normally determined in stagnant surroundings, it is a pure form of the equation of motion, where possible sources of error due to the inclusion of for example turbulent dispersion, are eliminated.

One of the sources of information is the data of Crowe (1997) shown in table 4.1. Fused quartz particles with aspect ratios of unity were dropped in mineral oil with a density of 825 $[kg/m^3]$ and a viscosity of 6.16 $[Pas]$.

	Diameter $[mm]$	**Density** $[kg/m^3]$	**Terminal velocity** $[m/s]$
Cylinders	6.0	2250	0.382
	9.0	2250	0.456
Spheres	6.0	2450	0.405
	9.0	2450	0.55

Table 4.1: Terminal velocities of isometric particles falling in Penrecos Drakeol mineral oil reported by Crowe (1997).

Other sources of data are reviewed by Haider and Levenspiel (1989), and together, the two sources cover blunt cylinders, spheres, discs and regular shapes with no one dimension much larger than the other, i.e. an aspect ratio close to unity.

4.1 Determination of terminal velocity

The terminal velocity of falling particles can be expressed semi-analytically as well as empirically.

Assuming a stationary, vorticity-free flow, a free falling spherical particle will experience a drag and buoyancy force, retarding the motion, and a gravity force acting in the opposite direction. At some point in time, the forces acting upon the particle will enter a state of equilibrium, cancelling each other out:

$$\vec{F}_D + \vec{F}_{buoy} + \vec{F}_g = 0 \tag{4.1}$$

Assuming Stokes regime and introducing the Archimedes number, equation 4.1 can be rewritten as (Brauer 1971)

$$\frac{|\vec{u}_g - \vec{u}_p| d_p}{\nu_g} = \frac{Ar}{18} \tag{4.2}$$

Ar: the Archimedes number, given by

$$Ar = \frac{d_p^3 \vec{g}}{\nu_g^2} \left(\frac{\rho_p}{\rho_g} - 1 \right) \tag{4.3}$$

For particle Reynolds numbers greater than approximately one and using equation 2.23, equation 4.2 becomes:

$$18Re_p + 3Re_p^{1.5} + 0.3Re_p^2 = |Ar| \tag{4.4}$$

Equation 4.4 is based only on spheres, and extending it to superellipsoids is possible by including the shape correlation f_{sel} (equation 2.28). However, as there is no incidence angle dependency, results based on such an extension become meaningless.

Haider and Levenspiel (1989) give another approach of calculating the terminal velocity for non-spherical particles, based on empirical correlations. Two dimensionless parameters are introduced, a diameter d_* and a terminal velocity u_*:

$$d_* = d_p \left(\frac{|\vec{g}| \rho_g (\rho_p - \rho_g)}{\mu_g^2} \right)^{1/3} \tag{4.5}$$

$$u_* = u_t \left(\frac{\rho_g^2}{|\vec{g}| \mu_g (\rho_p - \rho_g)} \right)^{1/3} \tag{4.6}$$

Based on several datasets, Haider and Levenspiel (1989) propose the following numerical correlation for equation 4.6, derived from the formulation of the drag coefficient given by equation A.9:

$$u_* = \left(\frac{18}{d_*^2} + \frac{3K_1}{4d_*^{0.5}} \right)^{-1} \tag{4.7}$$

$K_1 = 3.1131 - 2.3252\phi$

ϕ: particle sphericity (equation A.8)

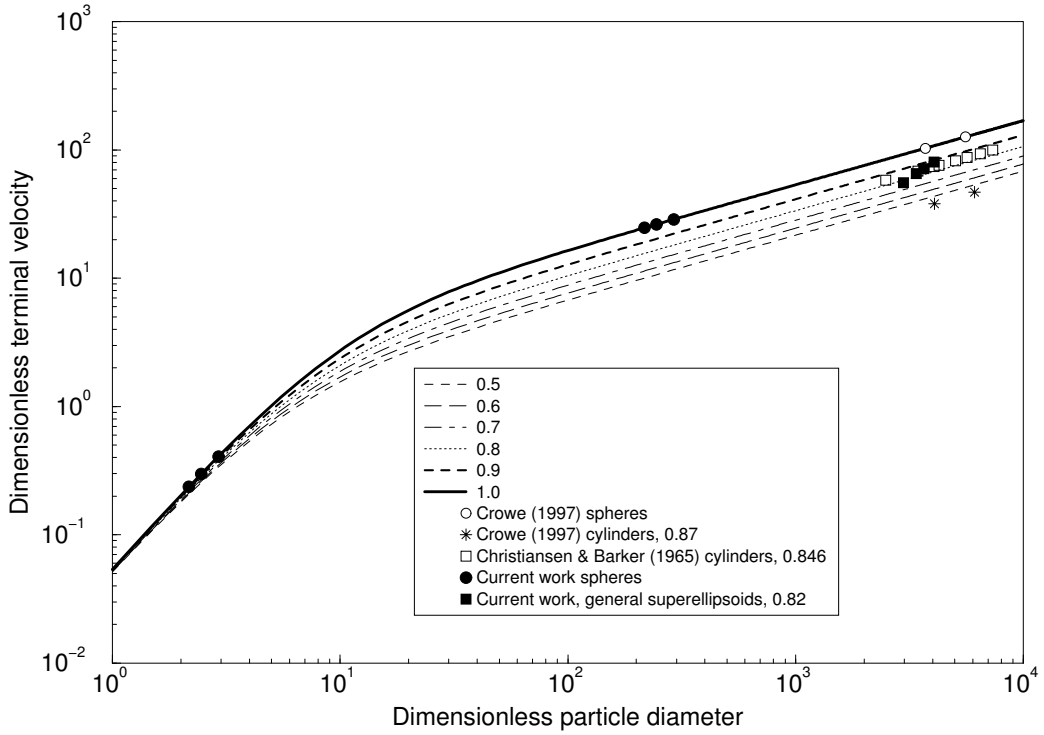

Figure 4.1: Terminal velocities (u_*) of isometric particles of sphericities in the range [0.5;1.0] as functions of d_* based on equation 4.7. Measured values by Crowe (1997) (table 4.1) and Christiansen & Barker (1965) and predicted values for spheres and general superellipsoids based on the current model are also shown. Superellipsoid parameters: $n = 75,\ \beta = 1,\ \phi = 0.82$.

Figure 4.1 shows very good agreement between the findings of the different experimental works and the numerical results of the current work, as well as the predictions of equation 4.7. A notable exception to this are the two cylinders of Crowe (1997), which fall well below the iso- sphericity line of 0.5, where they should have been in the same neighbourhood as the results reported by Christiansen and Barker (1965). A possible cause of this is the addition of a small amount (less than 5%) of Stottdard solvent to align the indices of refraction of the oil and the glass wall (Crowe 1997). This will have reduced the viscosity of the oil, although this is unlikely to have occured to the extent of changing the reported terminal velocities indicated in figure 4.1.

Due to its formulation, the current model is unable to predict the motion of particles with aspect ratios less than one. However, as shown in figure 4.2, this covers a wide range of sphericities. Considering the case of a cylinder with $\beta = 1.0$ and $n = 100.0$,

manipulation of the expression for the sphericity gives this quantity as a function of β:

$$\phi = \frac{2\left(\frac{3}{2}\beta\right)^{2/3}}{1+2\beta} \tag{4.8}$$

This analysis can only be completed analytically for cylinders, as the surface area as well as the volume of general superellipsoids belongs to the class of elliptic equations, which cannot be solved analytically (see Appendix B.1). Equation 4.8 is plotted in figure 4.2.

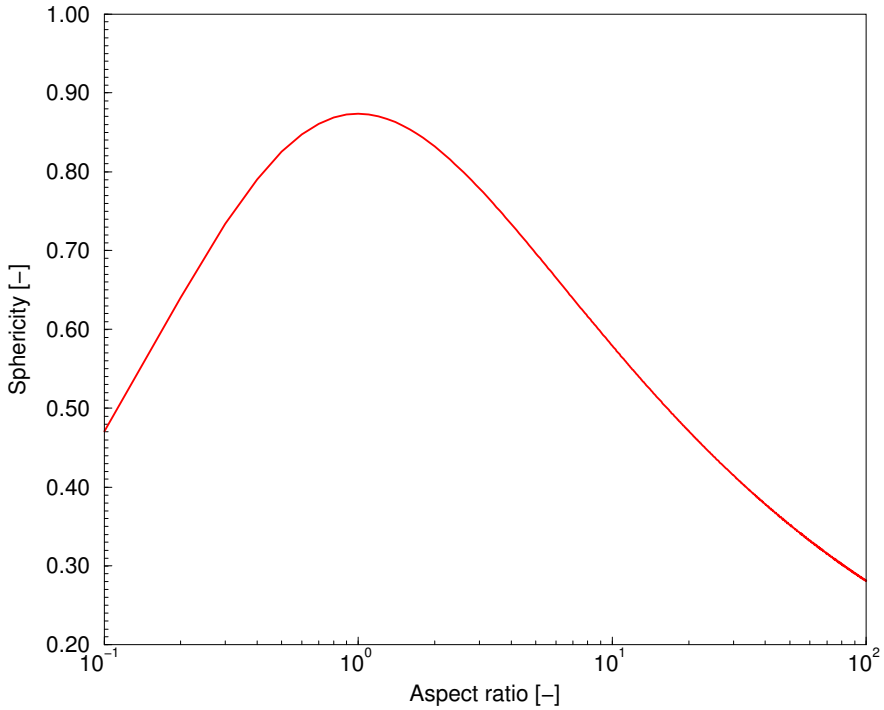

Figure 4.2: Sphericity (ϕ) as a function of aspect ratio (β) for cylinders using equation 4.8.

Not surprisingly, equation 4.8 shows a sphericity peak at $\beta = 1$, and drops for both disks and long cylinders. As a shape describing parameter, the sphericity is restricted to the class of isometric particles, which find their sphericities within the "peak" area of figure 4.2.

4.2 Stability of orientation

Non-spherical particles moving relative to a surrounding fluid will tend to exhibit a tumbling, or oscillatory motion. For particles moving in a stagnant, vorticity- free fluid, this motion will become stationary in time, and, as shown by Marchildon et al. (1964) for cylinders, becomes one of simple harmonic motion as indicated in figure 4.3.

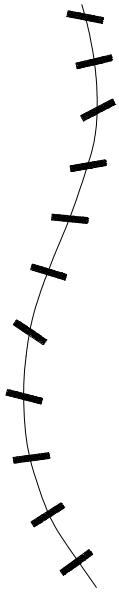

Figure 4.3: Schematic of the tumbling motion of non-spherical particles falling through a stagnant fluid. From Brauer (1971).

When the incidence angle exceeds ninety degrees, the centre of pressure moves from one end of the particle to the other. When this happens, the aerodynamic forces change direction, and the rotation of the particle slows down, and ultimately changes direction, as illustrated in figure 4.4. This repeats itself, and the oscillatory motion is established.

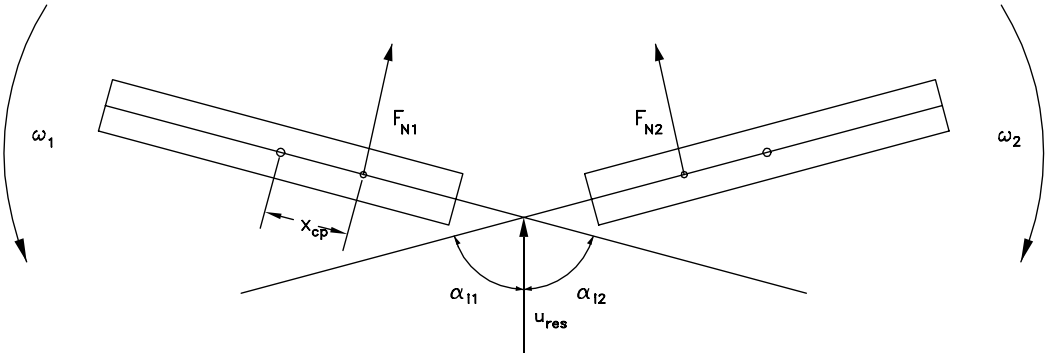

Figure 4.4: Schematic of the forces causing tumbling motion of non- spherical particles, as the angle of incidence exceeds ninety degrees.

However, for industrial systems, the stable condition is unlikely to be obtained by the particle. Such systems are often characterized by high turbulence, swirling flows, joining or division of multiple streams etc, leaving ideal conditions a hypothetical situation.

The analysis of Marchildon et al. (1964) is based on the ratio of front pressure build up and rear pressure deficit of a disk at ninety degrees incidence. Assuming the same

ratio of 44:56 holds for cylinders, the torque acting on a cylinder moving through a stagnant fluid is:

$$\vec{T} = 0.44\vec{F}_D x_{cp} \tag{4.9}$$

$\vec{F}_D$: drag force, defined in the conventional manner $[N]$

x_{cp}: location of centre of pressure respective to the plate centre, given by Marchildon et al. (1964) as:

$$x_{cp} = \frac{0.75\sin(90^\circ - \alpha_i)}{4 + \pi\cos(90^\circ - \alpha_i)} L \tag{4.10}$$

L: cylinder length ($2b$ using the superellipsoid formulation) $[m]$

Performing an angular force balance and keeping the drag force and force ratio constant, assuming the latter to be the same for a cylinder as for a disk, the period of oscillation of a cylinder becomes

$$P = 40.9\left(\frac{I_p}{\rho_p D L^2 u_t^2}\right)^{1/2} \tag{4.11}$$

I_p: moment of inertia $[kgm^2]$

u_t: terminal velocity $[m/s]$

D: cylinder diameter ($2a$ using the superellipsoid formulation) $[m]$

The assumption of constant drag force and force ratio in equation 4.11 as well as a simplification of equation 4.10, introducing an error of the order of 10% in the incidence angle interval $[0; 90]^\circ$, obviously equips equation 4.11 with some uncertainty. The correct expression for the drag force would entail the derivation of a mean value of the drag force in the interval of the steady state oscillation:

$$F_{\bar{D}} = \frac{1}{2}\rho_g \frac{u_r|u_r|}{\Delta\alpha}\int_{\alpha_-}^{\alpha_+} A_p(\alpha) C_D(\alpha) d\alpha \tag{4.12}$$

α_-, α_+: steady state oscillation bounding incidence angles $[rad]$

u_r: relative velocity between particle and fluid $[m/s]$

A_p: projected area $[m^2]$

As the bounding incidence angles are unknown, equation 4.12 cannot be solved, and the simplification of assuming constant drag becomes a necessary one.

Regardless of the uncertainties and shortcomings discussed above, valuable information on the dominant parameters regarding particle oscillation and equillibrium can be extracted from equation 4.11.

Assuming $\frac{D^2}{4} \ll \frac{L^2}{3}$, i.e. long cylinders, and assuming constant filling of the wake, equation 4.11 can be expressed using Strouhals number:

$$Sr_{cyl} = f\frac{(DL)^{1/2}}{u_t} \approx \frac{1}{10.5}\left(\frac{\rho_g}{\rho_p}\right)^{1/2} \tag{4.13}$$

f: oscillation frequency $[Hz]$

Thus, it follows from equation 4.13, that a dominant parameter is the density ratio between the fluid and the particle.

4.3 Summary

Different numerical correlations for the terminal velocity of particles falling in stagnant fluids have been presented, as well as a simple equation for the oscillatory period of falling cylinders.

Comparison of the results from the current work with these numerical correlations shows very good agreement, and indicates the soundness of the model of motion as formulated here.

.

Chapter 5

Single particle combustion

In order to model an entire system of combusting particles, suitable engineering models for each sub-reaction, which capture the global properties and characteristics of the system, have to be employed. A number of such models are available, the vast majority of these were designed for bituminous coals, and also, perhaps more importantly in the context of this work, for spheres.

Particle combustion models can be divided two parts: one part which describes the change of the particle dimensions, and a second part which describe the mechanisms controlling the rate of combustion. Predominant among the former are the progressive conversion and unreacted core or shrinking sphere models (cf. section 3.5), which describe the relationship between the change of size and the mass reduction due to combustion.

A number of models describing the manner in which the reaction occurs have been put forward. This work deals only with three of these, the mixed control and Gibb's model (Gibb 1985) for coal, and the reactivity index model (Sørensen 1996) for coal as well as biomass. Common for all is that they combine a kinetic and a diffusion rate, and therefore are limited by the slowest. For the common temperature regimes and oxygen fractions in furnaces, the diffusion rate will normally be rate controlling, and thus the importance of accurately modelling the heterogeneous combustion kinetics fades. Considering straw, with only approximately 16% char by mass, this becomes even more obvious.

The models used in the current chapter are described in detail in Chapter 3.

5.1 Burnout profiles

In order to investigate the burnout profiles predicted by the heterogeneous combustion models, these are applied, under idealised conditions, to particles representative of the fuels of interest for the current work, coal and straw, using data from tables 1.1, 1.2, 1.3 and Rosendahl (1995). Full details of the particle parameters are given in the table below.

	Coal	Straw
Char mass fraction $[kg/kg]$	0.463	0.161
Volatiles mass fraction $[kg/kg]$	0.36	0.707
Water mass fraction $[kg/kg]$	0.115	0.087
Ash mass fraction $[kg/kg]$	0.096	0.045
Particle density $[kg/m^3]$	1250.0	150.0
Particle diameter (2a) $[\mu m]$	150.0	1500.0
Aspect ratio $[-]$	1.0	1.0
Initial particle temperature $[K]$	350.0	350.0
Ambient gas temperatures $[K]$	1408,1503,1673	1408,1503,1673
Oxygen volume fraction $[m^3/m^3]$	0.025, 0.04, 0.08	0.025, 0.04 .08
Activation energy, eq. 3.5 $[kJ/kg]$	1.248×10^3	0.936×10^{3a}
Pre-exp. factor, eq. 3.5 $[kg/m^2Pas]$	0.86	0.86
Void fraction, eq. 3.12 $[-]$	0.5	0.5
Pore diameter, eq. 3.14 $[nm]$	5.0	5.0
Activation temperature, eq. 3.19 $[K]$	16040.0	14540.0
Reaction order, eq. 3.19 $[-]$	0.77	0.69

[a] Corresponding to 75% of the activation energy for Columbian Cerrejon coal

Table 5.1: Initial parameters for particles used in heterogeneous combustion model comparison.

Pyrolysis and evaporation is described using the first order model given by equation 3.1, with parameters for straw set to 75% of those for Columbian Cerrejon coal due to the looser bindings of the volatile gases in straw. The choice of reducing the activation energy by 75% is based on a best guess and trial and error, as no data is available for straw in terms of kinetic reaction rates. Stefan flow is not included. The Nusselt number relation of equation 3.29 is used for the convective heating rate, and a full implementation of the temperature dependent product composition is used for all three heterogeneous combustion models.

For both types of fuel at all temperatures, similar traits can be discerned. In all cases, the mixed control model predicts the longest burnout times, and Gibb's model the shortest. This is due to the different formulation of the diffusion rate of Gibb's model compared to the mixed control and reactivity index models, which share the same diffusion formulation, and, as shown on figure 5.4, the diffusion rate becomes limiting for temperatures above approximately 1400K. Regarding the burnout profiles predicted using Gibb's model, these differ from those predicted by the other two models

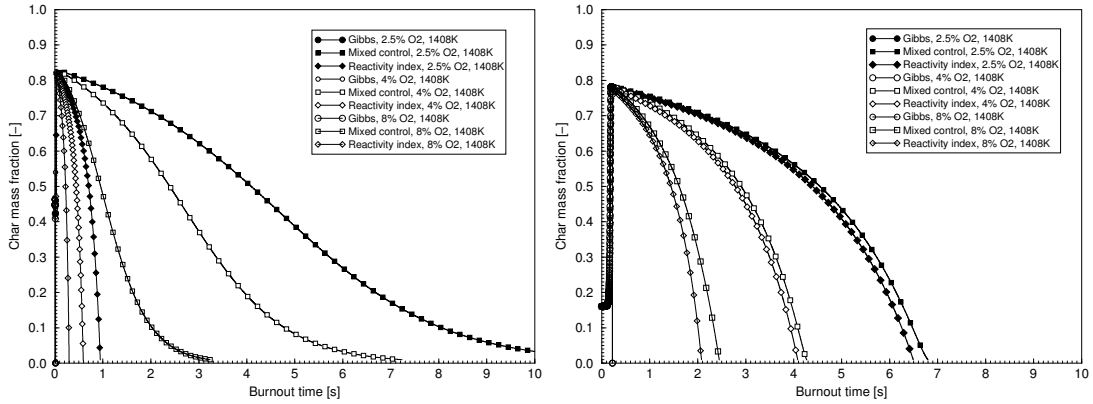

Figure 5.1: Idealised char burnout profiles of a coal particle (left) and a straw particle (right) using the mixed control model, Gibbs model and the reactivity index model at different oxygen concentrations. Ambient gas temperature is 1408K.

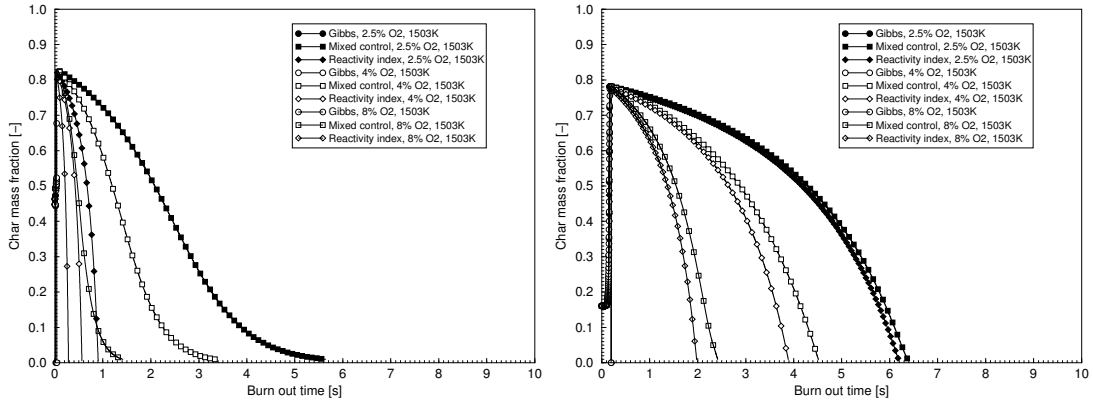

Figure 5.2: Idealised char burnout profiles of a coal particle (left) and a straw particle (right) using the mixed control model, Gibbs model and the reactivity index model at different oxygen concentrations. Ambient gas temperature is 1503K.

by such a significant amount, that they should be treated with caution as being possibly erroneous.

A distinguishing feature of the coal burnout profile is the assymptotic behaviour near the burnout limit of the mixed control model, which is only hinted at for the straw particles. This is caused by using the active surface correction (equation 3.34), which gradually reduces the available surface area for reaction and reduces the kinetic rate to such an extent, that it becomes rate limiting. Combined with the relatively smaller amount of ash and greater surface area of the straw particle, the active surface correction has much less effect for the burnout profile of these particles.

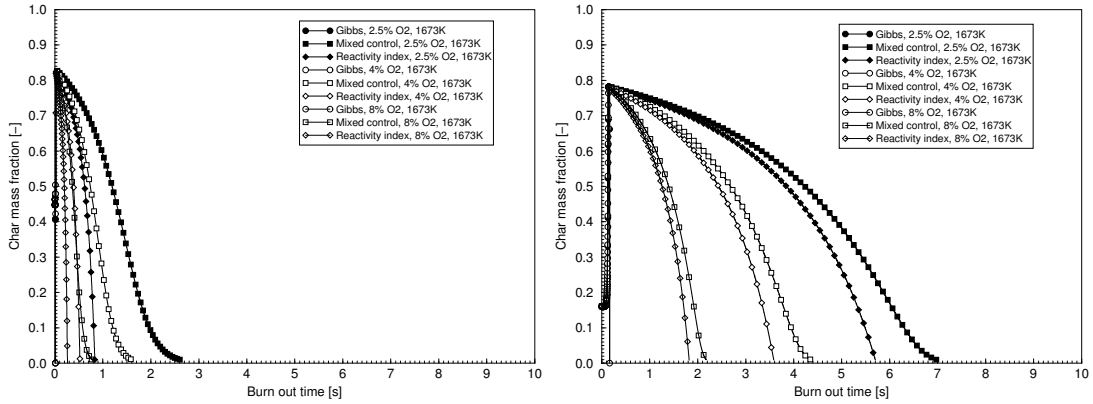

Figure 5.3: Idealised char burnout profiles of a coal particle (left) and a straw particle (right) using the mixed control model, Gibbs model and the reactivity index model at different oxygen concentrations. Ambient gas temperature is 1673K.

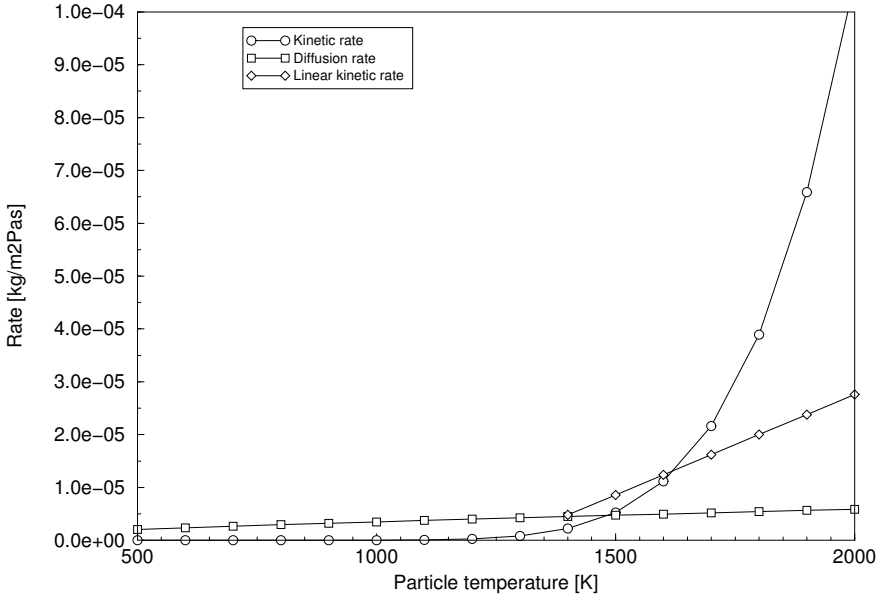

Figure 5.4: Heterogeneous reaction rates, using parameters for Columbian Cerrejon Coal, showing the temperature range where diffusion and kinetics control the reaction rate. Legend: ○: Kinetic rate, equation 3.5. □: Diffusion rate, equation 3.7. ◇: Linear kinetic rate, equation 3.6.

For straw, burnout times have been measured and video recorded by Stoholm and Kirkegaard (1992). Straw tubes of masses in the range 18-36mg were suspended on a platinum wire, and exposed to ambient conditions of 1408-1673K and 3.9-7.2% oxygen. An example of such a burnout process is shown on figure 5.6, where a 27mg straw is exposed to 1673K and 4.0% oxygen. Burnout in this case was achieved in 4.0 seconds

(symbolised in figure 5.5 by ▷), which is very much higher than for normal coal dust burnout times, but which corresponds well to the predictions of all the heterogeneous combustion models applied to straw. This is due to the relatively high gas temperature, which is above the temperature at which the diffusion rate becomes rate limiting. The data of the other combustion tests are shown in figure 5.5.

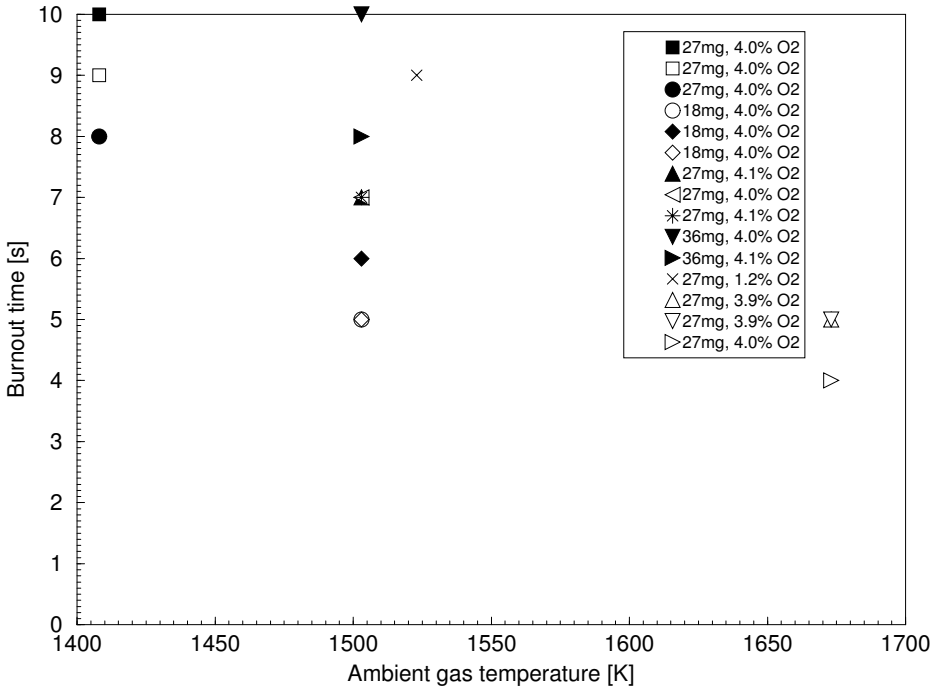

Figure 5.5: Burnout times of straw tubes at different ambient conditions.

Comparing the burnout time predictions of the heterogeneous combustion models to the experimental data for straw, Gibb's model is readily discarded as discussed previously. For the mixed control and reactivity index models in the formulations of this work, very good agreement is found with the experimental data. For example, the burnout time of a straw particle at 1673K and 4% oxygen is predicted to within 10% of the measured burnout time, using both models. This indicates that using conventional models for the burnout of straw particles, with either kinetic data directly for straw or appropriately modified kinetic data for coal, yields good results, provided that the temperatures are so high, that diffusion becomes rate limiting for the majority of the particle combustion period. At the same time, the transformation between actual straw shape and a sphere with the same surface area is also shown not to influence the model predictions negatively. Until specific experimental data on straw combustion becomes available to a degree where models aimed directly at straw can be formulated, or parameters derived specifically from straw experiments can be used, this combination seems a feasible engineering solution.

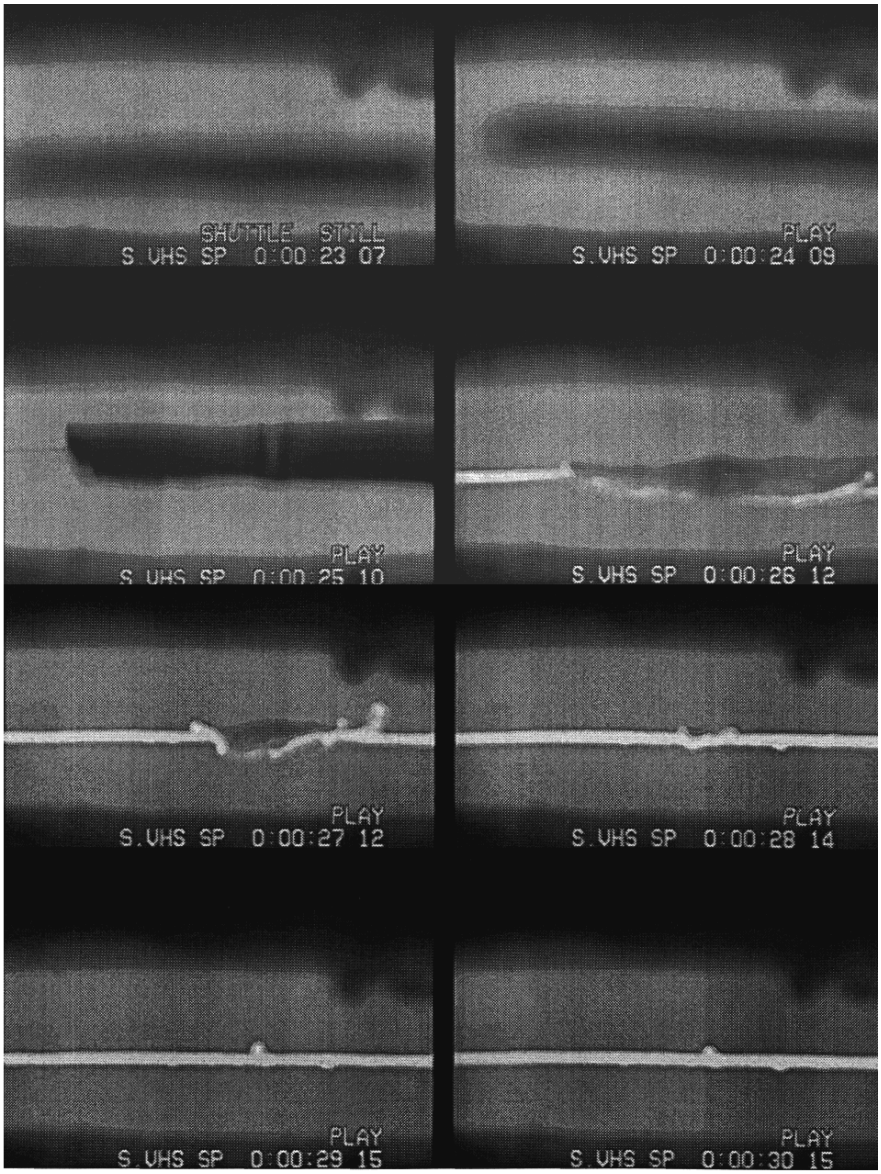

Figure 5.6: Video recording of a combusting straw tube, suspended on a platinum wire. Ambient gas temperature 1673K, initial mass 27 mg. From Stoholm and Kirkegaard (1992).

For the burnout profiles shown in figures 5.1-5.3, and for the calculations on the MKS1 burner (Chapter 8), the kinetic parameters used for the straw are set to 75% of those for Columbian Cerrejon coal, and the straw particles undergo the area transformation described above and in Section 3.2.

It is clear, however, that the burnout times shown in figures 5.1- 5.3 are somewhat longer than is normally encountered in furnaces. However, it is unlikely that fuel particles entering the flamezone of a furnace burner experience as low temperatures

and oxygen concentrations as in the preceding discussion, and therefore these particles will burn out quicker than shown here.

5.2 Theoretical burnout time

Based on idealised and constant external parameters, Levenspiel (1972) expresses a theoretical burnout time τ_b, for any particles based on the mixed control model as:

$$\tau_b = \frac{\rho_{p0} R T_m}{96 \phi D p_{O_2}} d_{p0}^2 + \frac{\rho_{p0}}{2 K_k p_{O_2}} d_{p0} \tag{5.1}$$

As can be seen, equation 5.1 contains the terms K_k, T_m and D, all of which are strongly temperature dependent, and therefore change through the particle lifetime. Further, no information as to the amount of char is included. Thus, equation 5.1 only gives meaningful results when sensible mean values are used for these terms.

A full integration of the processes over a particles lifetime can only be done by assuming the reaction to be either diffusion controlled or chemical kinetics controlled, and even then, introducing a number of assumptions and simplifications. Examples of this are given in Appendix F for the mixed control model and reactivity index model. As can be seen, the resulting equations involve the burnout time in very complex expressions, and it cannot easily be extracted.

Chapter 6

Testcase: AAU/DTU isothermal test rig

The AAU/DTU isothermal test rig has been used for several of the initial test runs of the non-spherical tracking code. Designed at Aalborg University by Christian Brix Jacobsen for a series of Laser Doppler Anemometry measurements for Large Eddy Simulation (see Jacobsen (1997)), it is now located at the Technical University of Denmark in Lyngby.

The tubular test rig is shown in figures 6.1 and 6.2. It consists of an annular inlet section preceeded by a vane swirler, such that the centre inlet remains unswirled, but the annular secondary inlet is swirled. After the inlet, a quarl expands the flow before entering the main section of the rig. At the end of the channel section an exit section is fitted.

6.1 Inlet conditions

The inlet conditions are prescribed from the LDA measurements performed on the rig in single-phase flow (Jacobsen 1997). Only a single swirl setting has been used for the gas-particle simulations, and the axial and tangential velocities, consisting of a central axial flow core, surround by swirling annular air, are shown in figures 6.3 - 6.4.

6.1.1 Inlet conditions for small particles

Inlet parameters for the four different particle simulations are shown in table 6.1. The simulations consist of one small sphere simulation, and a series of three simulations of spheres, ellipsoids and cylinders, which are defined in such a way that they are equivolumetric. This is done to provide a basis for comparison of the trajectories followed by the different shapes, where the differences can be ascribed to aerodynamical and

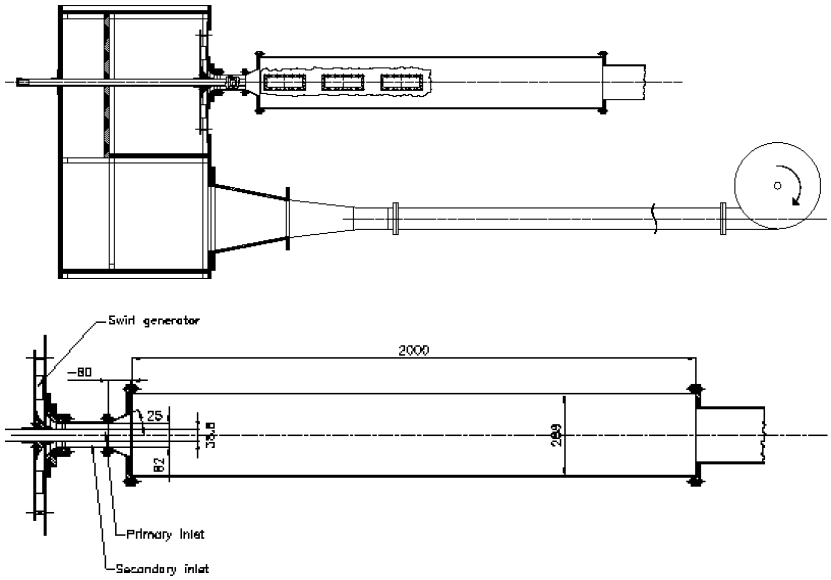

Figure 6.1: The AAU/DTU isothermal test rig. Top view: entire rig configuration. Bottom: dimensions of measurement section in millimetres.

hence shape effects.

	Spheres 1	**Spheres 2**	**Ellipsoids**	**Cylinders**
Inlet loading ratio $[kg\ particles/kg\ air]$	0.10	0.10	0.10	0.10
Number of trajectories	90	90	90	90
Inlet location	Centre tube	Centre tube	Centre tube	Centre tube
Inlet axial velocity $[m/s]$	16.00	16.00	16.00	16.00
Inlet angular velocity $[rad/s]$	[0.0,0.0,0.0]	[0.0,0.0,0.0]	[0.0,0.0,0.0]	[0.0,0.0,0.0]
Direction angles of major particle axis $[rad]$	$[0, \frac{\pi}{2}, \frac{\pi}{2}]$	$[0, \frac{\pi}{2}, \frac{\pi}{2}]$	$[0, \frac{\pi}{2}, \frac{\pi}{2}]$	$[0, \frac{\pi}{2}, \frac{\pi}{2}]$
Volume $[\times 10^{-15}]$	0.524	0.979	0.978	0.978
Minor particle axis $[\mu m]$	5.0	12.32	5.72	2.5
Projected area[a] $[\times 10^{-10}]$	0.785	1.191	2.565	2.490
Axis aspect ratio $[-]$	1.0	1.0	10.0	10.0
Superelliptic exponent $[-]$	2.0	2.0	2.0	50.0
Particle density $[kg/m^3]$	1000.0	1000.0	1000.0	1000.0

[a] At 90° incidence

Table 6.1: Inlet conditions for gas-particle simulations in AAU/DTU isothermal test rig. Small particles.

6.1.2 Inlet conditions for large particles

The inlet conditions of the large particles, shown in table 6.2, are configured subject to the same considerations as discussed above for the small particles.

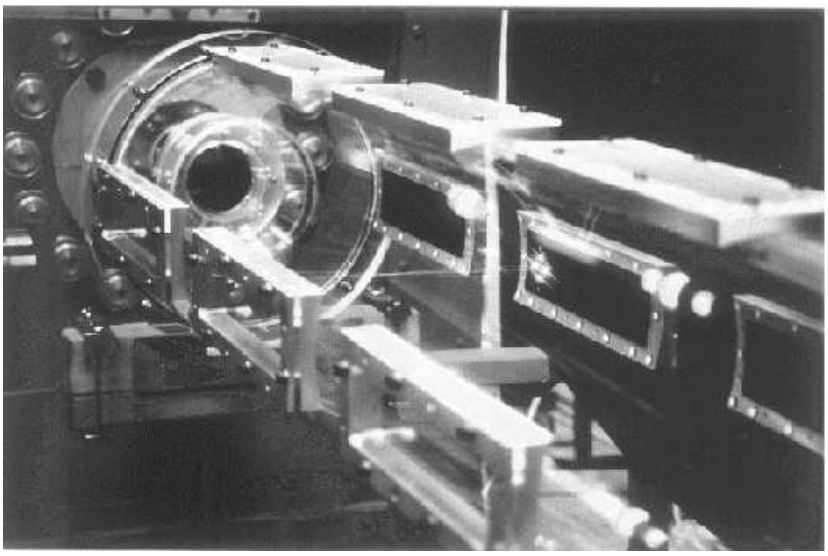

Figure 6.2: Picture of the isothermal test rig during the LDA measurements. The four dots on the far side are the laser beams reflecting off the surface. Photo: Christian Brix Jacobsen.

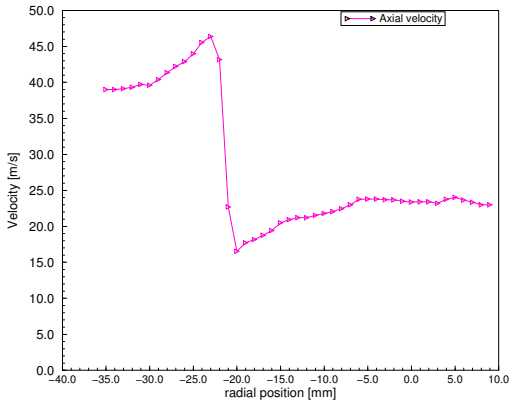

Figure 6.3: Measured inlet velocities at radial positions.

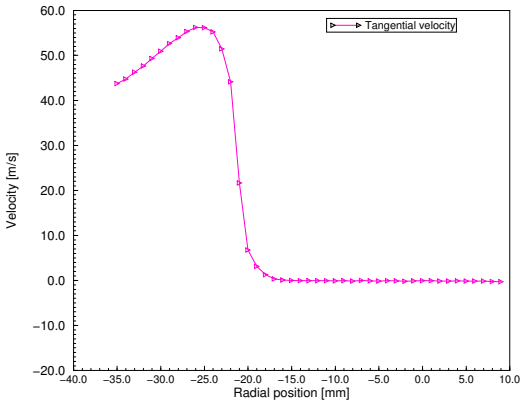

Figure 6.4: Measured tangential inlet velocities at radial positions.

6.2 Computational configuration

6.2.1 Mesh and physical models

The mesh used for the calculations is a structured butterfly mesh (see figure 6.5) with a square central block, consisting of 15 blocks and approximately 36,000 cells. This type of mesh is used to avoid excessively skew cells with cell angles approaching 180

	Spheres	**Ellipsoids**	**Cylinders**
Inlet loading ratio $[kg\ particles/kg\ air]$	0.10	0.10	0.10
Number of trajectories	100	100	100
Inlet location	Centre tube	Centre tube	Centre tube
Inlet axial velocity $[m/s]$	16.00	16.00	16.00
Inlet angular velocity $[rad/s]$	[0.0,0.0,0.0]	[0.0,0.0,0.0]	[0.0,0.0,0.0]
Direction angles of major particle axis $[rad]$	$[0, \frac{\pi}{2}, \frac{\pi}{2}]$	$[0, \frac{\pi}{2}, \frac{\pi}{2}]$	$[0, \frac{\pi}{2}, \frac{\pi}{2}]$
Volume $[m^3]$	3.35×10^{-11}	1.34×10^{-10}	8.04×10^{-10}
Minor particle axis $[\mu m]$	400.0	400.0	400.0
Projected area[a] $[m^2]$	5.03×10^{-7}	1.01×10^{-6}	1.28×10^{-6}
Axis aspect ratio $[-]$	1.0	10.0	10.0
Superelliptic exponent $[-]$	2.0	2.0	100.0
Particle density $[kg/m^3]$	1000.0	1000.0	1000.0

[a] At right angles of incidence

Table 6.2: Inlet conditions for gas-particle simulations in AAU/DTU isothermal test rig. Large particles.

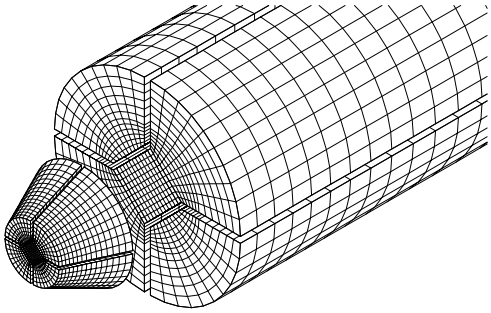

Figure 6.5: Detail of the quarl section of the butterfly mesh used for the calculations.

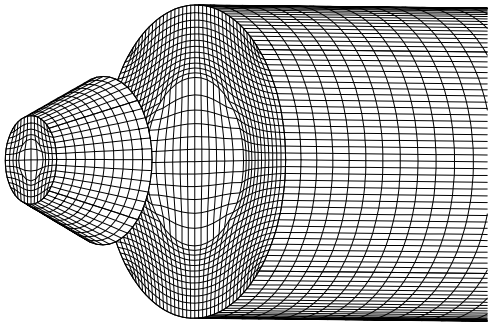

Figure 6.6: Detail of the quarl section of the standard mesh not used for the calculations.

degrees, as is the case with the standard three-block mesh shown in figure 6.6.

Turbulence is included using the $k - \varepsilon$ closure, with standard parameters as defined in CFDS (1994).

In the formulation of the particle equations of motion (equations 2.6 and 2.2-2.4), aerodynamic drag, profile lift and flow field vorticity are included. Turbulent dispersion is included using the eddy lifetime model (section 2.5.1).

The two-phase flow is not coupled, as only the trajectories are of interest in the current work.

6.3 CFD results

As shown in figures 6.7-6.9, the $k - \varepsilon$ turbulence closure provides a swirl profile of reasonable quality in the forward part of the furnace, although the swirl dies out rela-

tively close to the quarl, with subsequent smearing of the axial velocity profiles. This is not found in the measurements, as the high level of swirl maintains not only a long recirculation zone, but also steep radial gradients of the axial velocity.

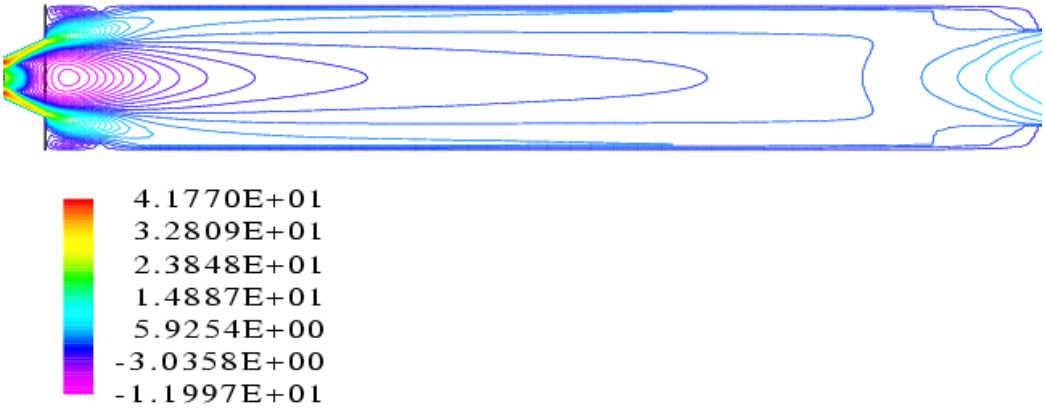

Figure 6.7: Axial velocity contours $[m/s]$in the AAU/DTU test rig.

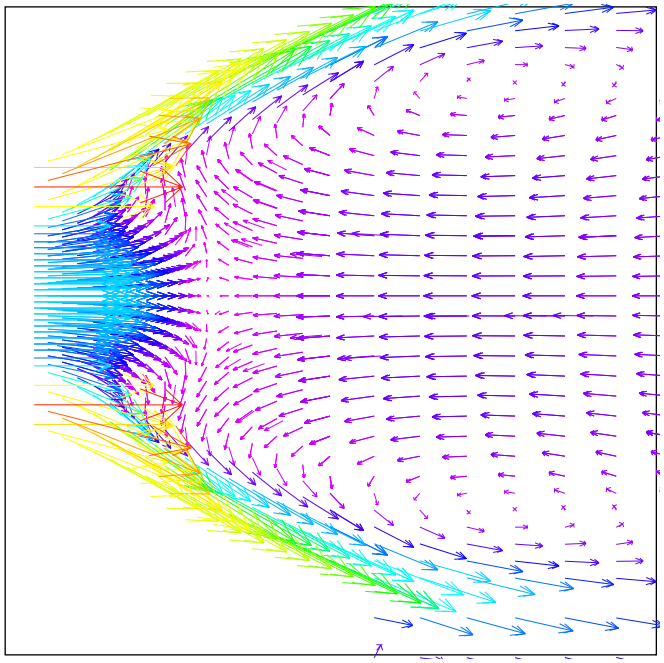

Figure 6.8: Velocity vectors in the near-burner zone.

6.4 LDA measurements

Extensive comparisons have been made between calculations and LDA measurements. For the purpose of this work, only figure 6.9 is included as documentation. For further details, please refer to Jacobsen (1997).

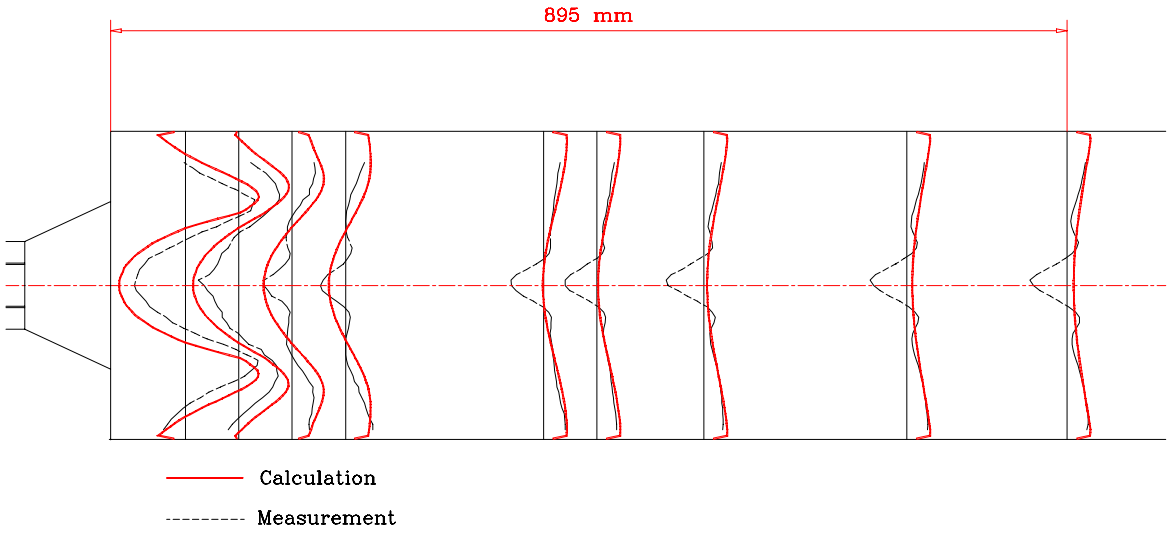

Figure 6.9: Measured and predicted velocity profiles in the forward part of the tubular chamber.

The flow field is not influenced by the presence of the particles, as no phase coupling has been performed for these calculations.

6.5 Particle trajectories

6.5.1 Small particles

The predicted particle trajectories in the AAU/DTU isothermal test rig are shown in figure 6.11.

The small spheres simulation is performed to gain confidence in the prediction of the trajectories of small particles in a swirling flow configuration. As expected, the resulting trajectories show a high degree of capture of particles in the central recirculation zone (figure 6.10).

As shown in figure 6.10, the two non-isotropic particles (ellipsoids and cylinders) show a much greater degree of dispersion compared to spheres. These, on the other hand,

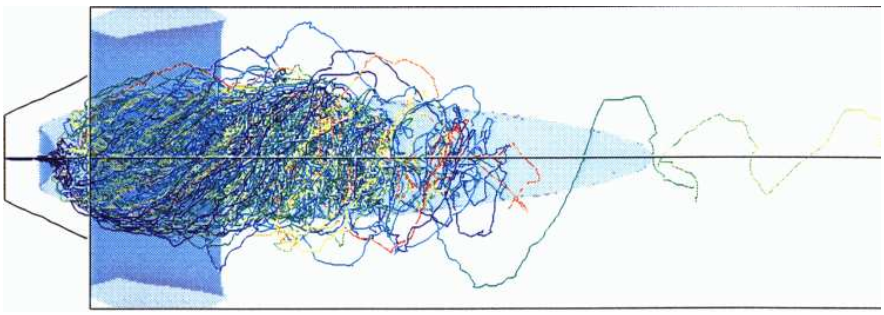

Figure 6.10: Small spheres (Spheres 1, table 6.1) in the AAU/DTU test rig. The shaded areas indicate the location of recirculation zones.

seem to be captured by the central recirculation zone at a greater rate than cylinders and ellipsoids, which is of importance in burner applications.

The differences in trajectories between the spheres and the non-isotropic particles are also very clear in the aerodynamic response times of the particles shown in figure 2.4. As the non-isotropic particles continuously change their orientation relative to the direction of the flow, the projected area as well as drag coefficient change rapidly, and for certain orientations, the particles have very large response times, causing them to diverge from the direction of the flow, leading to the high degree of dispersion shown in the trajectories.

6.5.2 Large particles

A primary characteristic of all three types of large particles is, that their aerodynamic response time is large enough for them to respond mainly to the mean flow, making visual comparison between the trajectories very valuable, as can be seen in figure 6.12. The spheres follow the flow, performing very regular traverses of the circumference of the furnace, in accordance with the flow. For the ellipsoids and cylinders, however, the pattern is much more erratic, and the particles disperse quickly, breaking away from the flow streamlines already in the early part of the quarl.

This erratic pattern is due to the misalignment of the resulting force acting on the particles and the direction of the flow, combined with the tumbling motion of the particles.

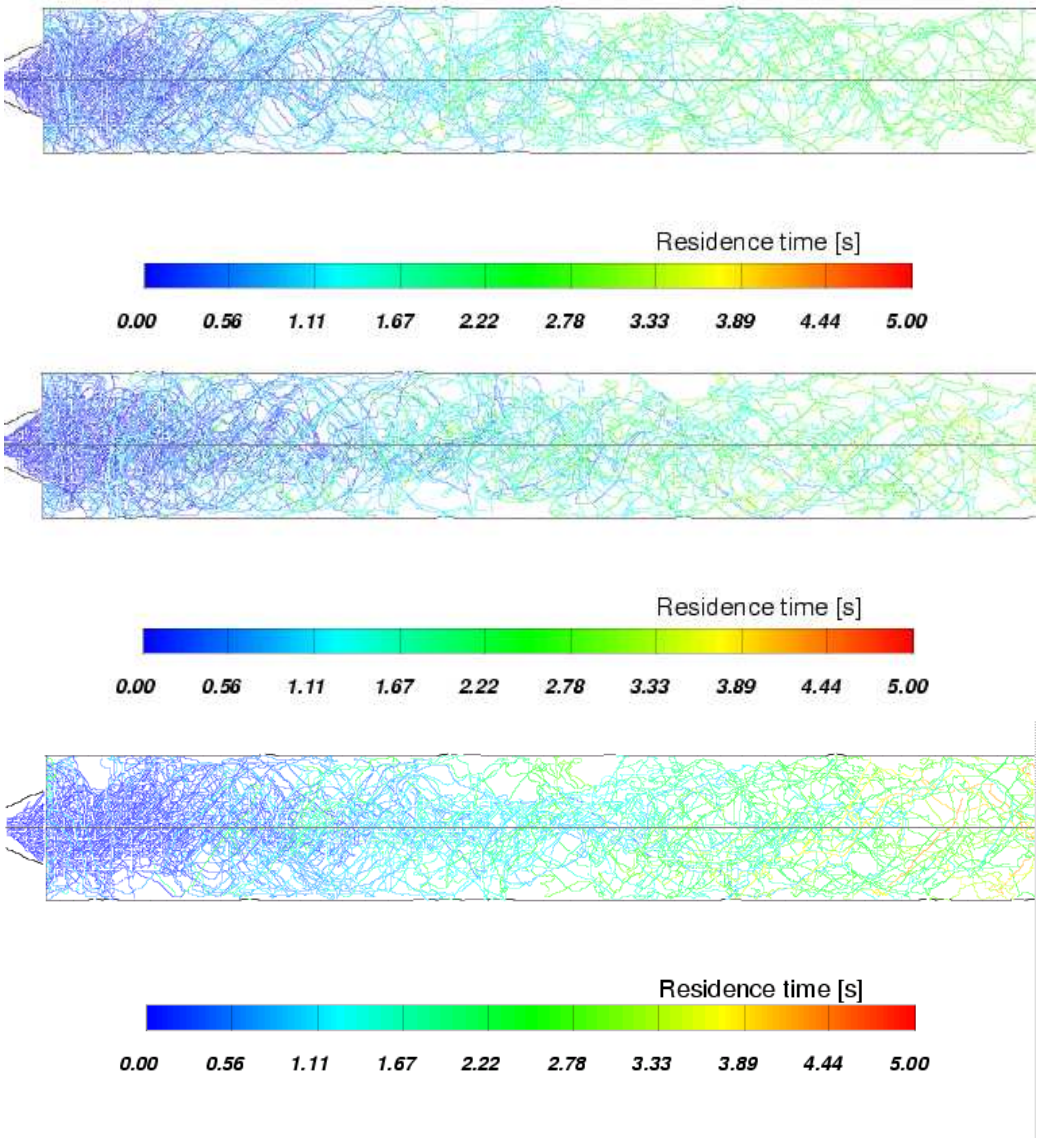

Figure 6.11: Trajectories of equi-volumetric (top to bottom) cylinders, ellipsoids and spheres in the AAU/DTU isothermal test rig using the particle boundary conditions given in table 6.1.

6.6 Summary

Dispersion calculations of small (table 6.1) and large (table 6.2) particles have been performed in a swirling, confined and isothermal flow.

An interesting factor to note for both size classes investigated here is the general similarity between the trajectories of the ellipsoids and cylinders, particularly evident for the large particles. This does seem to indicate that it is the aspect ratio of the axes (β), which is held constant for the two types of particles in the preceding calculations, rather than the superelliptic exponent (n) which governs the influence of the particle

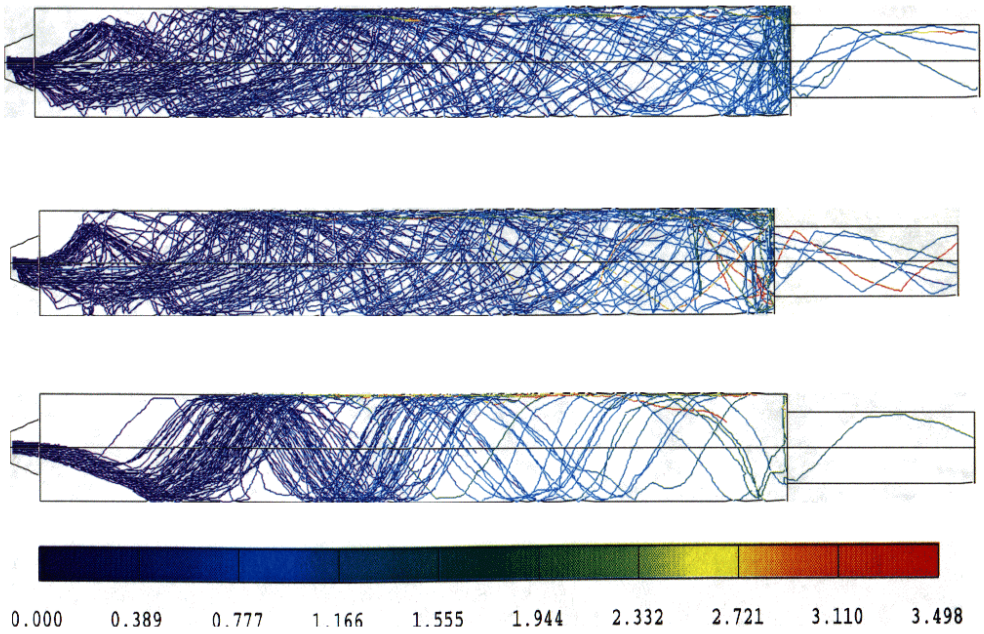

Figure 6.12: Trajectories of (top to bottom) cylinders, ellipsoids and spheres in the AAU/DTU isothermal test rig using the particle boundary conditions given in table 6.2.

shape on the drag coefficient.

Further analysis and verification at this point is hampered, as previously discussed, by the absence of suitable data.

Chapter 7

Testcase: Risø tunnel furnace

The Risø tunnel furnace is equipped with a 1.3MW water cooled pulverised coal burner, and located at the Department of Combustion Technology, Risø National Laboratory. It's a staged burner, with primary air and fuel entering axially through an annular central inlet, and swirled secondary air.

In 1993, extensive measurements of flow, species concentrations and temperature, using advanced technologies were carried out on this furnace firing different types of coal, making it very well suited for model verification. These measurements as well as standard operating conditions are documented in Jensen et al. (1993) and in a series of internal reports.

7.1 Standard operating conditions

For all calculations based on this furnace, the settings for the IFRF type 3 flame are used, as these constitute the most complete set of measurements for validation. The operating conditions are given in table 7.1, and inlet velocities in figure 7.2.

The LDA measurements of the type 3 flame indicate a recirculation zone as shown in figure 7.5.

7.2 Computational configuration

The calculations are performed on a butterfly mesh consisting of approximately 40,000 cells and 48 blocks. Turbulence is included through the $k - \varepsilon$ turbulence closure. The Higher Order Upwind difference scheme is used for the velocity components, and the

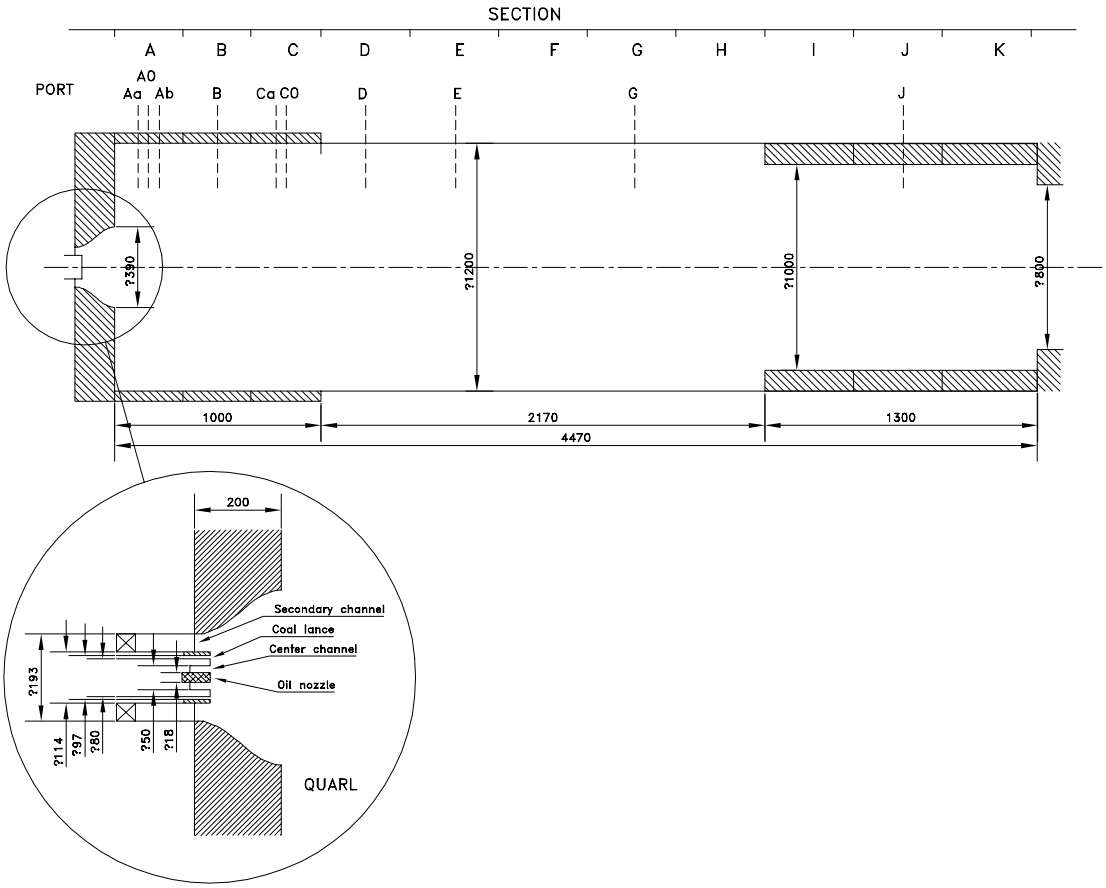

Figure 7.1: The layout of the Risø tunnel furnace, with the burner shown as inset.

Coal type	Columbian Cerrejon
Centre air flow $[m_n^3/h]^a$	50.0
Primary air flow $[m_n^3/h]$	230.0
Secondary air flow $[m_n^3/h]$	1140.0
Centre air temperature $[°C]$	46.0
Primary air temperature $[°C]$	46.0
Secondary air temperature $[°C]$	210.0
Secondary air swirl setting $[-]$	8
Coal mass flow $[kg/h]$	160.0
Excess air ratio	1.2
Loading ratio $[kg\ coal/kg\ air]$	0.085
Input power $[MW]$	1.3

[a] Referred to $273K$ and $1.01325 \times 10^5 Pa$.

Table 7.1: Standard operating conditions for the type 3 flame in the Risø tunnel furnace.

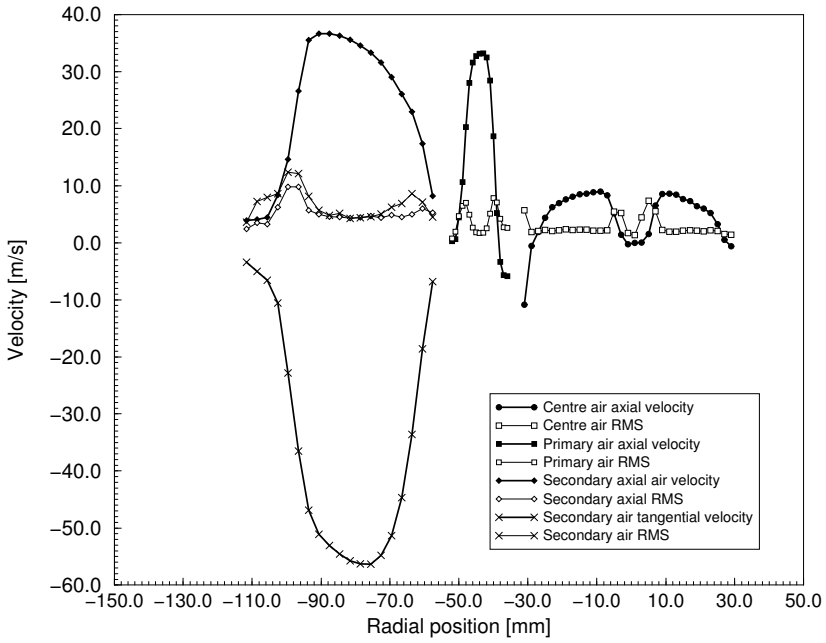

Figure 7.2: Inlet velocities and RMS values for the three inlets of the standard Risø coal burner.

Hybrid Scheme for the turbulent quantities.

The dispersed phase model contain profile lift, drag, viscous torque in the formulation of the equations of motion, with turbulent dispersion included using the eddy lifetime model (section 2.5.1).

7.3 Dispersed phase boundary conditions

Two separate simulations are carried out, one based on spheres and one on cylinders. Considering the results shown in the previous section, the cylinders exemplify the motion of non-spherical particles with large aspect ratios sufficiently, and thus including ellipsoids will most likely not provide more insight. The parameters for each particle type are given in table 7.2. In both cases, the particles are started along a central band in the annular primary inlet, where the coal is injected under standard operating conditions.

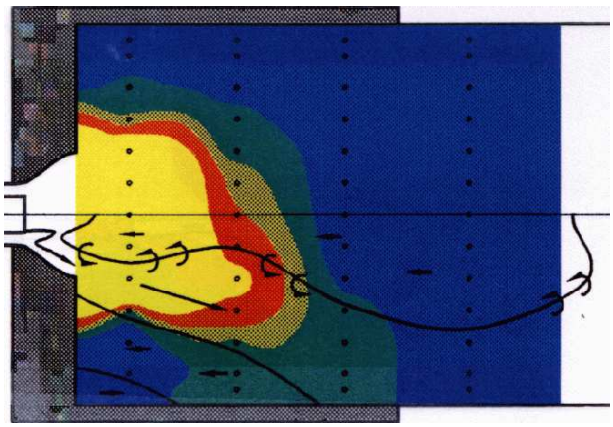

Figure 7.3: Measured recirculation zone boundary for the type 3 flame (Jensen et al 1992).

	Spheres	**Cylinders**
Start position radius $[m]$	0.04425	0.04425
Number of trajectories	5041	5041
Total mass flow $[kg/s]$	0.1	0.1
Diameter range $[\mu m]$	4.0 ... 250.0	200.0 ... 5000.0
Mean diameter $[\mu m]$	50.0	500.0
Aspect ratio	1.0	10.0
Superelliptic exponent	2.0	100.0
Particle density $[kg/m^3]$	2300.0	230.0

Table 7.2: Particle inlet conditions for gas-particle simulations in the Risø tunnel burner.

7.4 Results

7.4.1 Flow patterns

The predicted isothermal gas flow field is shown in figure 7.4. A singly-connected recirculation zone is created, which extends far into the quarl. Two external recirculation zones are also visible (see figure 7.5), one close to the quarl mouth and one in the far corners of the furnace. Comparing the predicted to the measured recirculation zones, it must be kept in mind that the measurements were carried out under combusting conditions, whereas the calculations are isothermal. Nonetheless, common traits are found, and the primary features of the shear layers between the recirculating and non-recirculating flow areas exist in both situations.

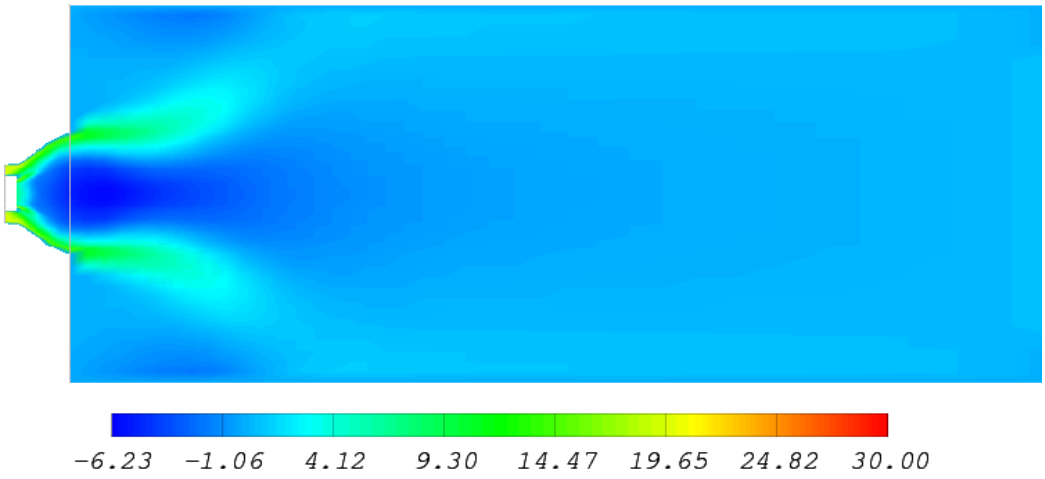

Figure 7.4: Predicted axial velocity in the Risø tunnel furnace.

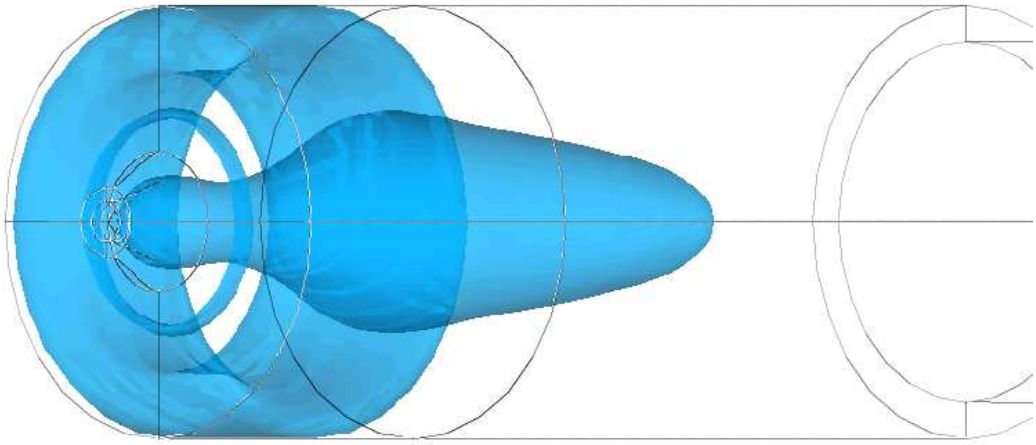

Figure 7.5: Predicted recirculation zones in the Risø tunnel furnace.

7.4.2 Particle trajectories

For combustion applications, a prime factor is the residence time of the fuel in the flame zone and the mixing ability of fuel and oxygen at the same location. These have commonly been achieved by creating a recirculation zone, around the edge of which mixing is greatly enhanced. The solid fuel particles move along the recirculation zone, are sucked into the recirculation zone from the rear and brought to the front of the flame zone, bringing with them hot gases and reactive species.

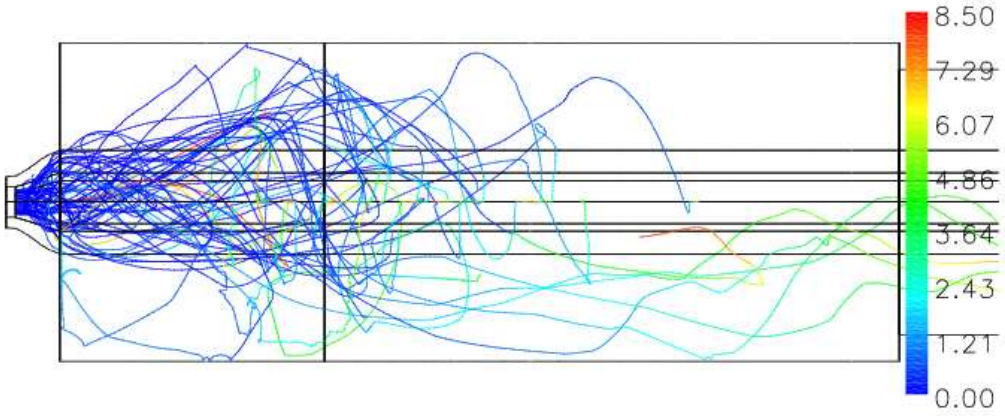

Figure 7.6: Trajectories of cylinders. Only 75 trajectories are shown. Legend designates residence time [s].

The trajectories of the two types of particles show distinct differences in terms of their trajectories, not only in the quarl area, but throughout the entire furnace. Regarding the spheres, the trajectories correspond to the design intentions of pulverised fuel burners, in that most of the particles follow a trajectory around the recirculation zone and are re-injected into the quarl zone through the rear of the recirculation zone.

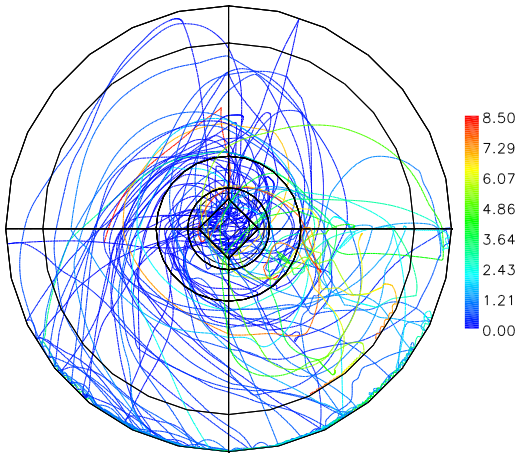

Figure 7.7: End view of trajectories of cylinders. Only 75 trajectories are shown. Legend designates residence time [s].

For the cylinders, the same characteristics as were found for the AAU/DTU isothermal

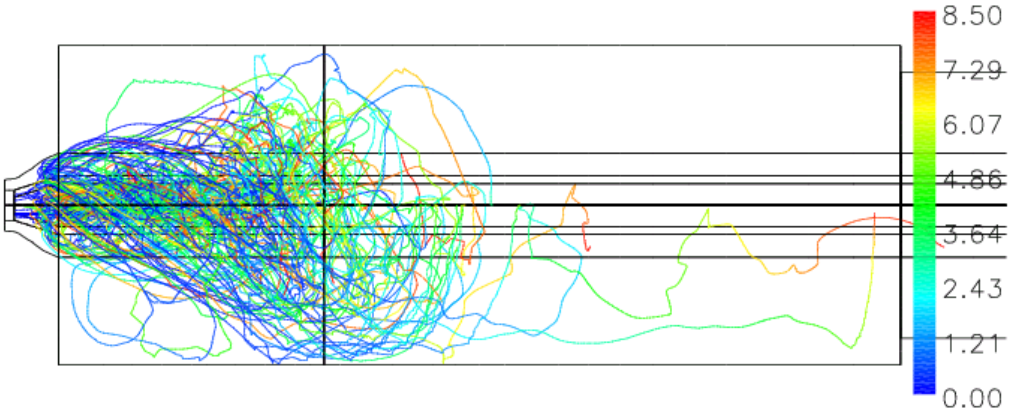

Figure 7.8: Trajectories of spheres. Only 75 trajectories are shown. Legend designates residence time $[s]$.

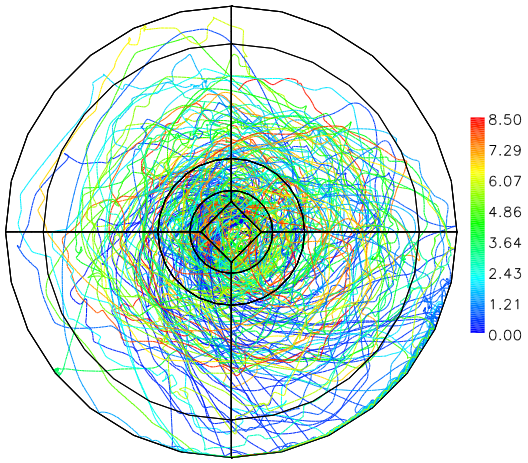

Figure 7.9: End view of trajectories of spheres. Only 75 trajectories are shown. Legend designates residence time $[s]$.

testrig, re-emerge in figures 7.6- 7.7[1]. Although the cylinders are not injected directly in the centre tube of the burner, but in an annulus surrounding it, the dispersion of the cylinders is much more apparent than that of the spheres. Thus, the larger cylinders move to the quarl sides very rapidly, and issue from there into the slow moving gas of the outer furnace area, and only what might be termed "straw dust" is entrained in the recirculation zone.

[1]Limiting the number of displayed trajectories to 75 for clarity causes the trajectories to appear biased, which is not the case when all 5041 trajectories are shown

As a final remark, it is obvious that the aerodynamic properties of the long straw particles demonstrated in this and the preceding chapter in terms of using straw as fuel indicate, that the traditional techniques of injection have to be revised, in order to obtain as homogeneous and controlled combustion environments as possible.

7.5 Summary

Simulations of an isothermal flow in a tubular combustor using spheres and cylinders have been carried out. Based on the conclusions of the previous chapter, ellipsoids are not tracked in this flow configuration.

Although this is an isothermal calculation, important combustion aspects concerning the injection of non-isotropic fuel particles into a furnace can be derived from it. Due to their shape, the cylindrical particles are not only dispersed quicker than the spherical particles, but there is a practically complete absence of reentrainment of the cylinders. This therefore indicates that straw will not, like coal dust, be captured and brought back into the flame zone for complete combustion, leading to a large degree of carbon loss due to unburnt straw particles escaping the flame zone.

Chapter 8

Testcase: MKS1 single combined burner

Unit 1 at Studstrupværket (MIDTKRAFT ENERGY COMPANY) in eastern Jutland, Denmark, is the oldest of the four blocks, comissioned in 1968 and due to be phased out in 1998. It is a 12-burner, wall-fired furnace, with the burners arranged in three rows of four (see figure 8.1). For the combined straw/pulverised coal test, the standard Babcock coal burners in the middle row (level 20 in figure 8.1) have been replaced by combined burners (see enlargement in figure 8.2). The main difference is that the oil lance and ignitor in the centre tube is now replaced by the straw inlet. In order to lower the inflow velocity of the straw, the diameter is increased compared to the standard burner.

8.1 Standard operating conditions

The data given below are the standard operating conditions of Studstrupværkets Unit 1 for a single combined burner. The data is given both as supplied, and transformed to a form suitable as boundary conditions (Dirichlet) for a numerical model.

8.2 Model configuration

For the calculations, a single combined burner is modelled enclosed in a tubular furnace of diameter 2m and length 13m (shown in figure 8.2), in order to study the reacting field in the near-burner zone.

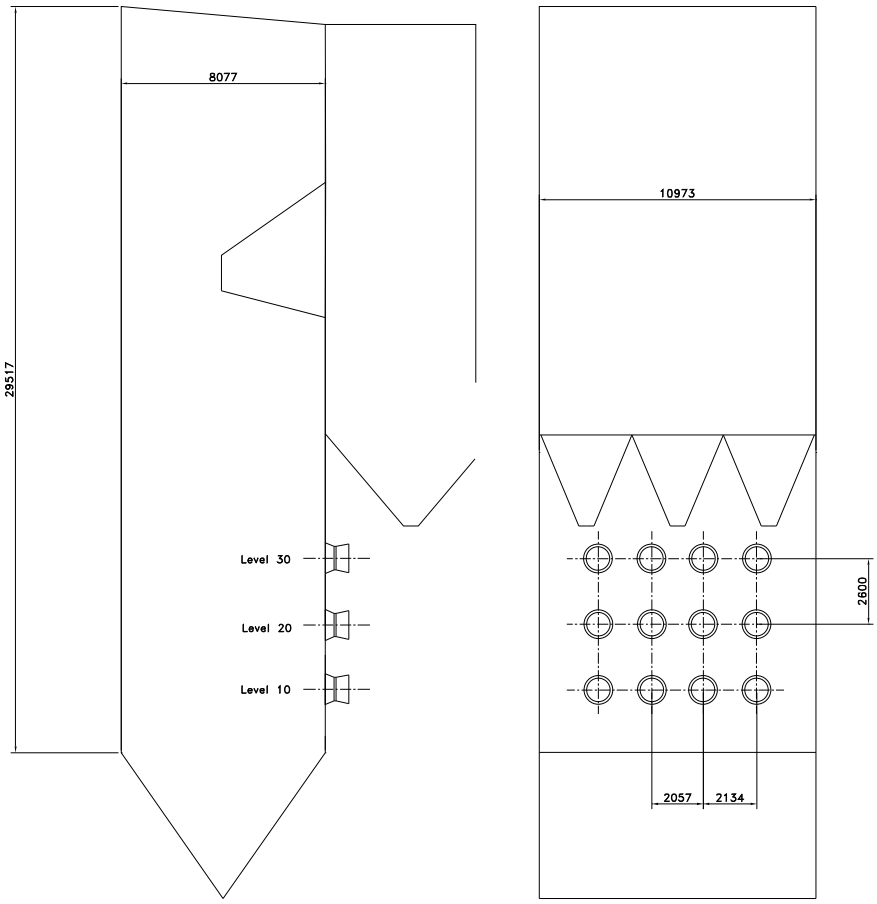

Figure 8.1: Schematic of MKS1. All dimensions are in millimetres.

8.2.1 Computational configuration

The CFD model is based on a structured mesh consisting of approximately 130,000 cells in 32 blocks. Solution of the continuous phase is performed using the Higher Order Upwind differencing scheme for the momentum equations, and Hybrid differencing for mass fractions and turbulence, for which the RNG k-ε turbulence closure is used (CFDS 1995). In order to account for the presence and reaction of coal, the primary air inlet is defined to contain a mass fraction of volatile gas corresponding to the heating value of the coal.

Burner output $[MW]$	38.7
Coal mass flow $[kg/s]$	0.8
Straw mass flow $[kg/s]$	1.32
Coal dust inlet velocity $[m/s]$	17.3
Straw inlet velocity $[m/s]$	16.2
Centre air mass flow $[kg/s]$	0.88
Centre air temperature $[K]$	343.0
Centre air density $[kg/m^3]$	1.03
Primary air mass flow $[kg/s]$	1.98
Primary air temperature $[K]$	343.0
Primary air density $[kg/m^3]$	1.03
Secondary air mass flow $[kg/s]$	13.52
Secondary air temperature $[K]$	553.0
Secondary air density $[kg/m^3]$	0.64
Swirl vane angle ϕ [deg]	60.0

Table 8.1: Standard operating conditions for a single combined burner at MKS1

Primary inlet area $[m^2]$	0.126
Primary air axial velocity $[m/s]$	19.57
Primary air radial velocity $[m/s]$	0.0
Primary air tangential velocity $[m/s]$	0.0
Secondary inlet area $[m^2]$	0.526
Secondary air axial velocity $[m/s]$	40.16
Secondary air radial velocity $[m/s]$	0.0
Secondary air tangential velocity $[m/s]$	65.56
Secondary air swirl number S_w	1.15
Centre inlet area $[m^2]$	0.053
Centre air axial velocity $[m/s]$	20.8
Centre air radial velocity $[m/s]$	0.0
Centre air tangential velocity $[m/s]$	0.0

Table 8.2: Boundary data for a single combined burner at MKS1

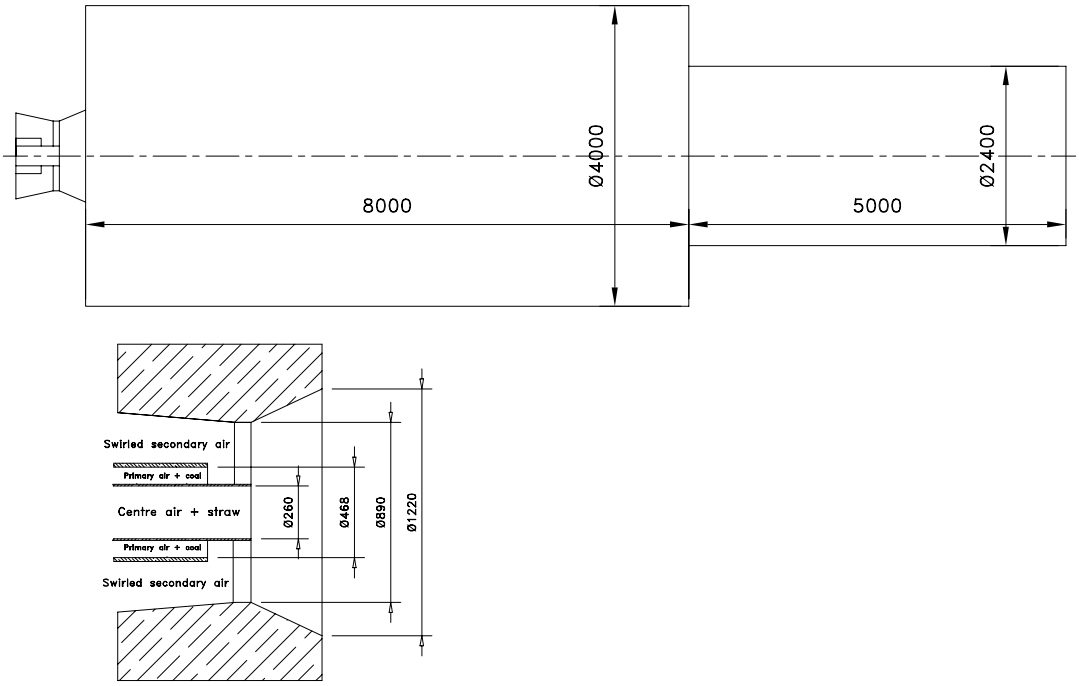

Figure 8.2: Schematic of the model combustion chamber with a single combined burner shown below.

8.2.2 Dispersed phase boundary conditions

The mass flow is assumed to enter in five radial positions, based on the assumption that most of the mass flow is transported in an annular band with a maximum at approximately 2/3 of the inlet radius. This is illustrated in figure 8.5.

In order to use the two-step gas combustion model (equation 3.41), knowledge of the

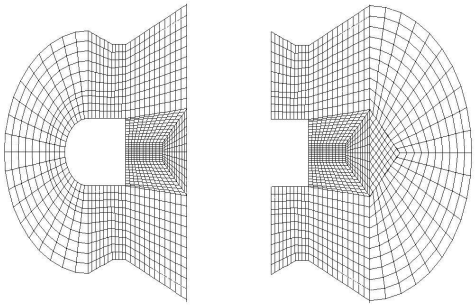

Figure 8.3: Detail of butterfly mesh structure in burner and quarl.

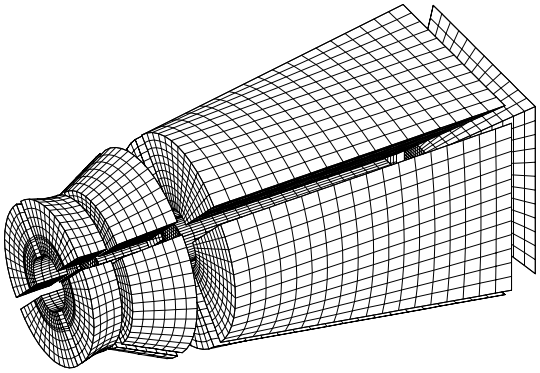

Figure 8.4: 3D view of the combined burner mesh.

Start position radius $[m]$	**0.02**	**0.05**	**0.07**	**0.09**	**0.11**
Number of trajectories	250	250	250	250	250
Total mass flow $[kg/s]$	0.132	0.198	0.33	0.396	0.264
Diameter range $[\mu m]$	50.0 ... 100.0	75.0 ... 200.0	150.0 ... 500.0	750.0 ... 1000.0	1000.0 ... 5000.0
Aspect ratio range	1.0 ... 10.0	5.0 ... 20.0	25.0 ... 50.0	25.0 ... 50.0	5.0 ... 10.0
Exponent	2.0	10.0	25.0	100.0	100.0

Table 8.3: Inlet conditions for gas-particle simulations in a single MKS1 combined burner.

constituents of the volatiles emitted from the straw is neccessary. Using table 1.1 and the composition values of the straw used for the single particle burn out calculations in Chapter 5, and assuming that the oxygen content can be determined by balance, the data shown in table 8.4 for 1 kmol volatile is obtained.

C content $[kmol/kmol]$	0.213
H content $[kmol/kmol]$	0.50
O content $[kmol/kmol]$	0.282
Molecular mass $[kg/kmol]$	7.568
Heating value $[MJ/kg]$	14.43

Table 8.4: Atomic data and heating value of volatile gas from the straw.

In the particle equations of motion (equations 2.6 and 2.2- 2.4), aerodynamic drag, profile lift and flow field vorticity are included. Heterogeneous combustion is based on the mixed control model (section 3.2.1) with kinetic parameters as defined in Chapter 5.

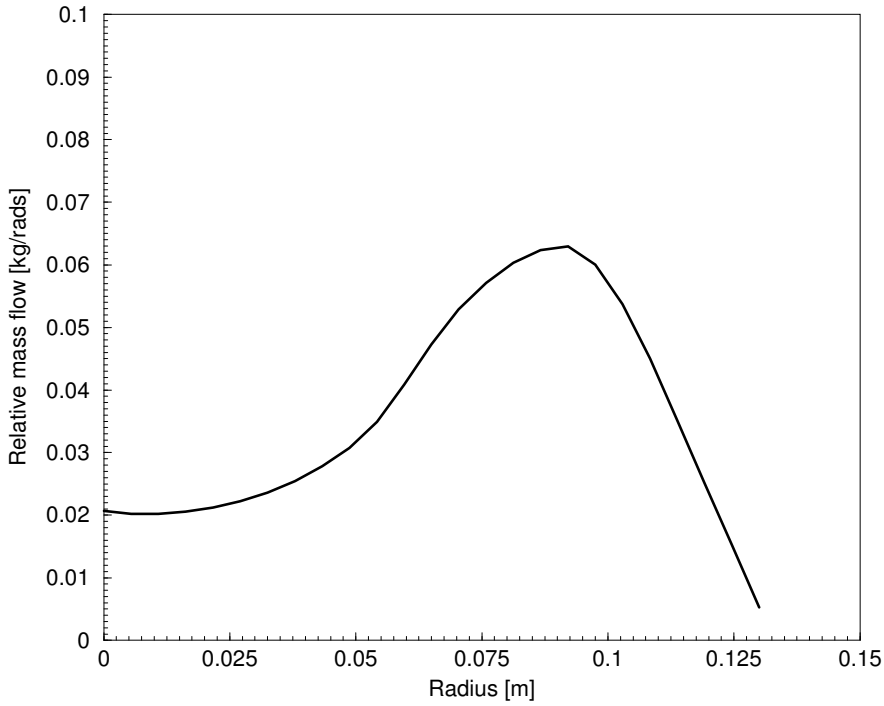

Figure 8.5: Radial mass flow distribution in the centre inlet of an MKS1 combined burner.

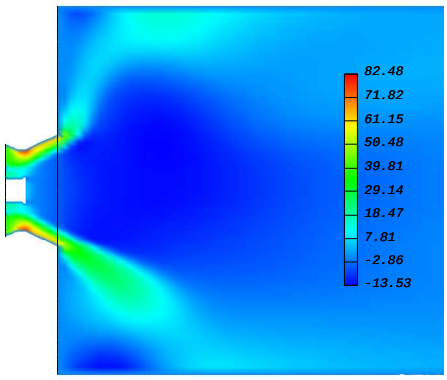

Figure 8.6: Near burner axial velocity contours without centre air.

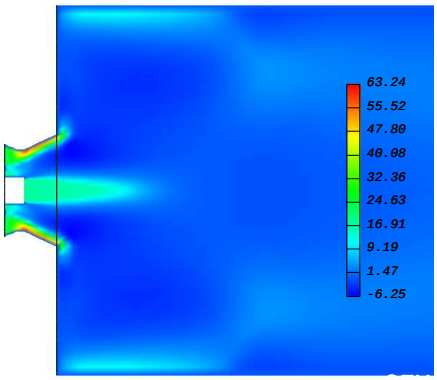

Figure 8.7: Near burner axial velocity contours with centre air.

8.3 Results

8.3.1 Isothermal flow patterns in coal and combined burners

In order to be able to discern all features of introducing straw into the centre air, isothermal calculations of combined burners with centre air (figure 8.7) as well as stan-

dard coal burners with no centre air (figure 8.6), have been performed. These show, not surprisingly, very different near-burner flow patterns. When introducing centre air in the combined burners, the recirculation zone is weakened substantially, and the centre air penetrates far into what is the flame zone for the standard coal burner. It should thus be expected that the aerodynamics in this region, which influence the combustion behaviour of the straw particles, are not comparable to those of the standard coal burner.

8.3.2 Coupled flow patterns

The coupled calculations have proven to be very unstable (as indicated in the residual plot in figure 8.8), and a fully converged solution has only been obtained for the first calculation of the flow field. Thus, only particle processes will be discussed in the following, as the flow and temperature fields are meaningless.

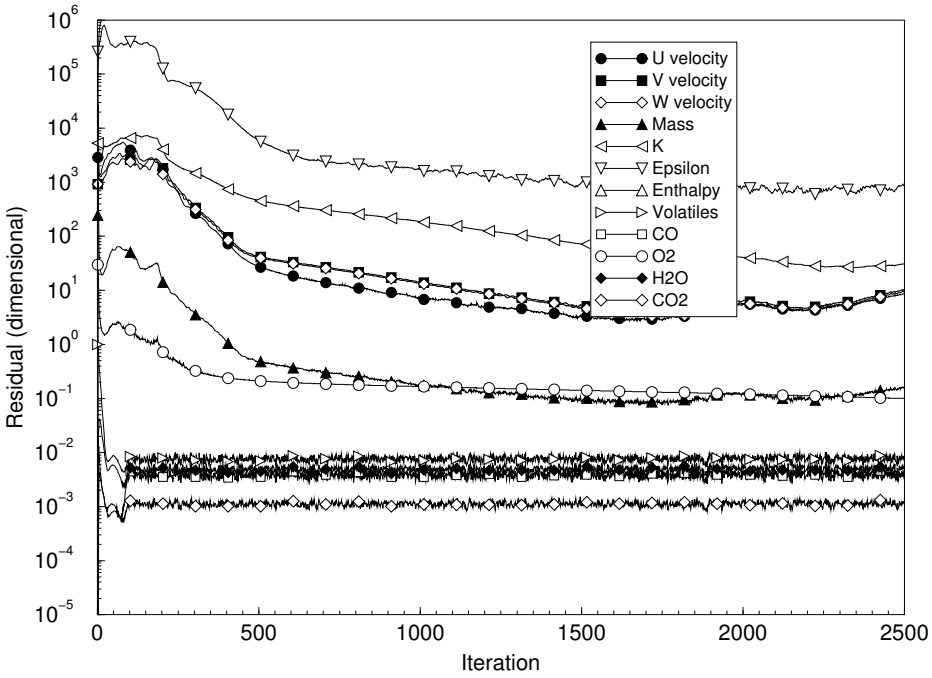

Figure 8.8: Residuals for the coupled flow calculations.

8.3.3 Particle trajectories

The particle trajectories for the straw are shown in figures 8.9 and 8.10. For these calculations, the particles react with the surrounding gas, exchanging mass and energy, and therefore the size of the particles shrinks, as these reactions undergo. Therefore

the trajectories are not quite as obviously different from what would be expected of spheres, but nevertheless, no or very little re-entrainment of fuel particles into the flame zone is evident. What does happen, is that some particles are brought back to the edge of the quarl mouth, but outside the flame zone, where in some cases they collide with the quarl exit wall, causing some slagging to occur here. This is also found in the MKS1 furnace for the combined burner level (Junker 1997).

Furthermore, a number of large particles can be seen to escape the furnace, containing unburnt carbon. This is also a documented feature of the combustion performance of MKS1 (Overgaard 1997).

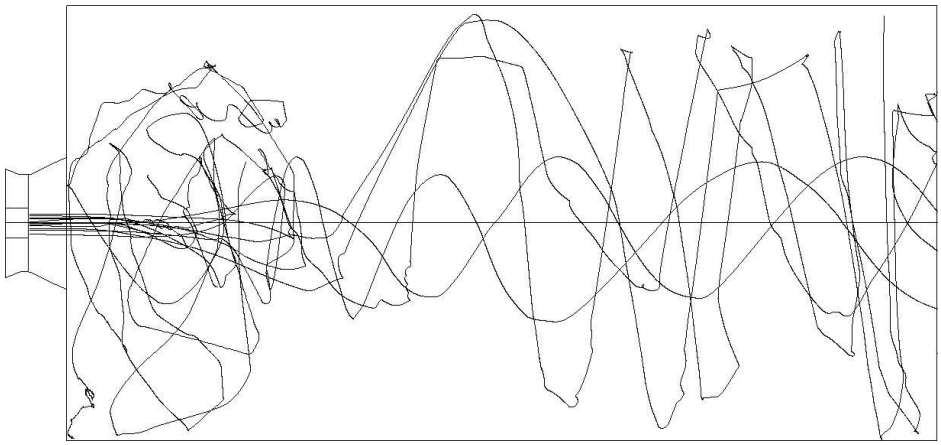

Figure 8.9: Straw particle trajectories in the MKS1 model combustor. Side view.

8.3.4 Particle combustion patterns

Due to the relatively large particles injected into the flame at high velocity, the heating rate experienced by the particles is not sufficient to bring devolatilization to an end in the near burner zone, and strands of volatile gas are formed as shown in figure 8.11. Furthermore, the heterogeneous reaction of the straw is delayed not only due to the slow heating, but also due to the large amount of volatile gas to be released over quite a long period. These effects combine to shift the flame zone downstream, and detach it from the burner mouth.

8.4 Summary

The coupled calculations of the MKS1 model combustor, though not converged, indicate a number of traits found also at the existing furnace, and thus serve to corroborate the

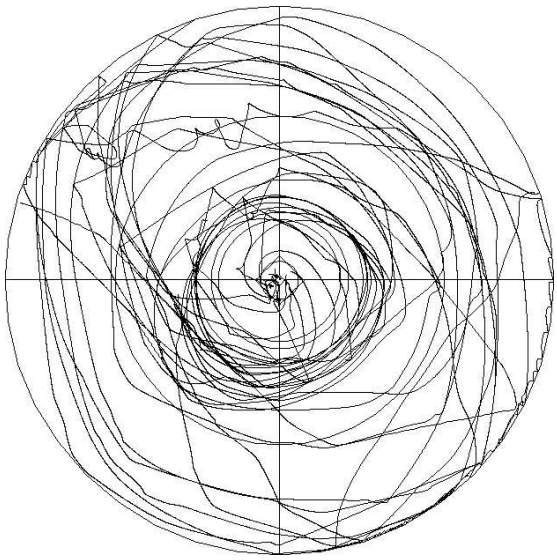

Figure 8.10: Straw particle trajectories in the MKS1 model combustor. End view.

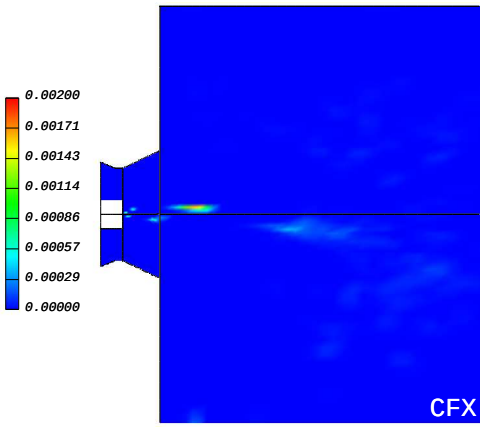

Figure 8.11: Rate of volatiles release $[kg/s]$ from the straw particles.

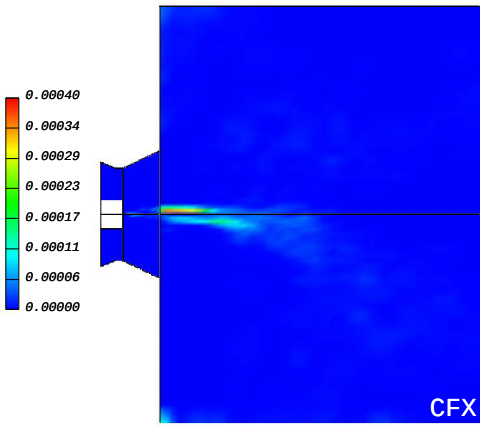

Figure 8.12: Rate of CO production $[kg/s]$ from the burning straw particles.

current approach as a valid tool in the analysis of this type of co-fuelled systems. The conclusions of the isothermal calculations of Chapter 7 concerning the problems of injecting straw into an existing coal flame can also be drawn on the basis of the above results. For the MKS1 combi- burners, the problems are actually made more severe by introducing a large momentum flux through the centre air inlet, weakening the recirculation zone, and subsequently allowing all but the small straw particles to pass straight through the flame zone.

In terms of the modelling, problems have been encountered not only obtaining convergence, but also in inlet configurations, as the CFD solver only allows one type of gaseous fuel. Using the built-in particle combustion model prohibits the use of the

two-step gas combustion model, so the presence of the coal has been modelled using an amount of volatile gas with the same composition and heating value as the volatiles from the straw, corresponding to the power input of the coal.

Concerning the coupled calculations, this model configuration has not proved successful, and a new approach to coupling the phases must be devised. One possible technique would be to reformulate the built-in particle model of the CFD solver in the superelliptic scheme.

.

Chapter 9

Conclusions and Perspective

The objective of this research project has been twofold: to develop and implement suitable models for the simulation of the aerodynamic behaviour of non-spherical particles, and to apply these models to burners firing solid fuels. The emphasis has been on solid fuels which deviate, in terms of shape and composition, from conventional solid fuels such as pulverised coal, which can be modelled aerodynamically as spheres and for which several well-proven combustion models exist. This work has been motivated by the growing environmental awareness and a desire for knowledge of the details of co-firing, through the ability to model the reactive two-phase flow of such burners.

These objectives have lead to the development of a numerical framework for the aerodynamic and combustion behaviour of a superelliptic particle class, with shapes characterised by an elliptic equation capable of assuming shapes ranging from spheres to cylinders, by simple parameter variation. A prime feature of the new model is its similarity to the existing Lagrangian particle tracking methodology, allowing for relatively easy implementation in existing CFD codes. Models accounting for the aerodynamic properties as well as combustion behaviour of these particles have been implemented in the Lagrangian particle tracking and combustion code PCOMBUST, which bases its predictions on a flow basis provided by an arbitrary flow solver, for this work the commercial CFD code CFX4.2.

Improved C_D formulation
Based on the concept of aerodynamical similarity, an improved C_D formulation has been developed, allowing for the conventional case of spheres, but also accounting for deviations from this shape, based on the superelliptic shape function. The use of the drag coefficient has been validated through terminal velocity calculations of differently shaped particles compared to experimental data.

Implementation and code interaction
Implementing a complete Lagrangian particle model for tracking and combustion, and coupling it to an existing flow solver, where also the combustion part is external, is prone

to instabilities. For the current model, couplings of iso-thermal gas- particle simulations have been without problems, whereas coupling reacting simulations has proven to be very difficult. The difficulty lies not in the Lagrangian part, but in the flow solver, where the dominant part of the combustion is performed. For CFX4, implementing the two-step reaction mechanism for hydrocarbon combustion has been the weak point, with problems in terms of oscillating residuals and time-consuming calculations. In order to remedy this, the mixture fraction formulation has been discontinued, and transport equations for all species defined, but with no significant improvement.

Combustion applications
Applying a non-spherical particle model to combustion configurations shows a lot of promise. The ability to handle non-conventional fuels in a CFD context is important, as well as the documentation that existing heterogeneous combustion models, based on a spherical particle shape, can be used for these fuels and still obtain plausible results.

For the specific case of the MKS1 combined burner, the question arises: what causes the shift in combustion pattern, changed aerodynamics, particle kinetics, particle aerodynamics, or a combination of these? Clearly, the safe answer is a combination of effects, most probably also the most correct answer, but nonetheless it is difficult to pinpoint where to concentrate efforts to provide as efficient and well-documented combined burners for future retrofitting of existing or design of new co-fuelled furnaces. Broad design guidelines for combined burners can be deduced from the results of the testcases, though, in terms of ensuring a very strong recirculation zone and injecting the straw particles in such a way, that even the large straw particles are re-entrained into the flame zone, in spite of the highly dispersive flow characteristics.

Choice of testcases
Retrospectively, the choice of testcases for the current work has not been ideal, as the flow in swirl burners is very complex, and it has been difficult to isolate different characteristics of particle motion. Simple shear flows, such as a backward facing step, would have been more appropriate at this stage of the model development. However, the objective of the work to be used in connection with co- fuelled swirl burners influenced the choice of the testcases to be of the same type as the final application.

Future work
In order to further enhance the non-spherical particle model, it is neccessary to validate the models to a greater extent than has been possible in the current work, and also to provide fundamental data regarding lift, drag and torque on superelliptic particles.

Future work in combustion applications necessitates that the CFD code - commercial or academic - allows for multiple solid as well as gaseous fuels, in order to account not only for the co-firing, but also for the different volatile compositions of the fuels.

Finally, for those not familiar with the Danish language, the citation at the beginning of Chapter 1 by Piet Hein translates roughly to " *When the large electronic brains are not busy with specific tasks, they speculate on numbers in general.*"

Bibliography

Anderson, J. D. (1985). *Introduction to Computational Fluid Dynamics*. Lecture Series 1985-01. Rhode-Saint-Genese, Belgium: von Karman Institute for Fluid Dynamics.

Astrup, P. (1992, February). *Turbulent gas-particle flow*. Ph. D. thesis, Department of Combustion Research, Risø National Laboratory, Denmark.

Astrup, P. and E. Gjernes (1988). Udvikling af EDB-model for stationær turbulent 3-D gas-partikel strømning. Technical Report M-2759, Department of Combustion Research, Risø National Laboratory, Denmark. In Danish.

Badzioch, S. and P. Hawksley (1970). Kinetics of thermal decomposition of pulverised coal particles. *Industrial Engineering Chemistry Process Design and Development 9*, 521.

Besnard, D. and F. Harlow (1986). Nonspherical particles in two-phase flow. *International Journal of Multiphase Flow 12*(6), 891–912.

Biede, O., L. Sørensen, and R. Peck (1992). Pyrolyse og antændelse af kul ved kulstøvsfyring. Technical Report EFP-88 1323/88-23, Energiministeriets forskningsudvalg for produktion og fordeling af el og varme. In Danish.

Bird, R., W. Stewart, and E. Lightfoot (1960). *Transport phenomena*. New York: John Wiley and Sons.

Boyd, R. and J. Kent (1986). Three-dimensional furnace computer modelling. In *21st Symposium (International) on Combustion*, pp. 265–274. The Combustion Institute.

Brauer, H. (1971). *Grundlagen der Einphasen- und Mehrphasenströmungen*. Grundlagen der Chemischen Technik - Verfahrenstechnik der chemischen und verwandter Industrien. Aarau, Switzerland: Verlag Sauerländer Aarau. In German.

Brenner, H. (1964a). The Stokes resistance of a slightly deformed sphere. *Chemical Engineering Science 19*, 519–539.

Brenner, H. (1964b). The Stokes resistance of an arbitrary particle - II. an extension. *Chemical Engineering Science 19*, 599–629.

Brenner, H. (1964c). The Stokes resistance of an arbitrary particle - III. shear fields. *Chemical Engineering Science 19*, 631–651.

Brenner, H. (1964d). The Stokes resistance of an arbitrary particle - IV. arbitrary fields of flow. *Chemical Engineering Science 19*, 703–727.

Brenner, H. and D. Condiff (1972, November). Transport mechanics in systems of orientable particles. III arbitrary particles. *Journal of Colloid and Interface Science 41*(2), 228–274.

CFDS (1994, June). *CFDS-FLOW3D Release 3.3 user guide*. 8.19 Harwell, Didcot, Oxfordshire OX11 0RA, UK: Computational Fluid Dynamics Services, AEA Technology.

CFDS (1995, October). *CFX4.1 Flow Solver User Guide*. 8.19 Harwell Laboratory, Oxfordshire OX11 0RA, UK: Computational Fluid Dynamics Services, AEA Technology plc.

Chiang, C., M. Raju, and W. Sirignano (1992). Numerical analysis of convecting, vaporizing fule droplet with variable properties. *International Journal of Heat and Mass Transfer 35*, 1307–1324.

Christiansen, E. and D. H. Barker (1965). The effect of shape and density on the free settling of particles at high Reynolds numbers. *AIChE Journal 11*(1), 145–151.

Crowe, C. (1997). Personal communication.

Crowe, C., M. Sharma, and D. Stock (1977). The Particle-Source-In Cell (PSI-Cell) model for gas-droplet flows. *Journal of Fluids Engineering 99*(2), 325–332.

Crowe, C., M. Sommerfeld, and Y. Tsuji (1998). *Multiphase Flows with droplets and particles*. Mechanical and Chemical Engineering. CRC Press LLC.

Dall, H. (1988, December). Development of a computer model for stationary turbulent 3-D gas-particle flows: Characteristic parameters of gas-particle flow. Technical Report M-2758, Risø National Laboratory, Denmark.

ELSAMPROJEKT (1994, August). Kemiske brændselsdata for dansk træflis. Internal note. In Danish.

Fan, F.-G. and G. Ahmadi (1995, March). Dispersion of ellipsoidal particles in an isotropic pseudo-turbulent flow field. *Journal of Fluids Engineering 117*, 154–161.

Finn, R. (1953). Determination of the drag on a cylinder at low Reynolds numbers. *Journal of Applied Physics 24*(6), 771–773.

Flachsbart, O. (1927, July). Neue Untersuchungen über den Luftwiederstand von Kugeln. *Physikalische Zeitschrift 28*(13), 461–469. In German.

Fredsøe, J. (1991). *Hydrodynamik* (2 ed.). Danmarks Tekniske Højskole (DTU): Den Private Ingeniørfond. In Danish.

Gallily, I. and A.-H. Cohen (1979, February). On the orderly nature of the motion of nonspherical aerosol particles. ii. inertial collision between a spherical large droplet and an axially symmetrical elongated particle. *Journal of Colloid and Interface Science 68*(2), 338–356.

Gibb, J. (1985). Combustion of the residual char remaining after devolatilisation. Lecture at the Three Day Intensive Course on PC Combustion,Mechanical Engineering Dept., Imperial College, London.

Grant, G. and W. Tabakoff (1975). Erosion prediction in turbomachinery resulting from environmental solid particles. *Journal of Aircraft 12*(5), 471–478.

Haider, A. and O. Levenspiel (1989). Drag coefficient and terminal velocity of spherical and nonspherical particles. *Powder Technology 58*, 63–70.

Hein, P. (1964). Superellipsen - en enkel løsning af et alment problem. *Dansk Kunsthåndværk 37*(4), 97–112. In Danish.

Hörner, S. F. (1965). *Fluid-dynamic drag - theoretical, experimental and statistical information.* Published by the author.

Jacobsen, C. B. (1997, June). *Large Eddy Simulation of confined swirling flows - a numerical study.* Ph. D. thesis, Institute of Energy Technology, Aalborg University, Denmark.

Jeffery, G. (1922). The motion of ellipsoidal particles immersed in a viscous fluid. *Proceedings of the Royal Society 102A*, 161–179.

Jensen, P., M. Kirkegaard, J. Bak, O. Rathmann, and S. Clausen (1992). Local measurements in three 1.3mw pulverized coal flames volume II. Technical Report R-636, Department of Combustion Research, Risø National Laboratory, Denmark.

Jensen, P., O. Rathmann, S. Clausen, and J. B. et al (1993). Measurements for the validation of advanced laser-based instrumentation ... Technical Report R-637(EN), Department of Combustion Research, Risø National Laboratory, Denmark.

Jensen, P., M. Stenholm, and K. Jørgensen (1994). Interview og litteratur-undersøgelse af halms udbrændings- og belægningsegenskaber. Technical Report R-786(EN), Department of Combustion Research, Risø National Laboratory, Denmark. In Danish.

Junker, H. (1997, November). *Cofiring biomass and coal. Plant comparisons and experimental investigation of deposit formation.* Ph. D. thesis, Institute of Energy Technology, Aalborg University, Denmark.

Kær, S. K. and K. K. Nielsen (1996, June). Numerical modelling of turbulent reacting sprays. Master's thesis, Institute of Energy Technology, Aalborg University, Denmark.

Kenning, V. and C. Crowe (1997). On the effect of particles on carrier phase turbulence in gas-particle flows. *International Journal of Multiphase Flow 23*(2), 403–408.

Lau, C. and S. Niksa (1992). The combustion of individual particles of various coal types. *Combustion and Flame 90*(1), 45–70.

Levenspiel, O. (1972). *Chemical reaction engineering.* New York: John Wiley & Sons.

Liebster, H. (1927). Über den Widerstand von Kugeln. *Annalen der Physik 4*(F82), 541–562. In German.

Magnussen, B. and B. Hjertager (1976, August). On mathematical models of turbulent combustion with special emphasis on soot formation and combustion. In *16th Symposium (Int'l) on Combustion*. The Combustion Institute.

Marchildon, E., A. Clamen, and W. Gauvin (1964, August). Drag and oscillatory motion of freely falling cylindrical particles. *The Canadian Journal of Chemical Engineering* , 178–182.

Maxey, M. (1990). On the advection of spherical and non-spherical particles in a non-uniform flow. *Phil Trans. R. Soc. Lond 333*, 289–307.

Maxey, M. and J. Riley (1983, April). Equation of motion for a small rigid sphere in a nonuniform flow. *Physics of Fluids 26*(4), 883–889.

Mostafa, A. and H. Mongia (1988). On the interaction of particles and turbulent fluid flow. *International Journal of Heat and Mass Transfer 31*(10), 2063–2075.

Nielsen, S. (1986). *Strømningsinducerede svingninger* (1 ed.). Hydraulics and Coastal Engineering Laboratory, Aalborg University, Denmark: Aalborg Tekniske Universitetsforlag.

Niksa, S. (1995, February). Predicting the devolatilization behavior of any coal from its ultimate analysis. *Combustion and Flame 100*(3), 384–394.

Overgaard, P. (1997). Personal communication. MIDTKRAFT ENERGY COMPANY.

Paulsen, B. B. and M. Holst (1993, June). Numerisk simulering af 3-D partikel-gas strømninger i udskilningsgeometrier. Master's thesis, Institute of Energy Technology, Aalborg University, Denmark. In Danish.

Press, W., S. Teukolsky, W. Vetterling, and B. Flannery (1992). *Numerical recipes in FORTRAN. The art of scientific computing* (2 ed.). Cambridge University Press.

Rasmussen, N. (1986). *Numerisk modellering af turbulent strømning og forbrænding i forbrændingsrum*. Ph. D. thesis, Laboratoriet for Varme- og Klimateknik, Technical University of Denmark. In Danish.

Rosendahl, L. (1995). On numerical modelling of multi-dimensional gas-particle reacting flows. In R. Larsson and N.-E. Wiberg (Eds.), *NSCM VIII - Eighth Nordic Seminar on Computational Mechanics*, Publication 95:15. NoACM - Nordic Association for Computational Mechanics: Chalmers University of Technology.

Rosendahl, L. (1996a). Analysis of combi-burner for coal and straw using FLUENT - Using FLUENT to prepare experimental campaigns at enel-crt. Technical report, ENEL-CRT, Pisa, Italy.

Rosendahl, L. (1996b). *PCOMBUST Users Manual version 3.0* (1 ed.). Aalborg University, Denmark: Institute of Energy Technology.

Rosendahl, L. (1997, October). Qualitative CFD and experimental prediction of the aerodynamic properties of superelliptic particles. In *Proceedings of the 4th International CFX User Conference*, 8.19 Harwell, Didcot, Oxfordshire OX11 0RA, UK, pp. 210–215. AEA Technology plc.

Rusaas, J. (1995, January). Numerical simulation of gas-particle flows. Technical Report I14950019, Institute of Energy Technology, Aalborg University, Denmark.

Rusaas, J. (1998, February). *Numerical simulation of gas-particle flow linked to pulverized coal combustion.* Ph. D. thesis, Institute of Energy Technology, Aalborg University, Denmark.

Saffman, P. (1965). The lift on a small sphere in a slow shear flow. *Journal of Fluid Mechanics 22*(2), 385–400. Corrigendum in *Journal of Fluid Mechanics 31*, 624.

Schmiedel, J. (1928, September). Experimentelle Untersuchungen über die Fallbewegung von Kugeln und Scheiben in reibenden Flüssigkeiten. *Physikalische Zeitschrift 29*(17), 593–610. In German.

Serio, M., D. Hamblen, J. Markham, and P. Solomon (1987). Kinetics of volatile product evolution in coal pyrolysis: Experiment and theory. *Energy and Fuels 1*, 138–152.

Shuen, J.-S., L.-D. Chen, and G. Faeth (1983). Evaluation of a stochastical model of particle dispersion in a turbulent round jet. *AIChE Journal 29*(1), 167–170.

Shuen, J.-S., A. Solomon, Q.-F. Zhang, and G. Faeth (1985, March). Structure of particle-laden jets: Measurements and predictions. *AIAA Journal 23*(3), 396–404.

Simonin, O. (1996). Continuum modelling of dispersed two-phase flows. In *Combustion and turbulence in twp-phase flows*, Lecture series 1996-02. Rhode-Saint-Genese, Belgium: von Karman Institute for Fluid Dynamics.

Sirignano, W. (1993). Fluid dynamics of sprays - 1992 Freeman Scholar Lecture. *Journal of Fluids Engineering 115*, 345–378.

Smoot, L. and D. Pratt (Eds.) (1979). *Pulverized-coal combustion and gasification. Theory and applications for continuous flow processes.* New York: Plenum Press.

Smoot, L. and P. Smith (1985). *Coal combustion and gasification.* The Plenum Chemical Engineering Series. New York: Plenum Press.

Sørensen, L. (1996, May). *Fuel reactivity as a function of temperature, pressure and conversion.* Ph. D. thesis, Department of Combustion Research, Risø National Laboratory, Denmark.

Sørensen, L., O. Biede, and R. Peck (1994). An experimental study of high-temperature, oxidative pulverized coal devolatilization. In *25. Symposium (International) on Combustion*, pp. 475–483. The Combustion Institute.

Stoholm, P. and M. Kirkegaard (1992). Eksperimentel bestemmelse af halmknæs udbrændingstid. Department of Combustion Research, Risø National Laboratory, Denmark. In Danish.

Versteeg, H. and W. Malalasekera (1995). *An introduction to Computational Fluid Dynamics - the finite volume method*. Longman Scientific and Technical.

Wieselsberger, C. (1922). Weitere feststellung uber die Gesetze des Flussigkeits- und Luftwiederstandes. *Physikalische Zeitschrift 23*, 219–224. In German.

Zachariassen, A. and L. Rosendahl (1994, June). Numerical modelling of particle combustion - a computer model of multidimensional reacting gas-particle flows. Master's thesis, Institute of Energy Technology, Aalborg University, Denmark.

Zhou, Q. and M. Leschziner (1991). A Lagrangian particle dispersion model based on a time-correlated stochastic approach. *Gas-Solid Flows, ASME 121*, 255–261.

APPENDICES

Appendix A

Approaches to non-spherical particle modelling

The surface shape of a particle plays an important role not only in the aerodynamical behaviour of a moving particle, but also in it's combustion behaviour. When dealing with straw, and, indeed, particles in general, the spherical shape suffers severe shortcomings, and a different shape must be chosen, in order to describe the behaviour of a more general class of particles.

The following outlines some of the different techniques of non-spherical particle modelling.

A.1 The ellipsoid at Stokes conditions

The original paper by Dr. G.B. Jeffery in 1922 forms the foundation of the majority of non-spherical particle models used even in the 1990's, as well as much of the work done on removing the shape constraint of the ellipsoid which is inherent in the work of Jeffery.

Before developing the model, Jeffery imposed the following constraint upon it:

> *"..that the condition for the validity of this approximation is that the product of the velocity of the ellipsoid by its linear dimensions shall be small compared with the "kinematic coefficient of viscosity" of the fluid. In relation to our present problem, it will therefore be satisfied either for sufficiently slow motions, or for sufficiently small particles."*

The shape of the fully ellipsoidal particles is given by

$$\frac{x'^2}{a^2} + \frac{y'^2}{b^2} + \frac{z'^2}{c^2} = 1 \tag{A.1}$$

a, b, c: particle semi-axis dimensions $[m]$

$[x', y', z']$: co-rotational coordinate system $[m]$

It should be noted, that in the original work of Jeffery, the notation $[x', y', z']$ is used for the intertial system, and $[x, y, z]$ for the co-rotational system. However, in order to avoid confusion in the current work, the notation shown in figure 2.1 is adopted here as well.

Writing the undisturbed motion of the fluid in the neighbourhood of the particle $[u_0, v_0, w_0]$ as

$$\begin{aligned} u_0 &= \mathtt{a}x' + \mathtt{h}y' + \mathtt{g}z' + \eta z' - \zeta y' \\ v_0 &= \mathtt{h}x' + \mathtt{b}y' + \mathtt{f}z' + \zeta x' - \xi y' \\ w_0 &= \mathtt{g}x' + \mathtt{f}y' + \mathtt{c}z' + \xi y' - \eta x' \end{aligned} \tag{A.2}$$

a,b,c,f,g,h, ξ, η, ζ: components of distortion and rotation of the fluid. These are assumed constant in space, although, as they are referred to the moving particle axes, they are not constant in time.

and using the previously quoted constraint to neglect the non-linear terms, the equation of motion of an incompressible viscous fluid referred to the first co- moving axis of the ellipsoid becomes

$$\mu_g \nabla^2 u - \frac{\partial p}{\partial x'} = \rho_g \left(\frac{\partial u}{\partial t} - \omega_3 v + \omega_2 w \right) \tag{A.3}$$

ω_i: particle rotation about the i'th axis expressed in the co- rotational system

and similarly for the second and third axes.

By applying an order of magnitude consideration once again, equation A.3 can be further reduced to

$$\mu_g \nabla^2 u = \frac{\partial p}{\partial x'}, \quad \mu_g \nabla^2 v = \tfrac{\partial p}{\partial y'}, \quad \mu_g \nabla^2 w = \frac{\partial p}{\partial z'} \tag{A.4}$$

The task now is to solve equation A.4 together with the continuity equation, such that the solution fulfills equation A.2 far from the particle, and on the surface of the ellipsoid gives:

$$u = \omega_2 z' - \omega_3 y', \quad v = \omega_3 x' - \omega_1 z', \quad w = \omega_1 y' - \omega_2 x' \tag{A.5}$$

After considerable mathematical manipulation, Jeffery arrives at very long and complicated expressions for the three velocity components. Rather than reproducing these

here (see Appendix D.1 for the transformation of Jeffery's model to the current formulation using c_1, c_2 and c_3), the hydrodynamic force $\vec{F}$ and torque $\vec{T}$, which produce the motion, are of greater interest. These have been put in a very compact form by Gallily and Cohen (1979):

$$\vec{F} = \mu_g \vec{K} \left[\vec{u}_g + \frac{1}{3!}(D^2\vec{u})_g + \frac{1}{5!}(D^4\vec{u})_g + \frac{1}{7!}(D^6\vec{u})_g \cdots - \vec{u}_p \right] \tag{A.6}$$

$\vec{K} = 16\pi abc \left(\frac{\mathbf{i}'\mathbf{i}'}{\chi_0 + a^2\alpha_0} + \frac{\mathbf{j}'\mathbf{j}'}{\chi_0 + b^2\beta_0} + \frac{\mathbf{k}'\mathbf{k}'}{\chi_0 + c^2\gamma_0} \right)$
$\chi_0 = abc \int_0^\infty \frac{d\lambda'}{\Delta}$
$\alpha_0 = abc \int_0^\infty \frac{d\lambda'}{(a^2+\lambda')\Delta}$
$\beta_0 = abc \int_0^\infty \frac{d\lambda'}{(b^2+\lambda')\Delta}$
$\gamma_0 = abc \int_0^\infty \frac{d\lambda'}{(c^2+\lambda')\Delta}$
$\Delta = [(a^2+\lambda')(b^2+\lambda')(c^2+\lambda')]^{1/2}$
$D^2 = a^2 \frac{\partial^2}{\partial x'^2} + b^2 \frac{\partial^2}{\partial y'^2} + c^2 \frac{\partial^2}{\partial z'^2}$

$$\begin{pmatrix} T_1 \\ T_2 \\ T_3 \end{pmatrix} = \begin{pmatrix} \frac{16\pi\mu_g abc}{3(b^2\beta_0 + c^2\gamma_0)}[(b^2-c^2)f' + (b^2+c^2)(\zeta - \omega_1)] \\ \frac{16\pi\mu_g abc}{3(c^2\gamma_0 + a^2\alpha_0)}[(c^2-a^2)g' + (c^2+a^2)(\eta - \omega_2)] \\ \frac{16\pi\mu_g abc}{3(a^2\alpha_0 + b^2\beta_0)}[(a^2-b^2)h' + (a^2+b^2)(\xi - \omega_3)] \end{pmatrix} \tag{A.7}$$

$f' = \frac{1}{2}\left(\frac{\partial w'}{\partial y'} + \frac{\partial v'}{\partial z'}\right)$
$g' = \frac{1}{2}\left(\frac{\partial u'}{\partial z'} + \frac{\partial w'}{\partial x'}\right)$
$h' = \frac{1}{2}\left(\frac{\partial v'}{\partial x'} + \frac{\partial u'}{\partial y'}\right)$

The work of Jeffery was further extended in the 1960's by H. Brenner[1], who developed models for arbitrary fields of flow, although still under Stokes flow.

A.2 Disks and octahedrons

Haider and Levenspiel (1989) conducted a survey of existing drag correlations and terminal velocity expressions for a number of different shapes including spheres, disks, octahedrons, cube octahedrons, tetrahedrons and cubes.

Faced with the fundamental problem of expressing particles of different shapes using a single parameter, the sphericity is defined:

$$\phi = \frac{A'_s}{A_s} \tag{A.8}$$

[1]Brenner (1964b), Brenner (1964c), Brenner (1964d), Brenner (1964a) and Brenner and Condiff (1972)

A'_s: surface area of a sphere having the same volume as the non- spherical particle $[m^2]$

A_s: surface area of the non-spherical particle $[m^2]$

For particles having the same sphericity less than one, the drag coefficient is expressed as:

$$\begin{aligned} C_D &= \frac{24}{Re_p}[1+\exp(2.3288-6.4581\phi+2.4486\phi^2)Re_P^{(0.0964+0.5565\phi)}] \\ &+ \frac{Re_p \exp(4.905-13.8944\phi+18.4222\phi^2-10.2599\phi^3)}{Re_p+(1.4681+12.2584\phi-20.7322\phi^2+15.8855\phi^3)} \end{aligned} \tag{A.9}$$

For spheres, the drag coefficient becomes:

$$C_D = \frac{24}{Re_p}(1+0.1806Re_p^{0.6459})+\frac{0.4251}{1+\frac{6880.95}{Re_p}} \tag{A.10}$$

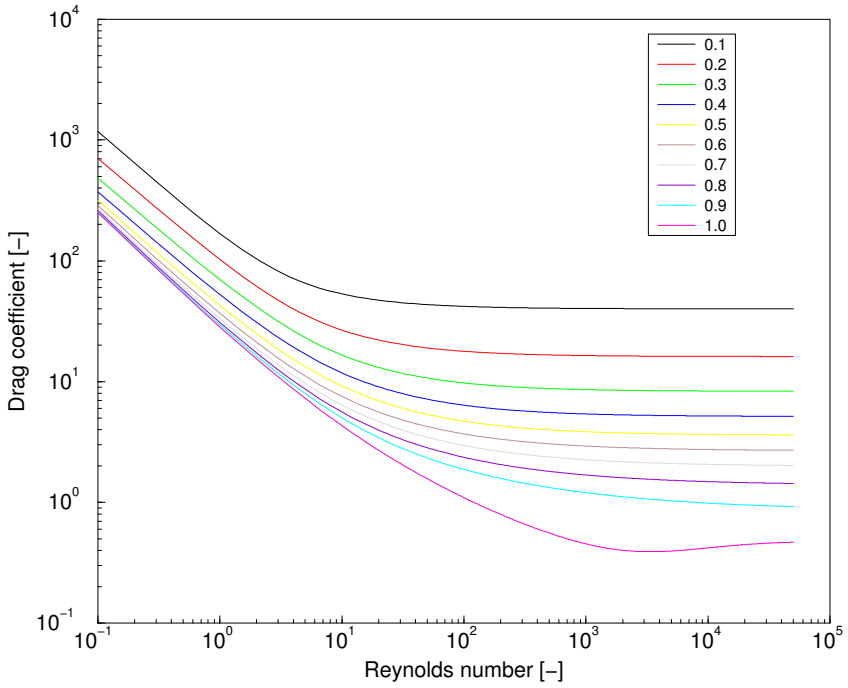

Figure A.1: Drag coefficients for non-spherical particles with sphericities in the range [0.1;1] calculated by equation A.9 and equation A.10 for $\phi = 1$.

A.3 The 2D ellipsoid under general flow conditions

The approach adopted by Besnard and Harlow (1986) is perhaps the most "engineering" of the models described here, and, although some relationships introduced in the work can be questioned, it does indeed form the basis of the model developed in the current work. Essentially, it is a 2D formulation of ellipsoids moving in a pseudo- turbulent flow, based on the same principal formulation as that employed for spheres, deducing, where possible, coefficients from known quantities for spherical particles.

A.3.1 Force definition

The forces formulated are the drag and lift forces. Two regimes are defined, a low velocity regime and a so-called "flow separation" regime for larger velocities. The drag forces in the two regimes are defined quite conventionally:

$$\vec{F}_{D1} = C_{D1}\mu_g V_p^{1/3}(\vec{u}_g - \vec{u}_p) \tag{A.11}$$

$$\vec{F}_{D2} = \frac{1}{2}\rho_g C_{D2} A_p |\vec{u}_g - \vec{u}_p|(\vec{u}_g - \vec{u}_p) \tag{A.12}$$

C_{D1}, C_{D2}: drag coefficients $[-]$
μ_g: fluid molecular viscosity $[kg/ms]$
ρ_g: fluid density $[kg/m^3]$
V_p: particle volume $[m^3]$
A_p: projected particle area $[m^2]$
$\vec{u}_g$: fluid velocity vector $[m/s]$
$\vec{u}_p$: particle velocity vector $[m/s]$

The projected particle area is defined as

$$A_p = \pi a^2(\cos^2\beta + e^2\sin^2\beta)^{1/2} \tag{A.13}$$

e: axes aspect ratio (eccentricity), $\frac{b}{a} \leq 1$ $[-]$

The lift forces consist of a visous circulation-induced lift as well as a flow separation lift. The former is defined as

$$\vec{F}_{L1} = C_{L1}[-sign(\vec{n}\cdot(\vec{u}_g - \vec{u}_p))]\left(\vec{n} \times \frac{\vec{u}_g - \vec{u}_p}{|\vec{u}_g - \vec{u}_p|}\right) \times (\vec{u}_g - \vec{u}_p) \tag{A.14}$$

with

$$C_{L1} = K_{L1}\mu_g(a - b) \tag{A.15}$$

The remaining lift force is based on a modified chord, l_x in figure A.2, describing the horizontal distance between the two separation points on the upper and lower surface

of the particle:

$$\vec{F}_{L2} = C_{L2}[-sign(\vec{n} \cdot (\vec{u}_g - \vec{u}_p))](\vec{n} \times (\vec{u}_g - \vec{u}_p)) \times (\vec{u}_g - \vec{u}_p) \tag{A.16}$$

with

$$C_{L2} = \frac{1}{2} K_{L2} \rho_g l_x a \tag{A.17}$$

l_x is defined as

$$l_x = \frac{a(1-e^2)|\sin^2 \beta|}{B(\beta)} \tag{A.18}$$

$B(\beta)$: geometric variable, $B(\beta) \equiv (e^2 \cos^2 \beta + \sin^2 \beta)$ $[-]$

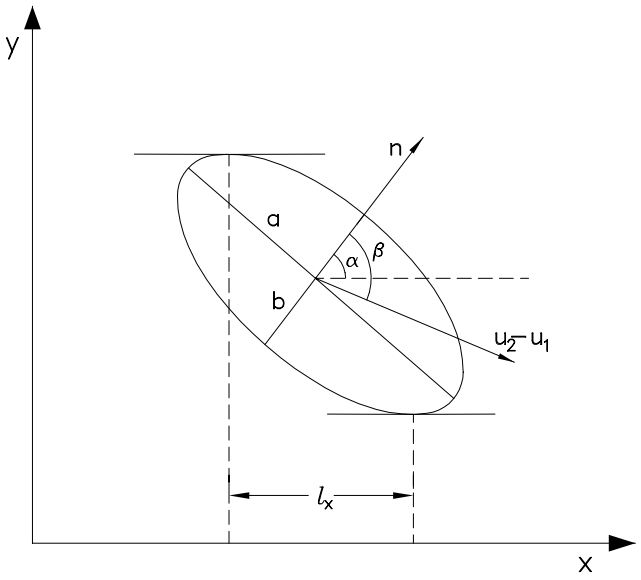

Figure A.2: Schematic of 2D ellipsoid with relevant symbols as defined by Besnard and Harlow (1986).

Including also a pressure gradient force, the full equation of motion becomes

$$\begin{aligned} m_p \frac{d\vec{u}_p}{dt} &= -V_p \vec{\nabla} P + K_{D1} \mu_g V_p^{1/3} (\vec{u}_g - \vec{u}_p) \\ &+ K_{D2} \rho_g A_p |\vec{u}_g - \vec{u}_p| (\vec{u}_g - \vec{u}_p) \\ &+ C_{L1}[-sign(\vec{n} \cdot (\vec{u}_g - \vec{u}_p))] \left(\vec{n} \times \frac{\vec{u}_g - \vec{u}_p}{|\vec{u}_g - \vec{u}_p|} \right) \times (\vec{u}_g - \vec{u}_p) \\ &+ C_{L2}[-sign(\vec{n} \cdot (\vec{u}_g - \vec{u}_p))](\vec{n} \times (\vec{u}_g - \vec{u}_p)) \times (\vec{u}_g - \vec{u}_p) \end{aligned} \tag{A.19}$$

A.3.2 Torque definition

Besnard and Harlow (1986) defines four torque contributors, again based on a viscous and a flow-separation part: viscous and flow-separation damping of the fluid vorticity, and assymmetric repartition of the boundary layer on the surface of the particle.

The first two contributions are given by equations A.20 and A.21:

$$\vec{T_1} = K_{\omega 1}\mu_g V_p \left(\frac{1}{2}\vec{\nabla} \times \vec{u}_g - \omega_p\right) \tag{A.20}$$

$$\vec{T_2} = \frac{1}{2}K_{\omega 2}\rho_g a(a-b)\pi a^2 A(\beta)|\vec{u}_g - \vec{u}_p| \left(\frac{1}{2}\vec{\nabla} \times \vec{u}_g - \omega_p\right) \tag{A.21}$$

$A(\beta)$: geometric variable, $A(\beta) \equiv (\cos^2\beta + e^2 \sin^2\beta)$ $[-]$

The boundary layer generated torques are given by equations A.22 and A.23:

$$\vec{T_3} = -K_{\omega 3}\mu_g b(a-b) \left(\vec{n} \cdot \frac{\vec{u}_g - \vec{u}_p}{|\vec{u}_g - \vec{u}_p|}\right) [\vec{n} \times (\vec{u}_g - \vec{u}_p)] \tag{A.22}$$

$$\vec{T_4} = \frac{1}{2}K_{\omega 4}\rho_g(a-b)\pi a^2 [\vec{n} \cdot (\vec{u}_g - \vec{u}_p)][\vec{n} \times (\vec{u}_g - \vec{u}_p)] \tag{A.23}$$

Appendix B

Simulation methodology

In the following sections, the numerical implementations of the physical models of the particle aerodynamics and combustion are described. The numerical code is termed PCOMBUST , and has been written entirely in Fortran 77 using several different IBM RS/6000 and CRAY platforms (table B.1).

Machine	Architecture	Location[a]	Memory
IBM 25T	RISC/6000	IET	64MB RAM
IBM 560	RISC/6000	IET	256MB RAM
IBM SP	RISC/6000	IET	2 × 256MB RAM
IBM SP	RISC/6000	UNIC	2 × 1-2GB RAM
CRAY-92A	Vector	UNIC	2.0GB RAM

[a]IET: Institute of Energy Technology, Aalborg University
UNIC: UNI-C, Danish National Computing Centre

Table B.1: Platforms and configurations.

PCOMBUST is designed to be a stand-alone code, obtaining it's CFD basis from an arbitraty external code, and returning particle source terms through a generic file format. During the development of PCOMBUST , CFX4 from AEA Technology plc has been used to provide the CFD basis, and in the following, users of CFX4 will no doubt find familiar terms and variable naming conventions.

B.1 Particle area and volume

The superelliptic equation (equation 2.14) belongs to the class of elliptic equations, which share the feature that they cannot be integrated analytically. This means that suitable numerical methods - in terms of speed, stability and accuracy - have to be employed to determine surface are, projected area and volume. For all these quantities, Romberg integration is used (Press et al. 1992). This method is a complex numerical

integration method, which is based on an extension of the trapezoidal rule:

$$\int_{x_1}^{x_N} f(x)dx = h\left[\frac{1}{2}f_1 + f_2 + \cdots + f_{N-1} + \frac{1}{2}f_N\right] + O\left(\frac{(b-a)^3 f''}{N^2}\right) \tag{B.1}$$

h: integration step size

f_i: function value at x_i

a, b: lower and upper endpoint for the integration

N: number of integration intervals

O: error term

By using equation B.1 with successive step size refinements k times, all terms in the error series up to $O\left(\frac{1}{N^{2k}}\right)$ are removed, and then the integral is extrapolated to the limit of $h = 0$, obtaining a value very close to the analytical. At the same time, the number of integral evaluations neccessary for convergence can be substantially less than using the trapezoidal rule alone, provided the integral is "smooth" and contains no singularities. The implementation in PCOMBUST uses $k = 5$ refinements, before extrapolation begins.

In order to perform the extrapolation in a responsible manner, Neville's algorithm (Press et al. 1992) is used. Neville's algorithm is based on an extension of Lagrange's extrapolation formula, where the extrapolation polynomial is constructed from a series of polynomials from order 0 to N-1, which relate the extrapolation points to function values. This method is described in detail in Press et al. (1992). One point to be made, though, is that Neville's algorithm also provides an error estimate, making the algorithm less susceptible to misuse.

Numerical integration is only performed on one quarter of the particle surface for each quantity, in order to speed up the calculation. For exponents greater than 20, a correction factor for the end surfaces is added to the integral.

For the combustion calculations, the mean diameter based on surface area is determined. The equivalent diameter is simply:

$$\bar{d}_p = \sqrt{\frac{A_s}{\pi}} \tag{B.2}$$

A_s: superelliptical particle surface area, determined by Romberg integration $[m^2]$

During combustion calculations, Romberg integration, due to its relatively large time consumption, is only employed to determine the volume once when the particle is initialized. After that, the combustion processes cause changes to the minor axis dimension (or particle diameter), which is then used to determine the volume of the particle at the end of each time step. This is done by assuming that the particle retains it shape, such that β and n are constant, and only the axes change. This then leaves only one variable, the minor axis dimension, which is shown in figure B.1 as a function of the

particle volume for a number of aspect ratios and superelliptic exponents. Romberg integration is then used to determine surface and projected areas, as normal.

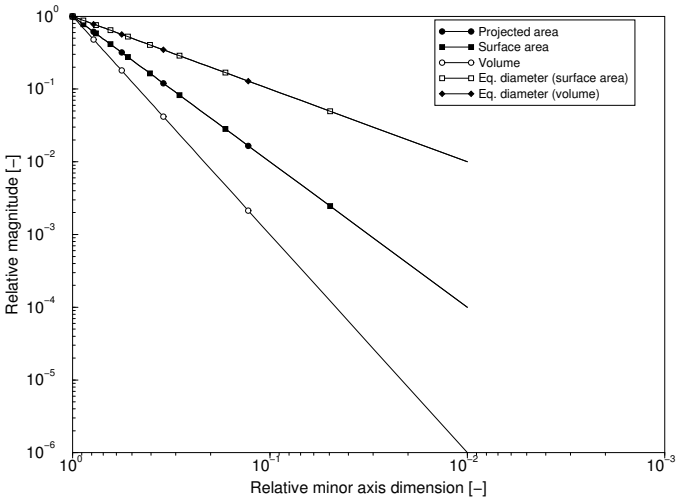

Figure B.1: Relative volume ($\frac{V}{V_0}$) and areas ($\frac{A}{A_0}$) as functions of the relative minor axis size ($\frac{a}{a_0}$). Equivalent spherical diameters based on surface area (eq. 3.4) and volume are also shown.

B.2 Coordinate systems

There are three types of coordinates systems in PCOMBUST, one global Cartesian (xyz), one local (rst), and one topological (IJK) set of coordinates. The latter is the framework of the entire programme, and will always be used, regardless of the global coordinate system used.

The default mapping convention between the global systems and the local and topological systems, respectively, is that first coordinates map to first coordinates, second to second and third to third.

It is important to understand, that PCOMBUST always works in physical coordinates, and no transformation to computational space takes place (see for example Anderson (1985)). This neccessitates special treatment of flow variables, as described in section B.2.3, with well-defined relationships between the different coordinate systems.

B.2.1 Cartesian coordinates

When Cartesian coordinates are used, all global coordinates are specified in this system. Thus, all cell vertices and centres are expressed in terms of their x, y and z locations,

assuming these vertices to be connected by straight lines[1]. This information is also used to calculate inlet areas, as well as to express the trajectories of particles in the domain.

Particle trajectories and velocities are always expressed in global coordinates.

B.2.2 The topological coordinate system

The topological coordinate system is used within PCOMBUST to index the four-dimensional arrays in which the coordinates and flow variables are stored. It is also used to define the locations of all patches such as inlets, outlets, block glue patches. During the tracking of a particle, the topological coordinates are stored in order to determine which set of cell vertex coordinates to use for the interpolation of flow variables to the particle position (see section B.4).

B.2.3 Local coordinates

The local coordinate system is defined within each individual cell, as shown in figure B.2, each coordinate in the range $[0; 1]$. This coordinate system is used for two purposes: the first is to interpolate all flow variables to the cell vertices at the beginning of a simulation, and then to interpolate these variables to the particle position during a simulation, in order to determine the transfer processes there.

In the following, a two dimensional system will be used for clarity. However, it is not difficult to extend the method to the third dimension.

As the global coordinate system is a physical system, the cells defined therein are not neccessarily rectangular. In order to uniquely determine the position of a particle in terms of the local coordinates at a given time within a cell in the local coordinate system, a bi-linear relationship is established between the global position vector of the particle, $\vec{x}_p$ and the global coordinates of the cell vertices, where the local coordinates are the transformation factors:

$$\begin{aligned} \vec{x}_p &= \vec{h}_1\ (1-r)(1-s) \\ &= \vec{h}_2\ r(1-s) \\ &= \vec{h}_3\ (1-r)s \\ &= \vec{h}_4\ \ rs \end{aligned} \tag{B.3}$$

$\vec{h}_i$: global coordinate vector to vertex i $[m]$

[1]This is no different from the assumption when transforming a boundary fitted grid from physical to computational space in a standard finite volume flow solver

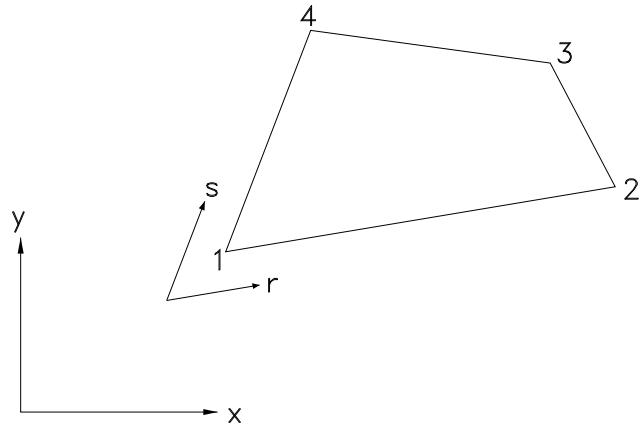

Figure B.2: Two dimensional representation of the relationship between global cartesian and local coordinates. The third coordinate, t, would be perpendicular to the plane of the paper.

As long as the local coordinates remain in the range $[0; 1]$, the particle is inside the cell. If, however, the local coordinates fall outside this range, the particle is not inside the cell, and the value of each local coordinate will signify the direction in which the cell with the particle is located, according to figure B.3 (Rusaas 1995).

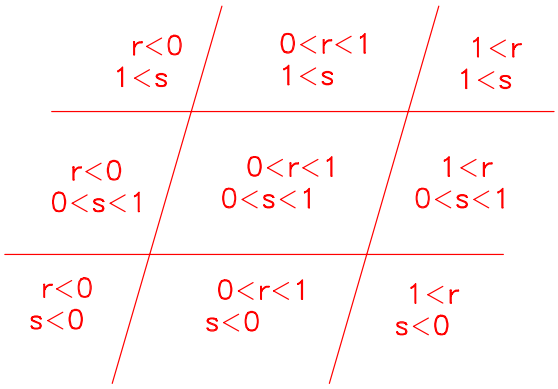

Figure B.3: The range of values of the local coordinates.

B.3 Domain topology

The domain topology is the information PCOMBUST uses to define the domain, and consists of patch types and locations. This information is given in terms of the topological coordinate system and two further variables, the `nwall` and `iblank` variables.

B.3.1 Patches

Patches are two-dimensional surfaces, located at the borders of the topology, which instruct PCOMBUST that this area is to be treated in a special manner.

When PCOMBUST defines the domain in terms of topological coordinates, it initially assumes that all cells are flow domain cells. It then proceeds to define a row of cells around each side of each block, the "dummy" cells[2].

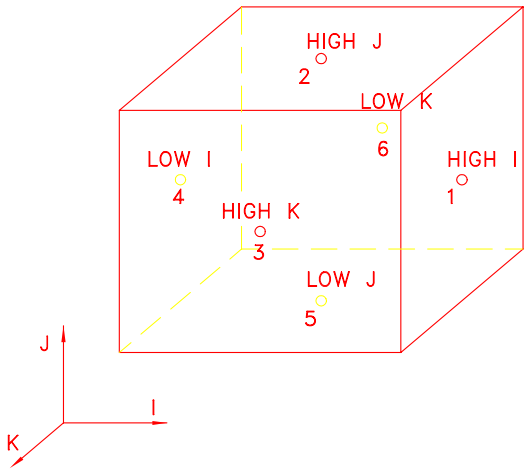

Figure B.4: The value of `nwall` defines the side of the cell on which the patch is located.

Finally, the patches are applied in the appropriate locations to change the cell types there. Due to the two-dimensional nature of a patch, it is applied on the side of a cell, governed by the value of `nwall` (see figure B.4). As such two-dimensional structures do not exist in PCOMBUST , the type of patch is applied to the neighbouring dummy cells, as shown in figure B.5. The type of patch is governed by the value of `iblank`, which identifies each individual cell in the domain by type (see table B.2)

B.4 Flow variable interpolation

As previously mentioned, all flow variables are interpolated to the particle position during tracking and, if defined, combustion. Another approach would be to use cell-centred values for the duration of a particles residence within a given cell, and, upon crossing to the neighbour cell, from one step to another, use these new cell-centred values. However, this is not a desirable approach, as these discontinuities make themselves

[2]These are also referred to as "ghost", or "dead" cells; they are a fundamental part of the computational domain used by virtually all finite-volume based CFD programmes. However, not all CFD programmes include the dummy cells when they write a grid file.

Iblank value	Patch name	Cell type
0	-	Flow cell
1	WALL	Solid cell
2	INLET	Fluid inlet
3	PARTOUT	Particle outlet
4	-	-
5	SYMMET	Symmetry cells
6	PARTIN	Particle inlet
7	OUTLET	Fluid outlet
8	PRESS	Pressure boundary cell
9	BLKBDY	Block-to-block glue cell

Table B.2: Values of `iblank` and corresponding patch names and cell types

very clear in the results, particularly when considering combustion.

The unknowns of the interpolation are the local coordinates; once they are determined from the known global position of the particle, they are used as a weighting function to determine the flow variables.

For the interpolation, equation B.4 is rewritten to form functions of the local coordinate which can be subjected to a root-finding routine (shown here for the two-dimensional case):

$$\begin{aligned} f_1(r,s) &= x_1(1-r)(1-s) + x_2 r(1-s) + x_3(1-r)s + x_4 rs - x_p \\ f_2(r,s) &= y_1(1-r)(1-s) + y_2 r(1-s) + y_3(1-r)s + y_4 rs - y_p \end{aligned} \tag{B.4}$$

x_i: first global coordinate of vertex i $[m]$

y_i: second global coordinate of vertex i $[m]$

x_p, y_p: first and second coordinates of the particle position vector $[m]$

Although these equations are analytically solveable, the resulting expressions, particularly in three dimensions, become very complex. Instead, a suitable numerical root finding algorithm can be utilized. In PCOMBUST, this algorithm is the Newton-Raphson method for multi-dimensional systems, chosen due to its stability and quadratic convergence rate, once near a root (Press et al. 1992), (Paulsen and Holst 1993). This will always be the case, as the change in position from one time step to the next is small.

The Newton-Raphson algorithm is based on a Taylor-series expansion of each of the functions to be zeroed:

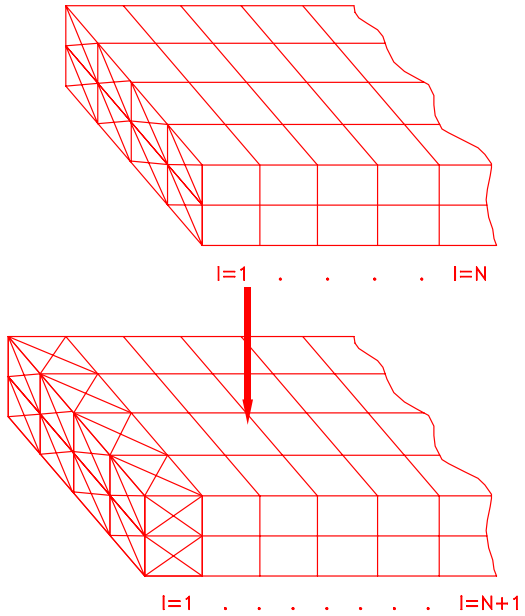

Figure B.5: The conversion of a 2D patch to 3D dummy cells.

$$f_i(\vec{z}+\delta\vec{z}) = f_i(\vec{z}) + \sum_{j=1}^{N} \frac{\partial f_i}{\partial z_j}\delta z_j + O(\delta\vec{z}^2) \tag{B.5}$$

$\vec{z}$: local coordinate vector $[m]$
N: number of coordinates $[-]$

Truncating all second and higher order terms, and identifying the first term in the summation as the Jacobian matrix, a linear set of equations for the correction $\delta\vec{z}$ which cause the functions f_i to go to zero simultaneously can be written:

$$\sum_{j=1}^{N} J_{ij}\delta z_j = -f_i \tag{B.6}$$

J_{ij}: terms in the Jacobian matriz $=\frac{\partial f_i}{\partial z_j}$

Equation B.6 can be solved using Cramers rule, yielding the new local coordinate vector when $f_i = 0$:

$$\vec{z} = \vec{z}_{old} + \delta\vec{z} \tag{B.7}$$

B.5 Adaptive time stepping

Within PCOMUST, the equations of motion (2.1) and (2.2- 2.4), which are of the same type, are recast in the form (B.8) (see appendix C). By assuming constant flow velocity and aerodynamic response time (equation 2.18), semi-analytic integration is performed to yield equation B.9:

$$f'(t) = c_1(f(t) - c_2) + c_3 \tag{B.8}$$

$$f(t) = c_2 + (f(t_0) - c_2)exp(c_1\Delta t) - \frac{c_3}{c_1}(1 - exp(c_1\Delta t)) \tag{B.9}$$

$f'(t)$: particle translational or angular acceleration

$f(t)$: particle translational or rotational velocity

t: current time

t_0: time of previous determination

Δt: time step

$-c_1$: the reciprocal of the aerodynamic response times for translation and rotation

c_2: term containing fluid velocity for translational motion and fluid vorticity for rotation

c_3: term containing conservative contributions

In order that the semi-analytical integration used does not cause unacceptable errors, the time step must be very small, in order for the assumptions to be valid. At the same time, very small time steps is computationally expensive, and therefore undesirable. Therefore, it is attractive to use some form of time step regulation to achieve the smallest time step without causing errors which are greater than a predetermined criterion. Two different approaches to time step regulation are relative time step control (Astrup and Gjernes 1988) and adaptive time step control (Rusaas 1995).

Relative time stepping controls the time step according to the particle velocity and cell dimensions, using the Jacobian matrix of the cell vertices:

$$\Delta t \leq f_{dim}\frac{|Ja|^2}{Ja\vec{u}_p} \tag{B.10}$$

Ja: Jacobian matrix of the cell

f_{dim}: parameter governing the number of time steps in a single cell

$\vec{u}_p$: particle velocity

One fundamental problem with this approach is the exclusion of fluid velocities, in particular fluid velocity gradients, in the determination of the timestep. If the particle velocity is small, the time step becomes large; if the particle is in an area with large velocity gradients, the integration error will become unacceptable.

Instead, PCOMBUST uses the adaptive time step method, where the time step is adjusted according to an estimate of the truncation error. This is done by carrying out each calculation step twice - first taking the entire time step, and then taking it again in two half steps (figure B.6). The difference δ between the two final velocities is

evaluated, and related to the velocity of the particle after the time step, if the values from the previous time step had been used, to determine the relative error:

$$\varepsilon = \frac{\delta}{|\vec{u}_p| + |\vec{a}_p dt|} \tag{B.11}$$

$\vec{u}_p$: particle velocity of the previous time step $[m/s]$

$\vec{a}_p$: particle acceleration of the previous time step $[m/s^2]$

dt: time step being evaluated $[s]$

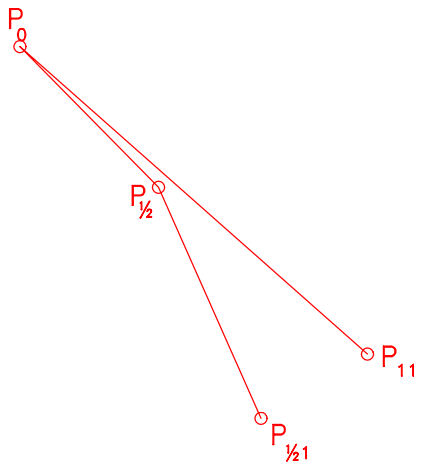

Figure B.6: The principle of adaptive time stepping: taking first one long step, then two half-steps, and evaluating the difference.

The time step is successively reduced, until ε falls below a preset error criterion. This is in PCOMBUST set to 5.0×10^{-4}, and is normally in the range $[5.0 \times 10^{-6}; 5.0 \times 10^{-3}]$ (Rusaas 1995). Further, an initial assumption that the new time step is four times that of the previous has been shown to give very fast convergence.

B.6 Wall collisions

Wall collisions are detected when a particle has crossed into a cell with an `iblank` value of 1. In this case, the normal time stepping is disabled, and the time step needed from the previous position to the point of impact with the wall is determined. Due the the non-linearity in the equation of motion, this is done iteratively, using the powerful Van Wijngaarden-Dekker-Brent algorithm of root finding (Press et al. 1992), which combines root bracketing, bisection and inverse quadratic interpolation.

The interval for the search is that from $dt = 0$, i.e. at the position before the time step, to the time step determined from the normal adaptive time step determination. As the

particle has crossed into a wall cell, the time step needed to reach the point of impact is certain to be within these two limits. If this is the case, the method guarantees at least linear convergence, but in practice convergence is reached at much higher rates.

Once the point of impact has been determined, the resulting velocities after the collision according to Grant and Tabakoff (1975) must be determined. This is done by determining a number of vectors, which describe the impact plane (see figure B.7):

$$\vec{n}_t = \vec{u}_{ip} \times \vec{n}_w \tag{B.12}$$

$\vec{n}_t$: vector normal to the plane of impact $[m]$

$\vec{n}_w$: vector normal to the wall, determined from the plane defined by the face of the cell $[m]$

$\vec{u}_{ip}$: impact, or incidence, velocity $[m/s]$

$$\vec{T} = \vec{n}_t \times \vec{n}_w \tag{B.13}$$

$\vec{T}$: vector in the plane of impact, tangent to the wall $[m]$

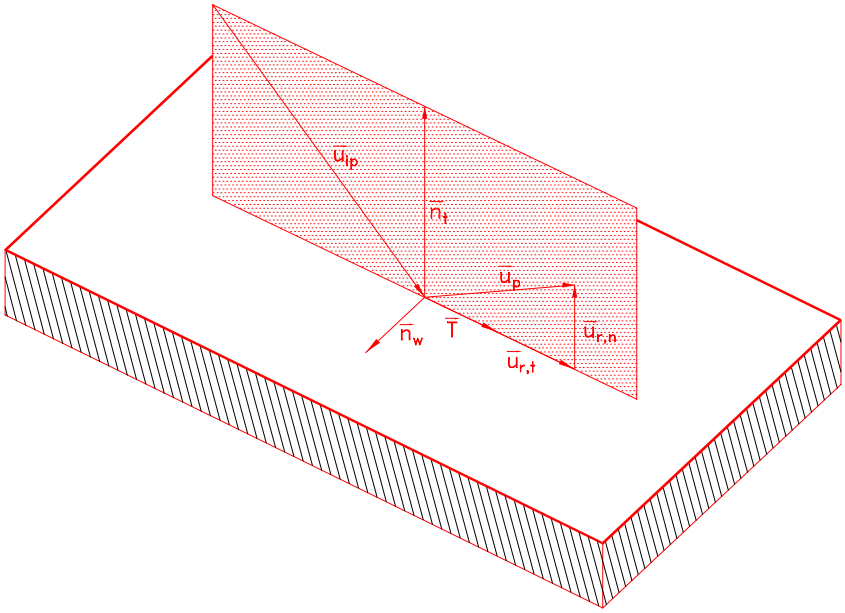

Figure B.7: The planes of impact and the vectors which define them.

With these vectors, the resulting velocities normal and tangential to the wall in the plane of impact can be determined:

$$\vec{u}_{r,n} = \frac{\vec{n}_w}{|\vec{n}_w|} u_{r,n} \tag{B.14}$$

$$\vec{u}_{r,t} = \frac{\vec{T}}{|\vec{T}|} u_{r,t} \tag{B.15}$$

$u_{r,n}$: resulting normal speed (equation B.16) $[m/s]$

$u_{r,t}$: resulting tangential speed (equation B.17) $[m/s]$

$$\frac{u_{r,n}}{u_{i,n}} = 0.993 - 1.76\beta_i - 1.56\beta_i^2 - 0.49\beta_i^3 \tag{B.16}$$

$$\frac{u_{r,t}}{u_{i,t}} = 0.988 - 1.66\beta_i + 2.11\beta_i^2 - 0.67\beta_i^3 \tag{B.17}$$

β_i: Impact angle $[rad]$

Finally, by vector addition, the particle velocity after the collision:

$$\vec{u}_p = \vec{u}_{r,n} + \vec{u}_{r,t} \tag{B.18}$$

Although possibly a major factor, the angular velocity of the particle (tumbling motion) is not included in the wall collision model.

B.7 Calculating particle temperature

The heat balance (equation 3.36) can be reformulated in the same manner as the equation of motion, yielding an equation of the same form as equation B.8. Thus, using similar assumptions (constant Nu and gas temperature during a time step), the resulting equation can be integrated to the form of equation (B.9), giving an expression for the instantaneous particle temperature:

$$T_p = c_2 + (T_{p,0} - c_2)\exp(c_1 \Delta t) - \frac{c_3}{c_1}(1 - \exp(c_1 \Delta t)) \tag{B.19}$$

Δt: time step $[s]$

$T_{p,0}$: particle temperature at the end of the previous time step $[K]$

c_1: temperature time constant $[s^{-1}]$, given by:

$$c_1 = -\frac{Nu A_s \lambda}{\bar{d}_p m_p c_{pp}} \tag{B.20}$$

c_2: gas temperature $[K]$

c_3: heat sources and sinks $[K/s]$:

$$c_3 = \frac{1}{m_p c_{pp}} \left(\frac{dm_v}{dt} h_{fg} + \frac{dm_c}{dt} z_{pg} H_{reac} \right) \tag{B.21}$$

m_p: particle mass $[kg]$

c_{pp}: particle heat capacity (equation (3.39) $[J/kgK]$

Nu: Nusselt number as given be either equation (3.29) or (3.30) $[-]$

λ: convective heat transfer coefficient $[W/m^2K]$

A_s: particle surface area $[m^2]$

$\frac{dm_v}{dt}$: rate of volatiles release $[kg/s]$

$\frac{dm_c}{dt}$: rate of fixed char release $[kg/s]$

h_{fg}: latent heat of the volatiles $[J/kg]$

H_{reac}: heat of reaction of the char+oxygen reaction $[J/kg]$

z_{pg}: fraction of heat of reaction to remain in particle $[-]$

B.8 Particle ignition - initial combustion calculations

In order to start a simulation of heat and mass transfer, the transfer processes must be initiated in some way, as the first flow solution will not have the heat and mass sources needed to build up a temperature field, upon which the transfer rates will depend. The simplest way to initiate the transfer processes, is to artificially scale the temperature of the gas phase, such that the particles experience steep temperature gradients upon entry into the domain, and the transfer processes are started. Thus, the artificial temperature is simply

$$T'_g = \alpha_T T_g \tag{B.22}$$

with α_T suitably chosen. Of course, this should only be employed in the first (or first few, depending on the underrelaxation employed) particle calculation; after that, the combustion should be able to sustain itself.

Appendix C

Integrating the equations of motion

In the majority of papers dealing with Langrangian particle motion, the equations of motion have been integrated numerically, typically using a 4th. order Runge- Kutta or Adams-Bashforth method. This entails several operations for each determination of the particle velocity, and, in complex numerical codes, this can cause undesirably long calculation times.

Rather than employing a numerical integration scheme, the equations of motion can be integrated semi-analytically once and for all, by assuming constant gas velocity and particle response time (i.e. a constant Stokes number) in one time step. This assumption does not differ from those necessary in the numerical schemes.

C.1 Translation and rotation

The differential equations of motion generally take the form

$$f'(\xi) = c_1(f(\xi) - c_2) + c_3 \tag{C.1}$$

$f(\xi)$: $\vec{v}_p$ or $\vec{\omega}_p$
c_1,c_2,c_3: constants in the time step

In the case of $c_3 = 0$, there is an analytical solution

$$f(\xi) = c_2 + C \exp c_1 t \tag{C.2}$$

C: constant of integration

In order to solve the case of $c_3 \neq 0$, C is transformed into a function of time, such that

$$C(t) = \frac{f(\xi) - c_2}{\exp c_1 t} \tag{C.3}$$

Replacing C by $C(t)$ in C.2 and differentiating with respect to time yields

$$\frac{df(\xi)}{dt} = \frac{d\left(C(t)\exp c_1 t\right)}{dt} = c_1(f(\xi) - c_2) + c_3 \tag{C.4}$$

Writing C.4 out in full:

$$\frac{d\left(C(t)\exp c_1 t\right)}{dt} = \frac{dC(t)}{dt}\exp c_1 t + C(t)c_1 \exp c_1 t = c_1(f(\xi) - c_2) + c_3 \tag{C.5}$$

Re-introducing the definition of $C(t)$ from C.3 in C.5 yields

$$\frac{dC(t)}{dt} = c_3 \exp\left(-c_1 t\right) \tag{C.6}$$

and C(t) can be written as

$$C(t) = \frac{c_3}{-c_1}\exp\left(-c_1 t\right) + C_2 \tag{C.7}$$

C_2: constant of integration

The expression for $f(\xi)$ now becomes

$$f(\xi) = c_2 + \left(\frac{c_3}{-c_1}\exp\left(-c_1 t\right) + C_2\right)\exp c_1 t \tag{C.8}$$

It only remains now to determine the value of C_2. This is done using the initial conditions $f(\xi_0)$ and $F(\xi_0)$, where $F(\xi) = \int f(\xi)dt$:

$$C_2 = f(\xi_0) - c_2 + \frac{c_3}{c_1} \tag{C.9}$$

Inserting this into C.8 yields the final expression:

$$f(\xi) = c_2 + \left(\frac{c_3}{-c_1}\exp\left(-c_1 t\right) + (f(\xi_0) - c_2 + \frac{c_3}{c_1})\right)\exp c_1 t \tag{C.10}$$

and written in a more logical form

$$f(\xi) = c_2 + \left(f(\xi_0) - c_2\right)\exp c_1 t - \frac{c_3}{c_1}\left(1 - \exp c_1 t\right) \tag{C.11}$$

C.11 thus represents a template for the final form of the equations of motion of arbitrary particles, as well as arbitrary forms of motion. The task that remains is a definition of the forces or torques, which cause the motion (i.e. c_1, c_2 and c_3). Once defined, they can be readily inserted into the integrated equation.

C.2 Position and orientation

Continuing the line of logic above, it is a small effort to integrate C.11 once more, to obtain the position and orientation of the particle, rather than rely on the mean value of velocity during two timesteps. Using the same symbols as above, the equation for position and particle orientation becomes

$$F(\xi) = F(\xi_0) + c_2 t - \frac{1}{c_1}(f(\xi_0) - c_2)[1 - \exp(c_1 t)] - \frac{c_3}{c_1}\left[t - \frac{1}{c_1}\left(1 - \exp(c_1 t)\right)\right] \quad \text{(C.12)}$$

Appendix D

c_i for different models of motion

D.1 Ellipsoid

Shape used by (Jeffery 1922), (Brenner 1964d), (Fan and Ahmadi 1995) amongst others. Limited to Stokes regime.

Translation

$$c_1 = -\frac{\mu_g}{m_p}\underline{\underline{K}}' \tag{D.1}$$

$$c_2 = \vec{u}_g \tag{D.2}$$

$$c_3 = \frac{\mu_g}{6m_p}\underline{\underline{A}}^{-1} \cdot \underline{\underline{K}} D^2\vec{u} \tag{D.3}$$

Rotation about x' axis

$$c_1 = \frac{-16\pi\mu a^3\beta}{3I_{x'}(\beta^2\beta_0 + \alpha_0)}(\beta^2 + 1) \tag{D.4}$$

$$c_2 = \frac{1}{2}\left(\frac{\partial w}{\partial y} - \frac{\partial v}{\partial z}\right) \tag{D.5}$$

$$c_3 = \frac{\omega_{y',0}\omega_{z',0}}{I_{x'}}(I_{y'} - I_{z'}) + \frac{16\pi\mu a^3\beta}{3I_{x'}(\beta^2\beta_0 + \alpha_0)}(\beta^2 - 1)\left[\frac{1}{2}\left(\frac{\partial w}{\partial y} + \frac{\partial v}{\partial z}\right)\right] \tag{D.6}$$

Rotation about y' axis

$$c_1 = \frac{-16\pi\mu a^3\beta}{3I_{y'}\alpha_0} \tag{D.7}$$

$$c_2 = \frac{1}{2}\left(\frac{\partial u}{\partial z} - \frac{\partial w}{\partial x}\right) \tag{D.8}$$

$$c_3 = 0 \tag{D.9}$$

Rotation about z' axis

$$c_1 = \frac{-16\pi\mu a^3\beta}{3I_{z'}(\alpha_0 + \beta^2\beta_0)}(\beta^2 + 1) \tag{D.10}$$

$$c_2 = \frac{1}{2}\left(\frac{\partial v}{\partial x} - \frac{\partial u}{\partial y}\right) \tag{D.11}$$

$$c_3 = \frac{\omega_{x',0}\omega_{y',0}}{I_{z'}}(I_{x'} - I_{y'}) + \frac{16\pi\mu a^3\beta}{3I_{z'}(\alpha_0 + \beta^2\beta_0)}(1 - \beta^2)\left[\frac{1}{2}\left(\frac{\partial v}{\partial x} + \frac{\partial u}{\partial y}\right)\right] \tag{D.12}$$

with parameters β, $D^2\vec{u}_g$, $\underline{\underline{K}}$, $\underline{\underline{K'}}$, α_0 and β_0 defined as follows:

$$\beta = \frac{b}{a} \tag{D.13}$$

$$D^2\vec{u}_g = a^2\frac{\partial \vec{u}_g}{\partial x^2} + b^2\frac{\partial \vec{u}_g}{\partial y^2} + a^2\frac{\partial \vec{u}_g}{\partial z^2} \tag{D.14}$$

$$\underline{\underline{K}} = \begin{bmatrix} \frac{16\pi a(\beta^2-1)}{\frac{2\beta^2-3}{\sqrt{\beta^2-1}}\ln(\beta+\sqrt{\beta^2-1})+\beta} & 0 & 0 \\ 0 & \frac{8\pi a(\beta^2-1)}{\frac{2\beta^2-1}{\sqrt{\beta^2-1}}\ln(\beta+\sqrt{\beta^2-1})-\beta} & 0 \\ 0 & 0 & \frac{16\pi a(\beta^2-1)}{\frac{2\beta^2-3}{\sqrt{\beta^2-1}}\ln(\beta+\sqrt{\beta^2-1})+\beta} \end{bmatrix} \tag{D.15}$$

$$\underline{\underline{K'}} = \underline{\underline{A}}^{-1} \cdot \underline{\underline{K}} \cdot \underline{\underline{A}} \tag{D.16}$$

$$\alpha_0 = \frac{b^2}{b^2 - a^2} + \frac{a^2 b}{2(b^2 - a^2)^{3/2}}\ln\left[\frac{b - \sqrt{b^2 - a^2}}{b + \sqrt{b^2 - a^2}}\right] \tag{D.17}$$

$$\beta_0 = -\frac{2a^2}{b^2 - a^2} - \frac{a^2 b}{(b^2 - a^2)^{3/2}}\ln\left[\frac{b - \sqrt{b^2 - a^2}}{b + \sqrt{b^2 - a^2}}\right] \tag{D.18}$$

Translation and rotation

$$\vec{v}_p(t) = \vec{u}_g + (\vec{v}_{p,0} - \vec{u}_g)\exp(-\frac{\mu}{m_p}\underline{\underline{K}}'t) + \frac{\underline{\underline{A}}^{-1} \cdot \underline{\underline{K}} D^2\vec{u}_g}{6\underline{\underline{K'}}}\left(1 - \exp(-\frac{\mu}{m_p}\underline{\underline{K}}'t)\right) \tag{D.19}$$

$$\begin{aligned}\omega_{x'}(t) &= \frac{1}{2}\left(\frac{\partial w}{\partial y}-\frac{\partial v}{\partial z}\right)+\left(\omega_{x',0}-\frac{1}{2}\left(\frac{\partial w}{\partial y}-\frac{\partial v}{\partial z}\right)\right)\exp\left[-\frac{16\pi\mu a^3\beta(\beta^2+1)}{3I_{x'}(\beta^2\beta_0+\alpha_0)}t\right]\\ &- \left(-\frac{3\omega_{y',0}\omega_{z',0}(I_{y'}-I_{z'})(\beta^2\beta_0+\alpha_0)}{16\pi\mu a^3\beta(\beta^2+1)}-\frac{\beta^2-1}{\beta^2+1}\left[\frac{1}{2}\left(\frac{\partial w}{\partial y}+\frac{\partial v}{\partial z}\right)\right]\right)\\ &\left(1-\exp\left[-\frac{16\pi\mu a^3\beta(\beta^2+1)}{3I_{x'}(\beta^2\beta_0+\alpha_0)}t\right]\right) \qquad \text{(D.20)}\end{aligned}$$

$$\omega_{y'}(t)=\frac{1}{2}\left(\frac{\partial u}{\partial z}-\frac{\partial w}{\partial x}\right)+\left(\omega_{y',0}-\frac{1}{2}\left(\frac{\partial u}{\partial z}-\frac{\partial w}{\partial x}\right)\right)\left(1-\exp\left[-\frac{16\pi\mu a^3\beta}{3I_{y'}\alpha_0}t\right]\right) \qquad \text{(D.21)}$$

$$\begin{aligned}\omega_{z'}(t) &= \frac{1}{2}\left(\frac{\partial v}{\partial x}-\frac{\partial u}{\partial y}\right)+\left(\omega_{z',0}-\frac{1}{2}\left(\frac{\partial v}{\partial x}-\frac{\partial u}{\partial y}\right)\right)\exp\left[-\frac{16\pi\mu a^3\beta(\beta^2+1)}{3I_{z'}(\beta^2\beta_0+\alpha_0)}t\right]\\ &- \left(-\frac{3\omega_{y',0}\omega_{z',0}(I_{y'}-I_{x'})(\beta^2\beta_0+\alpha_0)}{16\pi\mu a^3\beta(\beta^2+1)}-\frac{1-\beta^2}{\beta^2+1}\left[\frac{1}{2}\left(\frac{\partial v}{\partial x}+\frac{\partial u}{\partial y}\right)\right]\right)\\ &\left(1-\exp\left[-\frac{16\pi\mu a^3\beta(\beta^2+1)}{3I_{z'}(\beta^2\beta_0+\alpha_0)}t\right]\right) \qquad \text{(D.22)}\end{aligned}$$

Position and orientation

$$\begin{aligned}\vec{x}_p(t) &= \vec{x}_{p,0}+\vec{u}_g t+\frac{m_p}{\mu\underline{\underline{K}}'}(\vec{v}_{p,0}-\vec{u}_g)\left[1-\exp\left(\frac{\mu}{m_p}\underline{\underline{K}}'t\right)\right]\\ &+ \frac{\underline{\underline{A}}^{-1}\underline{\underline{K}}D^2\vec{u}_g}{6\underline{\underline{K}}'}\left[t+\frac{m_p}{\mu\underline{\underline{K}}'}\left(1+\exp\left(-\frac{\mu}{m_p}\underline{\underline{K}}'t\right)\right)\right] \qquad \text{(D.23)}\end{aligned}$$

$$\begin{aligned}\theta_{x'}(t) &= \theta_{x',0}+\frac{1}{2}\left(\frac{\partial w}{\partial y}-\frac{\partial v}{\partial z}\right)t+\left[\frac{3I_{x'}(\beta^2\beta_0+\alpha_0)}{16\pi\mu a^3\beta}(\beta^2+1)\right]\left(\omega_{x',0}-\frac{1}{2}\left(\frac{\partial w}{\partial y}-\frac{\partial v}{\partial z}\right)\right)\\ &\left(1-\exp\left(\frac{-16\pi\mu a^3\beta}{3I_{x'}(\beta^2\beta_0+\alpha_0)}(\beta^2+1)t\right)\right)\\ &- \left(-\frac{3\omega_{y',0}\omega_{z',0}(I_{y'}-I_{z'})(\beta^2\beta_0+\alpha_0)}{16\pi\mu a^3\beta(\beta^2+1)}-\frac{\beta^2-1}{\beta^2+1}\left[\frac{1}{2}\left(\frac{\partial w}{\partial y}+\frac{\partial v}{\partial z}\right)\right]\right)\\ &\left(t+\frac{3I_{x'}(\beta^2\beta_0+\alpha_0)}{16\pi\mu a^3\beta}(\beta^2+1)\left(1+\exp\left[-\frac{16\pi\mu a^3\beta}{3I_{x'}(\beta^2\beta_0+\alpha_0)}(\beta^2+1)t\right]\right)\right) \qquad \text{(D.24)}\end{aligned}$$

$$\begin{aligned}\theta_{y'}(t) &= \theta_{y',0}+\frac{1}{2}\left(\frac{\partial u}{\partial z}-\frac{\partial w}{\partial x}\right)t\\ &+ \frac{3I_{y'}\alpha_0}{16\pi\mu a^3\beta}\left(\omega_{y',0}-\frac{1}{2}\left(\frac{\partial u}{\partial z}-\frac{\partial w}{\partial x}\right)\right)\left[1-\exp\left(-\frac{16\pi\mu a^3\beta}{3I_{y'}\alpha_0}t\right)\right] \qquad \text{(D.25)}\end{aligned}$$

$$\begin{aligned}\theta_{z'}(t) &= \theta_{z',0} + \frac{1}{2}\left(\frac{\partial v}{\partial x} - \frac{\partial u}{\partial y}\right)t + \left[\frac{3I_{z'}(\beta^2\beta_0 + \alpha_0)}{16\pi\mu a^3\beta}(\beta^2+1)\right]\left(\omega_{z',0} - \frac{1}{2}\left(\frac{\partial v}{\partial x} - \frac{\partial u}{\partial y}\right)\right) \\ &\quad \left(1 - \exp\left(\frac{-16\pi\mu a^3\beta}{3I_{z'}(\beta^2\beta_0 + \alpha_0)}(\beta^2+1)t\right)\right) \\ &- \left(-\frac{3\omega_{y',0}\omega_{x',0}(I_{y'} - I_{z'})(\beta^2\beta_0 + \alpha_0)}{16\pi\mu a^3\beta(\beta^2+1)} - \frac{1-\beta^2}{\beta^2+1}\left[\frac{1}{2}\left(\frac{\partial v}{\partial x} + \frac{\partial u}{\partial y}\right)\right]\right) \\ &\quad \left(t + \frac{3I_{z'}(\beta^2\beta_0 + \alpha_0)}{16\pi\mu a^3\beta}(\beta^2+1)\left(1 + \exp\left[-\frac{16\pi\mu a^3\beta}{3I_{z'}(\beta^2\beta_0 + \alpha_0)}(\beta^2+1)t\right]\right)\right) \quad \text{(D.26)}\end{aligned}$$

D.2 Superellipsoid

Shape used by current work.

The formulation neglects the velocity gradient forces on the particle surface, leaving profile lift and drag as well as gravity in the equation of motion. The equations are valid for all types of flow.

Translation

$$c_1 = -\frac{1}{2}V_p\frac{\rho_g}{\rho_p}|\vec{u}_g - \vec{v}_p|(C_D A_p + C_L A_\alpha) \quad \text{(D.27)}$$

$$c_2 = \vec{u}_g \quad \text{(D.28)}$$

$$c_3 = \vec{g}\left[\frac{1}{\rho_p}\left(1 - \frac{\rho_g}{\rho_p}\right)\right] - A_p\bar{d}_p\vec{\nabla}P \quad \text{(D.29)}$$

Rotation about x' axis

$$\begin{aligned}c_1 &= -\frac{5\cos\theta_{1x'}K_\omega\mu_g A_s\bar{d}_p}{(1+R_\beta^2)a^2 m_p} \quad \text{(D.30)} \\ c_2 &= \frac{5\cos\theta_{1x'}}{a^2 m_p(1+\beta^2)}\frac{1}{2}\left(\frac{\partial w_g}{\partial y} - \frac{\partial v_g}{\partial z}\right) \quad \text{(D.31)} \\ c_3 &= \frac{5\cos\theta_{1x'}}{a^2 m_p(1+\beta^2)}\left[\frac{1}{2}C_{Nx'}\rho_g A_{\alpha u}x_{cpx'}|\vec{u}_g - \vec{v}_p|(u_g - u_p)\right] \quad \text{(D.32)} \\ &\quad + \frac{5\cos\theta_{2x'}}{a^2 m_p(1+\beta^2)}\left[K_\omega\mu_g A_s\bar{d}_p\left(\frac{1}{2}\left(\frac{\partial u_g}{\partial z} - \frac{\partial w_g}{\partial x}\right) - \Omega_y\right)\right. \\ &\quad \left. + \frac{1}{2}C_{Ny'}\rho_g A_{\alpha y}x_{cpy'}|\vec{u}_g - \vec{v}_p|(v_g - v_p)\right] \\ &\quad + \frac{5\cos\theta_{3x'}}{a^2 m_p(1+\beta^2)}\left[K_\omega\mu_g A_s\bar{d}_p\left(\frac{1}{2}\left(\frac{\partial v_g}{\partial z} - \frac{\partial w_g}{\partial y}\right) - \Omega_z\right)\right. \\ &\quad \left. + \frac{1}{2}C_{Nz'}\rho_g A_{\alpha z}x_{cpz}|\vec{u}_g - \vec{v}_p|(w_g - w_p)\right]\end{aligned}$$

Rotation about y' axis

$$c_1 = -\frac{5\cos\theta_{2y'}K_\omega\mu_g A_s\bar{d}_p}{2a^2m_p} \tag{D.33}$$

$$c_2 = \frac{5\cos\theta_{2y'}}{2a^2m_p}\frac{1}{2}\left(\frac{\partial u_g}{\partial z}-\frac{\partial w_g}{\partial z}\right) \tag{D.34}$$

$$\begin{aligned} c_3 = {} & \frac{5\cos\theta_{1y'}}{2a^2m_p}\left[K_\omega\mu_g A_s\bar{d}_p\left(\frac{1}{2}\left(\frac{\partial w_g}{\partial y}-\frac{\partial v_g}{\partial z}\right)-\Omega_x\right)\right. \\ & \left.+\frac{1}{2}C_{Nx'}\rho_g A_{\alpha x}x_{cpx'}|\vec{u}_g-\vec{v}_p|(u_g-u_p)\right] \\ & +\frac{5\cos\theta_{2y'}}{2a^2m_p}\left[\frac{1}{2}C_{Ny'}\rho_g A_{\alpha v}x_{cpy'}|\vec{u}_g-\vec{v}_p|(v_g-v_p)\right] \\ & +\frac{5\cos\theta_{3y'}}{2a^2m_p}\left[K_\omega\mu_g A_s\bar{d}_p\left(\frac{1}{2}\left(\frac{\partial v_g}{\partial x}-\frac{\partial u_g}{\partial y}\right)-\Omega_y\right)\right. \\ & \left.+\frac{1}{2}C_{Nz'}\rho_g A_{\alpha z}x_{cpz'}|\vec{u}_g-\vec{v}_p|(w_g-w_p)\right] \end{aligned} \tag{D.35}$$

Rotation about z' axis

$$c_1 = -\frac{5\cos\theta_{3z'}K_\omega\mu_g A_s\bar{d}_p}{(1+R_\beta^2)a^2m_p} \tag{D.36}$$

$$c_2 = \frac{5\cos\theta_{3z'}}{a^2m_p(1+\beta^2)}\frac{1}{2}\left(\frac{\partial v_g}{\partial x}-\frac{\partial u_g}{\partial y}\right) \tag{D.37}$$

$$\begin{aligned} c_3 = {} & \frac{5\cos\theta_{1z'}}{a^2m_p(1+\beta^2)}\left[K_\omega\mu_g A_s\bar{d}_p\left(\frac{1}{2}\left(\frac{\partial w_g}{\partial y}-\frac{\partial v_g}{\partial z}\right)-\Omega_x\right)\right. \\ & \left.+\frac{1}{2}C_{Nx'}\rho_g A_{\alpha x}x_{cpx'}|\vec{u}_g-\vec{v}_p|(u_g-u_p)\right] \\ & +\frac{5\cos\theta_{2z'}}{a^2m_p(1+\beta^2)}\left[K_\omega\mu_g A_s\bar{d}_p\left(\frac{1}{2}\left(\frac{\partial u_g}{\partial z}-\frac{\partial w_g}{\partial x}\right)-\Omega_y\right)\right. \\ & \left.+\frac{1}{2}C_{Ny'}\rho_g A_{\alpha y}x_{cpy'}|\vec{u}_g-\vec{v}_p|(v_g-v_p)\right] \\ & +\frac{5\cos\theta_{3z'}}{a^2m_p(1+\beta^2)}\left[\frac{1}{2}C_{Nz'}\rho_g A_{\alpha z}x_{cpz'}|\vec{u}_g-\vec{v}_p|(u_g-u_p)\right] \end{aligned} \tag{D.38}$$

Appendix E

Partial differentiation of numerical quantities

In the equations of motion of non-spherical particles, a number of partial derivatives of the flow field occur. As this is given as discrete numerical values through the solution of the Navier-Stokes equations, a method must be devised to calculate the necessary first and second order derivatives.

Consider first the definition of a derivative:

$$f'(x) = \lim_{h \to 0} \frac{f(x+h) - f(x)}{h} \tag{E.1}$$

Applying a central difference formulation on E.1, it becomes

$$f'(\bar{x}) = \frac{f(x+h) - f(x)}{h} \tag{E.2}$$

$\bar{x}$: "midpoint" of $(x+h)$, implying that $f'(\bar{x})$ is constant, thus implying a linear variation in f in this interval.

In practical use, h will be closely linked either to the cell dimensions, as the initial interpolations will be based on the cell corner coordinates, or to the timestep, with which the particle moves.

Applying the central difference formulation once again, the second derivative can be written as

$$f''(x) = \frac{f(x+h) - 2f(x) + f(x-h)}{h^2} \tag{E.3}$$

E.3 implies use of a constant cell dimension h, which by no means is guaranteed. However, replacing h by h_1 and h_2, respectively, E.3 becomes

$$f''(x) = \frac{f(x+h_2) - f(x)}{h_2^2} - \frac{f(x) - f(x-h_1)}{h_1^2} \tag{E.4}$$

Equations E.2 and E.4 thus provide the tools for evaluation of spin and deformation rate tensors as well as the D^2 operator, which ties the particle shape to the spatial gradient of the velocity field, at any point in the domain.

Appendix F

Burnout times

In the following, theoretical expressions for the burn out time τ_b, of solid fuel particles are given subject to different reaction controls. For all the cases, the following assumptions are made:

- The particle is subject to a constant heating rate
- The mean boundary layer temperature is equal to the particle temperature
- The particle is fully devolatilized before heterogeneous combustion initiates

The nomenclature for all equtions in this appendix is given below.

k: heating rate $[K/s]$
m_a, m_c: ash and carbon mass fractions $[-]$
m_{c0}: initial carbon mass fraction $[-]$
T_{p0}: initial particle temperature $[K]$
d_{p0}: initial particle diameter $[m]$
R: universal gas constant $[kJ/kgK]$
E: activation energy $[kJ/kg]$
p_{O_2}: oxygen partial pressure $[Pa]$
M_C: molecular mass of carbon $[kg/kmol]$
A_Γ: pre-exponential factor for CO/CO_2 ratio (equation 3.23)
$D_0,\ T_0$: equation 3.9
n_c: reaction order (equation 3.19)
$b = -\frac{E}{R}$
$k_0 = \frac{R}{2\pi d_{p0} p_{O_2} M_C (m_{c0}+m_a)^{1/3}}$
$C_{01} = \frac{A_\Gamma D_0}{(2T_0)^{1.75}}$
$C_{02} = \frac{(m_{c0}+m_a)^{2/3}}{\pi p_{O_2} d_{p0}^2}$

F.1 All models, diffusion control

$$\begin{aligned}\frac{k_0}{4}\left(m_a^{4/9}-(m_{c0}+m_a)^{4/9}\right) \approx \frac{C_{01}}{k}\Bigg[&\frac{(T_{p0}+k\tau_b)^{-5/4}\exp\left(\frac{b}{T_{p0}+k\tau_b}\right)}{b}\\ &-\frac{5}{4b^2}(t_{p0}+\tau_b)^{-1/4}\exp\left(\frac{b}{T_{p0}+k\tau_b}\right)\\ &+\frac{5}{16b^3}(T_{p0}+k\tau_b)^{3/4}\exp\left(\frac{b}{T_{p0}+k\tau_b}\right)\Bigg]\\ -\frac{C_{01}}{k}\Bigg[&\frac{T_{p0}^{-5/4}\exp\left(\frac{b}{T_{p0}}\right)}{b}\\ &-\frac{5}{4b^2}T_{p0}^{-1/4}\exp\left(\frac{b}{T_{p0}}\right)\\ &+\frac{5}{16b^3}T_{p0}^{3/4}\exp\left[\left(\frac{b}{T_{p0}}\right)\right]\end{aligned} \tag{F.1}$$

F.2 Mixed control model, kinetic control

$$\begin{aligned}3C_{02}\left(m_a^{1/3}-(m_{c0}+m_a)^{1/3}\right) = \frac{kAR}{E}\Bigg[&\frac{\exp\left(\frac{b}{T_{p0}+k\tau_b}\right)}{b}\Big((T_{p0}+k\tau_b)^{-2}\\ &-\frac{2}{b(T_{p0}+k\tau_b)}+\frac{2}{(T_{p0}+k\tau_b)^2}\Big)\\ &-\frac{\exp\left(\frac{b}{T_{p0}}\right)}{b}\left(T_{p0}^{-2}-\frac{2}{bT_{p0}}+\frac{2}{T_{p0}^2}\right)\Bigg]\end{aligned} \tag{F.2}$$

F.3 Reactivity index model, kinetic control

$$\begin{aligned}\left(p_{O_2c}^n f(X)k_0\right)^{-1}\left(\ln(m_{c,min})-\ln(m_{c0})\right) = \frac{kR}{E}\Bigg[&\frac{\exp\left(\frac{b}{T_{p0}+k\tau_b}\right)}{b}\Big((T_{p0}+k\tau_b)^{-2}\\ &-\frac{2}{b(T_{p0}+k\tau_b}+\frac{2}{(T_{p0}+k\tau_b)^2}\Big)\\ &-\frac{\exp\left(\frac{b}{T_{p0}}\right)}{b}\left(T_{p0}^{-2}-\frac{2}{bT_{p0}}+\frac{2}{T_{p0}^2}\right)\Bigg]\end{aligned} \tag{F.3}$$

Appendix G

Laser Sheet analysis

In order to evaluate the flow patterns around arbitrary particles with respect to determining drag and lift characteristica, an experimental setup has been used to perform Laser Sheet Visualisation of the flow pattern in the wake of different superellipsoids: a sphere, a cylinder, an ellipsoid and a general superellipsoid at three different subcritical Reynolds numbers, 500, 1000 and 1500, and incidence angles ranging from zero to ninety degrees. The experimental results in the form of wake patterns and upper surface separation points have been compared to results from CFD predictions using CFX5.1.

G.1 Experimental setup

The experimental part of this work is based on **L**aser **S**heet **V**isualisation (LSV) techniques, where a thin laser light sheet provides a two-dimensional picture of the flow being investigated. The flow is seeded with tiny particles of the order of 10-20 μm, which reflect the laser light upon passage through the sheet, thus giving an accurate picture of the flow structure.

The test rig (see figure G.1) consists of a rectangular channel of dimensions $0.1 \times 0.7 \times 1.2$ metres, fitted with a bellmouth at the inlet, and a perforated plate at the outlet. Flow in the channel is generated by a suction blower, situated above the channel. The perforated plate generates a localised pressure drop large enough to ensure that the flow is even across the central part of the channel cross-section. In the tube section upstream the suction blower, an orifice plate is placed, in order to determine volumetric flow rates in the system through a pressure drop across the plate, and subsequently flow velocities in the channel.

The superellipsoids under investigation are placed on a horizontal arm, perpendicular

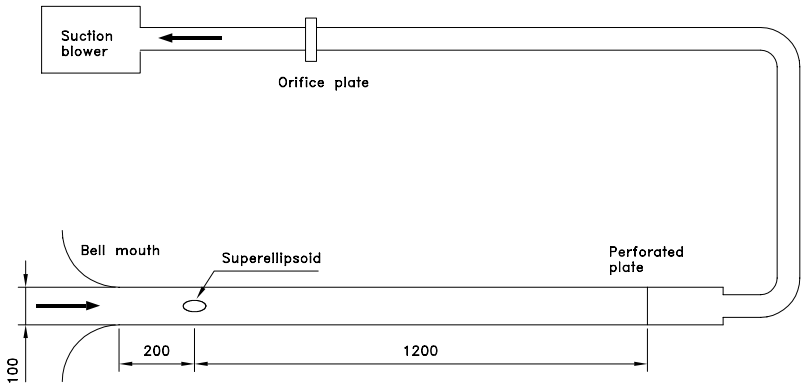

Figure G.1: Channel setup with orifice plate for determination of flow velocity and location of superellipsoid.

to the flow direction, 0.2 metres from the end of the bellmouths (see figure G.2). The arm enables the superellipsoid to be turned through flow incidence angles ranging from $-90°$ to $90°$.

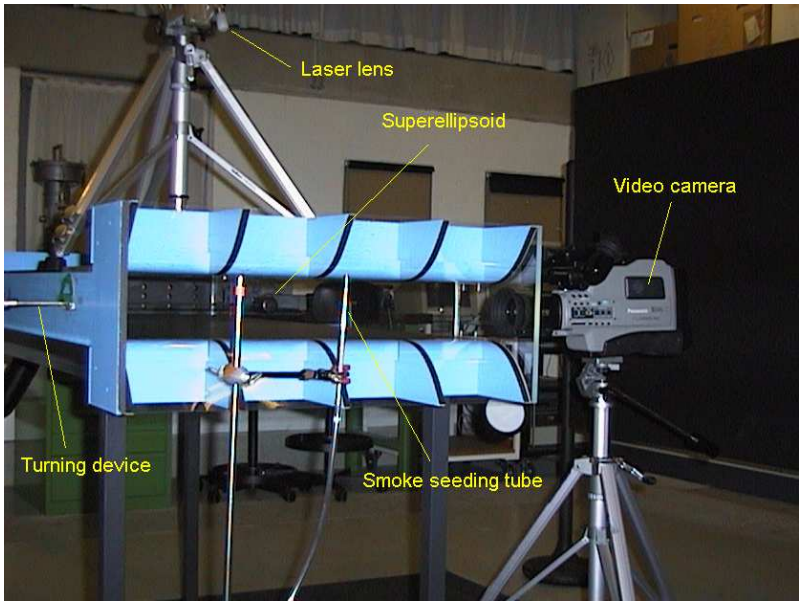

Figure G.2: Position of superellipsoid and location of laser sheet, smoke generator and video camera.

The air flowing into the channel is seeded with smoke, and a video camera is placed such that the motion of the air in a vertical two-dimensional plane around the superellipsoid can be filmed.

The flow patterns around the superellipsoid have been investigated under the conditions

Re_p [−]	500, 1000, 1500
Incidence angles [°]	0, 5, 10, 15, 30, 45, 60, 90

Table G.1: Experimental setup

given in table G.1.

G.2 Numerical setup

The calculations are all performed using CFX5.1, which is a fully unstructured code using a coupled solver solution strategy. The mesh is constructed such that the density at the surface of the superellipsoid is very fine, with an approximate grid length scale of $0.5 - 1.5$ millimetres in this region (see figure G.3). In order to save time and system resources, a symmetry plane is defined at the location of the laser sheet shown in figure G.2. A plug flow velocity corresponding to the orifice gauge measurements is prescribed at the channel inlet, which is extended numerically 100 millimetres compared to the experimental setup, in order to ensure fully developed flow at the superellipsoid.

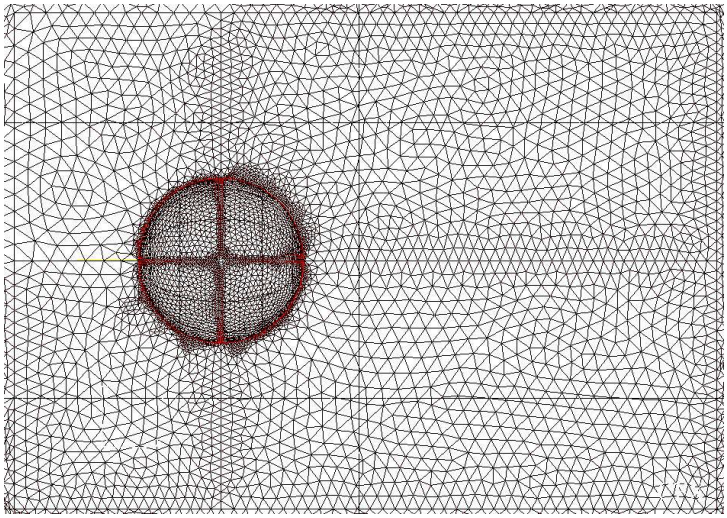

Figure G.3: Two-dimensional plot of the mesh structure on the symmetry plane and superellipsoid surface, in this case a sphere.

Table G.2 shows details of the computational setup.

Re_p [−]	500, 1000, 1500
Incidence angles [°]	0, 5, 15, 30, 35, 60, 75, 90
Turbulence closure	RNG k-epsilon
Inlet velocity profile	Plug flow
Calculation type	Steady state

Table G.2: Numerical setup

G.3 Results

G.3.1 Experimental results

The experimental results generally show that there is quite a difference in wake patterns between the superellipsoids, and that, to a large extent, these differences are governed by the superelliptic exponent, ie. the curvature at the ends of the superellipsoid. Also contributing to this effect is the axes aspect ratio. Leaving aside the sphere, the ellipsoid was the only particle with an axes aspect ratio different from one to exhibit "profile characteristics", that is two- dimensional flow at the centreline of the particle, at non-zero angles of incidence, in the sense that the vertical flow around the ellipsoid is strong enough to dominate the near-wake structure. For the other two particles at non-zero angles of incidence, an attached flow region around the central part of the particle establishes itself, where the horizontal flow around the particle dominates. At the top and bottom of the attached flow region, reverse flow regions were observed (see figures 2.7 and G.4).

This is clearly visible in the right hand picture in figure G.6, where a vertical slice is made through the wake. The narrow vertical region - the "stem" - is the attached flow wake, whereas the bottom circular pattern is the reverse flow region.

Rotating particles

As it is unlikely that the particles remain stationary relative to the surrounding fluid long enough for the wakes to develop, it is interesting to qualitatively investigate the effect of rotation on the wake. For this purpose, a sphere at $Re_p = 1000$ was rotated counter-clockwise. As can be seen on figure G.7, the centreline of the wake moves up along the upper surface of the particle. For the case of slow rotation, the wake remains very symmetrical, but as the rotaional speed increases, the wake assumes a strong clock-wise rotation.

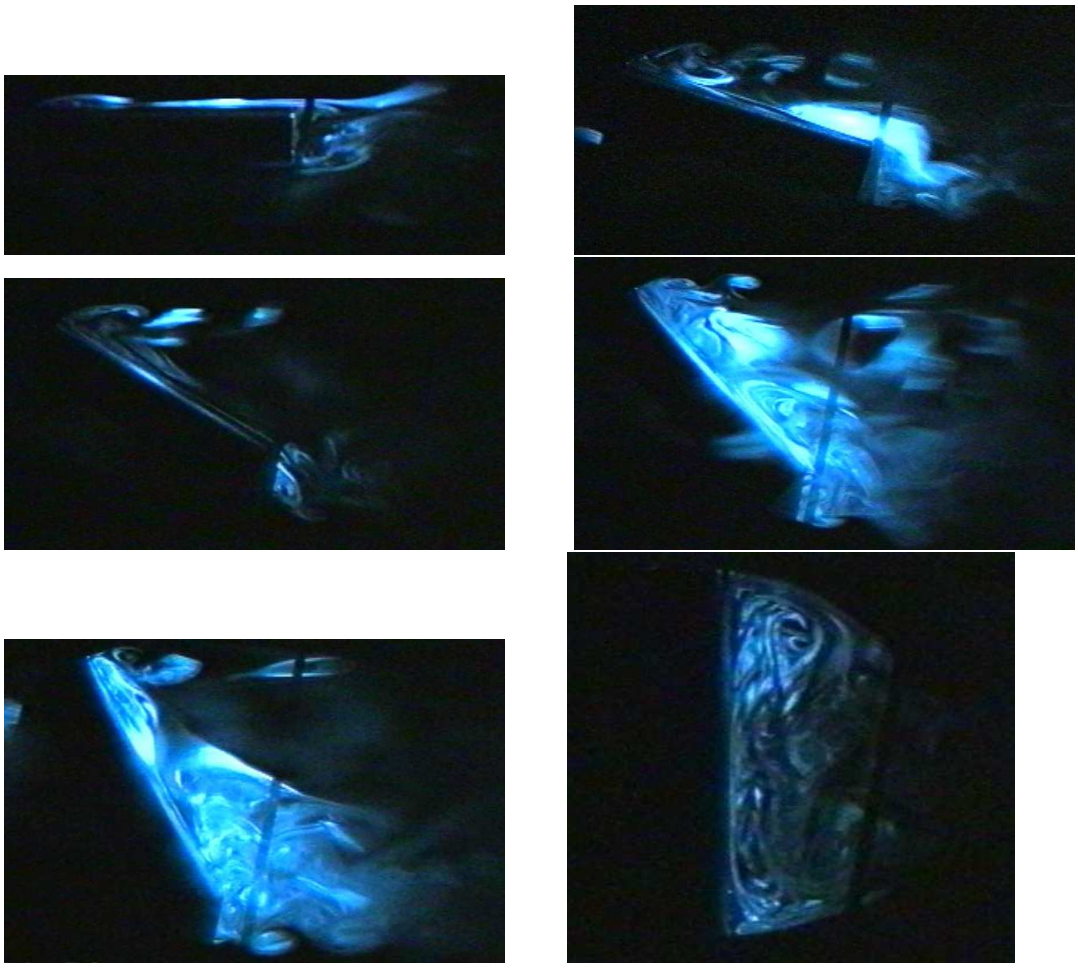

Figure G.4: Photographed wakes of cylinders at $Re_p = 1000$ and incidence angles $[0, 15, 30, 45, 60, 90]$ degrees.

G.3.2 Numerical results

In general, the overall characteristics of the numerical calculations correspond well to those observed experimentally. However, transient phenomena are obviously not included in the calculations, and the results of enforcing a steady state solution may influence the results, such that direct comparison between the steady state calculations and the instantaneous LSV pictures is difficult, as shown on figure G.8. There is a tendency in the numerical results to overemphasize the "non-profile characteristics" of the general superellipsoid and the cylinder in the calculations, although the general features of the wakes at the different incidence angles are captured, in particular the calculated near-wake structure of the ellipsoid corresponds well to the experimental.

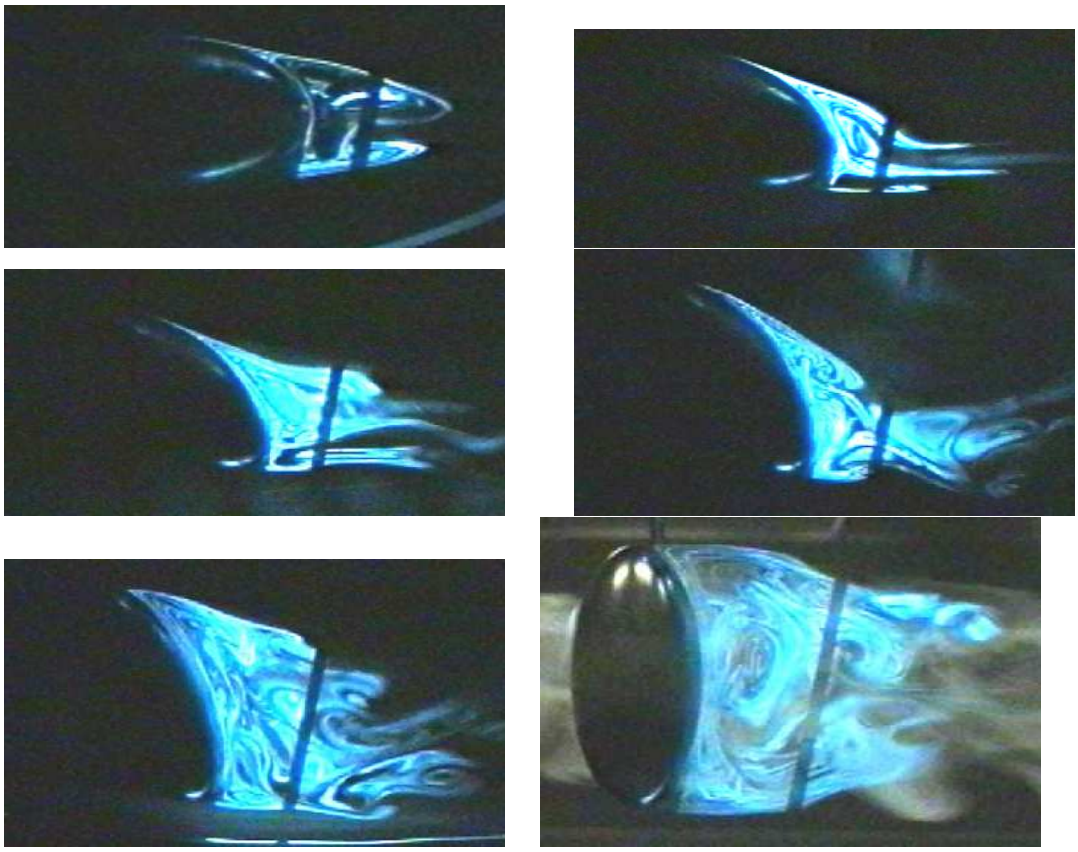

Figure G.5: Photographed wakes of ellipsoids at $Re_p = 1000$ and incidence angles $[0, 15, 30, 45, 60, 90]$ degrees.

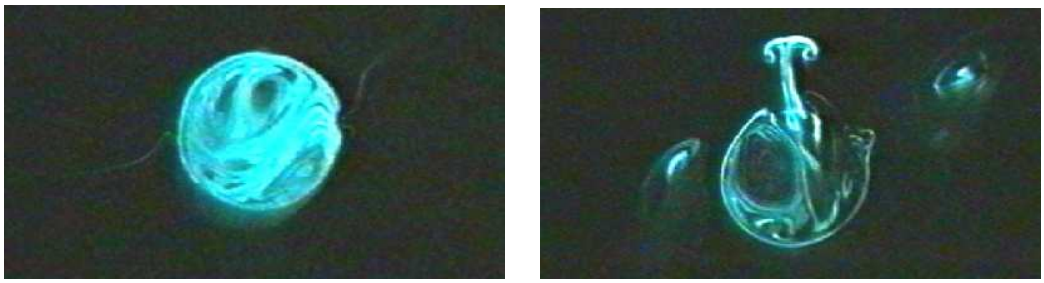

Figure G.6: General superellipsoids at $Re_p = 1000$, and zero and fifteen degrees incidence, respectively. Vertical slice taken approximately one diameter behind the trailing edge.

Upper surface separation point location

As an indication of the quality of a CFD-calculation of this type, the location of the separation point along the centre line of the upper surface can be used. For the ellipsoid (see figure G.10), very good correspondence between calculation and experiment was obtained.

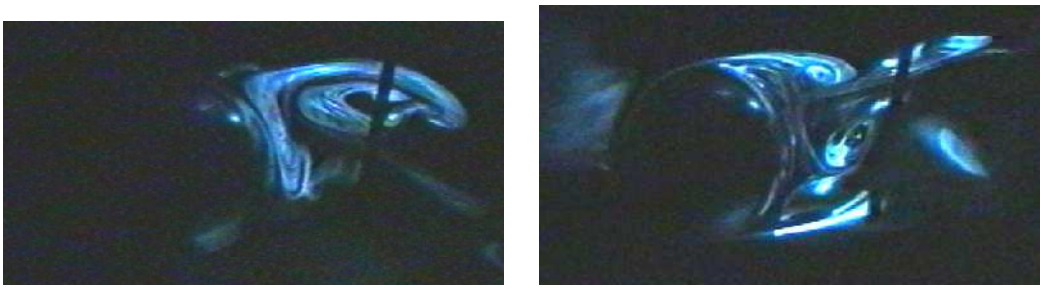

Figure G.7: Rotating spheres at $Re_p = 1000$. Flow enters horizontally from the left, and the spheres rotate counter-clockwise. Left picture: fast rotation. Right picture: slow rotation.

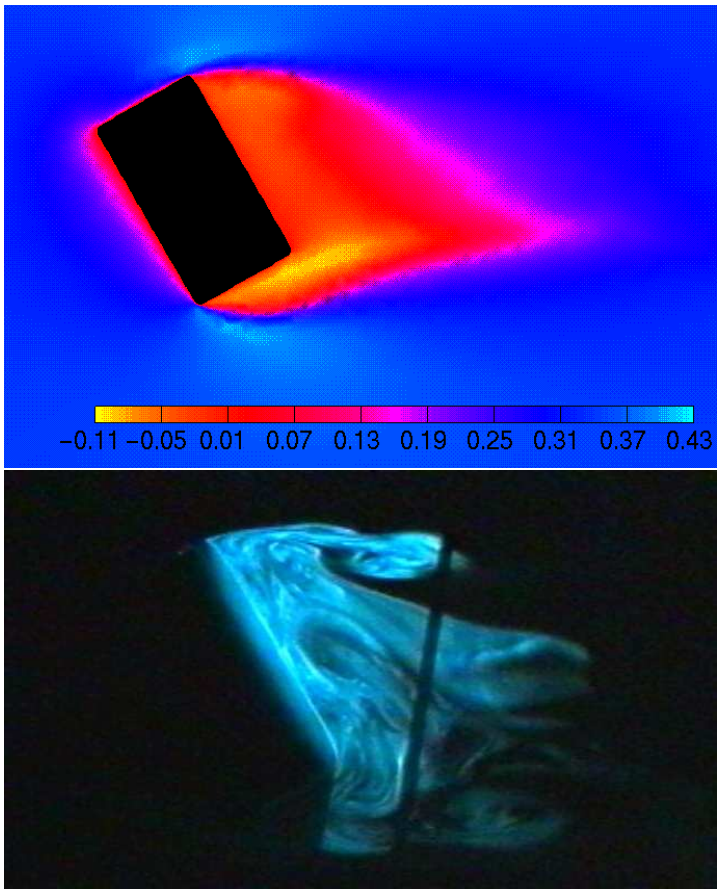

Figure G.8: Comparison of predicted and photographed wake structures of general superellipsoids at 60° incidence and $Re_p = 1000$. Top: steady state CFD calculation. Bottom: LSV picture.

As previously discussed, it is irrelevant to refer to an upper body separation point when dealing with superellipsoids with relatively high exponents and axes aspect ratios different from unity. With such particles, the flow will tend to separate at the point of highest curvature, and re-attach further down the upper surface. As the curvature of the upper surface is very localised, there is no geometrically caused adverse pressure

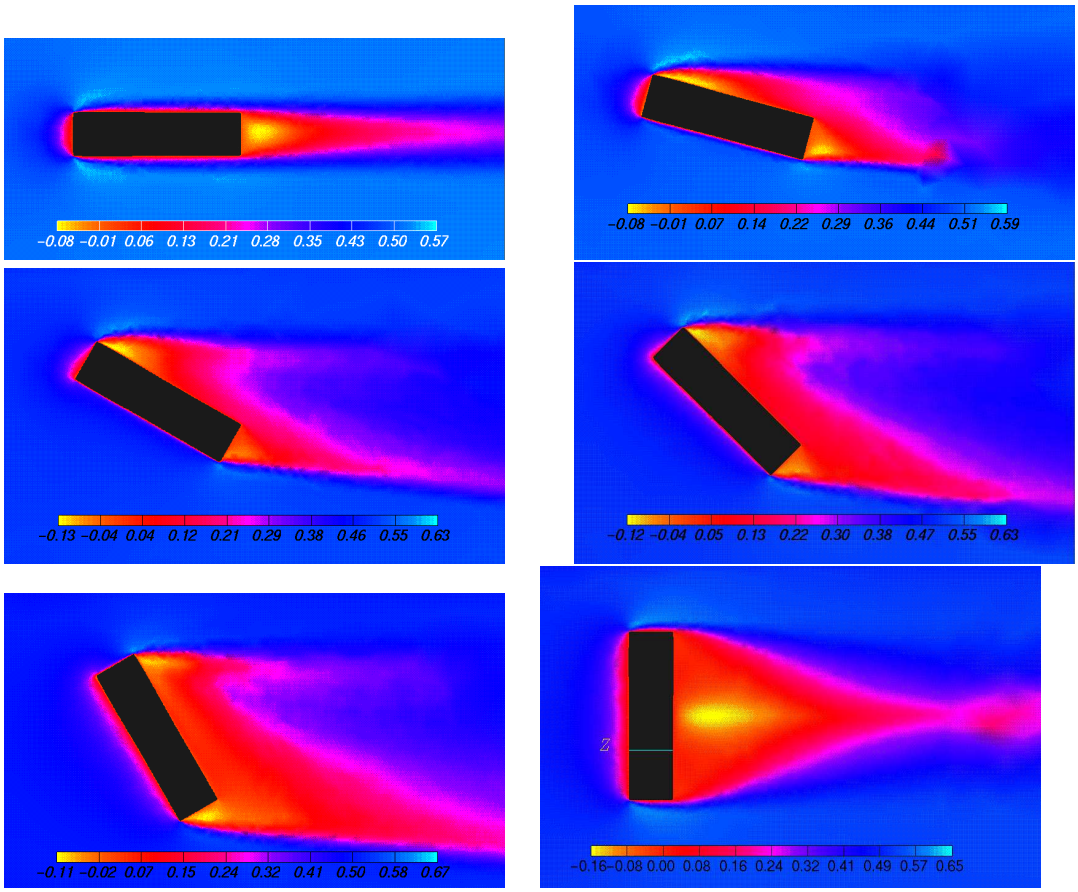

Figure G.9: Predicted wakes of cylinders at $Re_p = 1000$ and incidence angles $[0, 15, 30, 45, 60, 90]$ degrees.

gradient (as in the case of the ellipsoid, where the curvature is distributed along the entire upper surface) and this re- attachment can take place.

Drag and lift calculations

Among the outputs from the CFD calculations are information on the lift and drag forces on the particles. Transforming these into coefficients, they can be compared to the correlated values of equation 2.27 (see figures 2.8 and 2.9).

A general observation is that the calculated values generally lie higher than measurements performed by numerous investigators at right angles, whereas the correlated values are in correspondence with these. Furthermore, the drag coefficient seems to be almost invariant to changes in the incidence angle, except for the case of the cylinder, where the coefficient falls with increasing incidence angle. This effect, which is due to relating the drag coefficient to the projected area in spite of the high area ratio causing viscous drag to play an important role at zero degrees incidence, is reproduced in figure

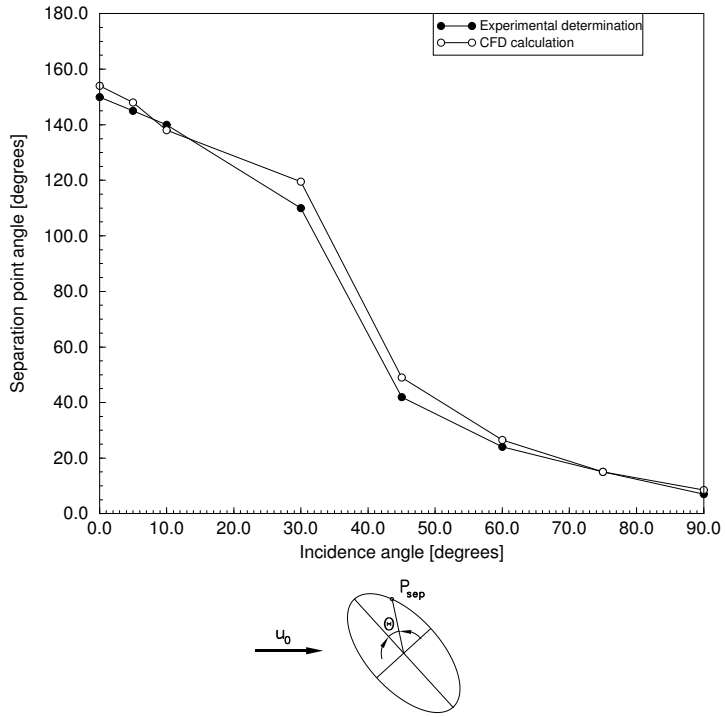

Figure G.10: Location of upper surface separation point: angle (θ) between major axis and upper surface separation point, as shown at the bottom of the figure. $Re_p = 1000$.

2.9, using equation 2.30.

Figure 2.11 shows the ratios of drag versus lift coefficients for superellipsoids at $Re_p = 1000$. Except for the cylinder, the CFD predictions correspond well with equation 2.32. The cylinder, on the other hand, deviates markedly from equation 2.32, which is likely to be due to the two recirculation zones located at either end. Equation 2.32 is based on the aerodynamics of an infinitely long cylinder, and does not take the above mentioned end-effects into account. For the other two superellipsoids, these effects are not so severe, and therefore their behaviour is more akin to that of an infinitely long cylinder.

G.4 Summary

Generally, the wake pattern is well reproduced by the CFD calculations, where it is possible to distinguish a number of the characteristic features of the experimental results. The location of the upper body separation points show very good agreement between the experimental and numerical predictions, whereas the lift and drag predictions of the CFD calculations for all cases are too high. Comparisons between the existing drag correlation for superellipsoids and the CFD predictions show general agreement,

although some discrepancies are noted, particularly for superellipsoids with high exponents and axes aspect ratios at low angles of incidence. In this regime, the wake behind such particles is divided into two distinct parts, with reverse flow at the ends of the particle, and attached flow at the central part of the particle.

This work has shown that although superellipsoids, from a mathematical perspective are identical, there are large aerodynamic differences connected to them. It is also apparent that, although much more knowledge is neccessary to accurately predict lift and drag of arbitrary superellipsoids, the current approach is sound and provides a reasonable estimate, and that it captures the main features of the behaviour of the aerodynamic coefficients at different angles of incidence and Reynolds numbers.

At the same time, the power of LSV[1] techniques to supply at least part of this knowledge is clearly demonstrated. In order to quantitatively work on improving the drag and lift correlations, Laser Doppler Anemometry would be an appropriate method.

Finally, the CFD predictions capture the general flow features well, as well as the trends in the aerodynamic coefficients as functions of incidence angles are reasonably well predicted. However, in order to base future drag and lift correlations upon results from CFD calculations, it is again neccessary to have more extensive measurement data to use to validate the results.

[1]LSV pictures of all flow configurations investigated can be found at `http://www.iet.auc.dk/afd2/lab/lsvpart.html`

Appendix H

Sample PCOMBUST command and log file

H.1 Command file

```
/*****************************************************************/
/*                       CALCSPEC.CFG                            */
/*   Configuration file for particle tracking and combustion     */
/*                                                               */
/*                       PCOMBUST Release 3.0                    */
/*                  Aalborg University, 1995                     */
/*                                                               */
/* Set up for MKS1 tunnel furnace for combi-firing - straw inlet */
/*****************************************************************/
>>PCOMBUST
>>FLOW SOLVER CFX4
  >>CALCULATION SPECIFICATION
    NAME mks1_comb_combi
    THREE DIMENSIONS
    CARTESIAN COORDINATES
/*    INITIALIZE
    TRACKING AND COMBUSTION
    FLUID DENSITY 1.2
    FLUID VISCOSITY 15.8E-6
    RESULT DIRECTORY straw_mks1
    MESH FILE m01.geo
    TOPOLOGY FILE combi_straw.topo
    DUMP FILE combi_hot_base.dmp
    UNFORMATTED DUMP FILE
    READ PARTICLE FILE
    PARTICLE FILE mks1_straw.dat

  >>INLET SPECIFICATION
```

```
    INLET NAME CEN_INLET
    ROSIN-RAMMLER SIZE DISTRIBUTION
    RELATIVE VARIANCE 2.0
    MASS MEAN PARTICLE DIAMETER 500.E-6
    INLET DENSITY 150.
    NUMBER OF PARTICLES 1250
    SUPERELLIPTIC EXPONENT 50.0
    ASPECT RATIO 25.
    MAXIMUM DIAMETER 2500.E-6
    MINIMUM DIAMETER 20.E-6
    CIRCUMFERENTIAL DISTRIBUTION
    CENTRE AXIS 0.22 0.0 0.0
    INLET INNER RADIUS 0.0
    INLET OUTER RADIUS 0.13
    >>INLET VELOCITY
      USER SPECIFIED 16.2 0. 0.
    INLET MASS FLOW 1.32
    PARTICLE INLET TEMPERATURE 333.
    PARTICLE LOWER HEATING VALUE 14.5
    VOLATILE MOLECULAR MASS 16.0
    VOLATILE LATENT HEAT 4.26E5
    SWELLING INDEX 1.0
   >>PARTICLE PROPERTIES
      VOLATILES .707
      CHAR .161
      ASH .0453
      WATER .0867

/* The kinetic parameters are estimated for straw, approx. 0.9x coal values

    >>KINETIC PARAMETERS
      EVAPORATION PRE-EXPONENTIAL FACTOR 7.94E12
      EVAPORATION ACTIVATION ENERGY 9528.75
      DEVOLATILIZATION PRE-EXPONENTIAL FACTOR 7.94e12
      DEVOLATILIZATION ACTIVATION ENERGY 9528.75
      KINETIC RATE PRE-EXPONENTIAL FACTOR .86
      KINETIC RATE ACTIVATION ENERGY 1.248e3
   END

  >>SOLVER OPTIONS
    GRAVITY VECTOR    0.0 -9.82 0.0
    >>UNDER RELAXATION FACTORS
      MOMENTUM 1.0
      ENTHALPY 1.0
      SCALARS  1.0
      END
    >>DISPERSION MODEL
      EDDY LIFETIME
      >>UNDER RELAXATION FACTORS
        UU  1.
        VV  1.
        WW  1.
```

```
        END
      CMY  0.16
      END
    ARRHENIUS PYROLYSIS MODEL
    MIXED CONTROL COMBUSTION MODEL
    COMBUSTION PRODUCT TEMPERATURE DEPENDENT
    TEMPERATURE SCALE FACTOR 7.5
/*   >>STEFAN FLOW INCLUDED
/*      VOLATILES ONLY
    >>SPECIES TRANSPORT EQUATIONS
      VOLATILE MASS FRACTION MF FUEL
      CARBON MONOXIDE MASS FRACTION MF CO
      MIXTURE FRACTION MIXT FRAC
    ACTIVE SURFACE CORRECTION
    MAXIMUM RESIDENCE TIME 8.50
    MAXIMUM NUMBER OF TIME STEPS 2500000
    MAXIMUM NUMBER OF WALL COLLISIONS 1000
  >>OUTPUT OPTIONS
    PARTICLE SCALE FACTOR 10.
    COLOUR TRAJECTORIES BY TEMPERATURE
    END
  >>LOG FILE OPTIONS
    EACH TRAJECTORY
    END
>>STOP
```

H.2 Log file

```
 PPPP
 P   P
 P   P
 PPPP   CCC   OOO   M    M  BBB   U   U   SSSS  TTTTT
 P     C     O   O  MM  MM  B  B  U   U  S        T
 P     C     O   O  M MM M  BBB   U   U   SSS     T
 P     C     O   O  M    M  B  B  U   U      S    T
 P      CCC   OOO   M    M  BBB    UUU   SSSS     T


 Reading front end data specified in calcspec.cfg
 Done reading command file - processing keywords

 CALCULATION SETUP

 CALCULATION TITLE:  mks1_comb_combi
 NUMBER OF DIMENSIONS: three
 COORDINATE TYPE: cartesian
 FLOW SOLVER: CFX4
 MESH FILE: m01.geo
```

```
TOPOLOGY FILE: combi_straw.topo
DUMP FILE: combi_hot_base.dmp
RESULT DIRECTORY: straw_mks1
HETEROGENEOUS COMBUSTION: MIXED CONTROL MODEL
PARTICLE DATA FILE: mks1_straw.dat
PROBLEM TYPE: combustion
Particle data file read
NUMBER OF INLETS:  1

INLET NAME: CEN_INLET
PARTICLE INLET TEMPERATURE:  333.0000000
PYROLYSIS MODEL : ARRHENIUS
Colouring trajectories by particle temperature
User defined maximum number of time steps  2500000
User defined maximum number of wall collisions  1000
No block search accuracy criterion defined - using default value of 0.001

SOLVER OPTIONS:

GRAVITY VECTOR:  0.0000000000E+00 -9.819999695 0.0000000000E+00
UNDER RELAXATION FACTORS:
MOMENTUM:  1.000000000
SCALARS :  1.000000000
ENTHALPY:  1.000000000
UU      :  1.000000000
VV      :  1.000000000
WW      :  1.000000000
DISPERSION MODEL: Eddy lifetime
CMY:  0.1599999964
TTSF:  0.0000000000E+00
Mesh specification from Flow3D grid file m01.geo                        :
Number of blocks:  32
Total number of cells:  122800
Block sizes:
NUMBER-1                        10 10 10
NUMBER-2                        10 10 10
NUMBER-3                        10 10 10
NUMBER-4                        10 10 10
NUMBER-5                        10 10 12
NUMBER-6                        10 10 12


               ⋮


NUMBER-27                       10 10 25
NUMBER-28                       10 10 25
NUMBER-29                       10 10 25
NUMBER-30                       10 10 25
NUMBER-31                       10 10 25
NUMBER-32                       10 10 25
```

```
Topological information from m01.geo                          :
FLUID INLETS:
Block and patch name:  1 PRI_INLET
 Range:  1 4 1 12 1 1 6 1
Block and patch name:  2 PRI_INLET
 Range:  1 1 1 4 1 12 4 2
Block and patch name:  3 PRI_INLET
 Range:  1 1 1 4 1 12 4 3
Block and patch name:  4 PRI_INLET
 Range:  1 4 1 1 1 12 5 4
Block and patch name:  1 SEC_INLET
 Range:  6 12 1 12 1 1 6 1
Block and patch name:  2 SEC_INLET
 Range:  1 1 6 12 1 12 4 2
Block and patch name:  3 SEC_INLET
 Range:  1 1 6 12 1 12 4 3
Block and patch name:  4 SEC_INLET
 Range:  6 12 1 1 1 12 5 4
Block and patch name:  6 CEN_INLET
 Range:  1 9 1 12 1 1 6 6
Block and patch name:  9 CEN_INLET
 Range:  1 9 1 12 1 1 6 9
Block and patch name:  10 CEN_INLET
 Range:  1 9 1 12 1 1 6 10
Block and patch name:  12 CEN_INLET
 Range:  1 9 1 12 1 1 6 12
Block and patch name:  5 CEN_INLET
 Range:  1 12 1 12 1 1 6 5
FLUID OUTLETS:
Block and patch name:  24 OUTLET
Range:  1 12 1 12 27 27 3 24
Block and patch name:  25 OUTLET
Range:  1 12 1 12 27 27 3 25
Block and patch name:  26 OUTLET
Range:  1 12 1 12 27 27 3 26
Block and patch name:  27 OUTLET
Range:  1 12 1 12 27 27 3 27
Block and patch name:  28 OUTLET
Range:  1 12 1 12 27 27 3 28
Block and patch name:  29 OUTLET
Range:  1 12 1 12 27 27 3 29
Block and patch name:  30 OUTLET
Range:  1 12 1 12 27 27 3 30
Block and patch name:  31 OUTLET
Range:  1 12 1 12 27 27 3 31
Block and patch name:  32 OUTLET
Range:  1 12 1 12 27 27 3 32
WALL BOUNDARIES:
PRESSURE BOUNDARIES:
SYMMETRY BOUNDARIES:
BLOCK-TO-BLOCK GLUE PATCHES:
```

```
 Reading cell vertices for all blocks...
 Done - no errors encountered. Closing m01.geo

 Creating dummy cells at block boundaries
 Completed.

 Determining max and min x and y coordinates of each   block:
Block   1
     :
Max:    .2150  -.1400   .4450
Min:    .0000   .0000   .0000
Block   2
     :
Max:    .2150   .0000   .0000
Min:    .0000  -.1400  -.1400
Block   3
     :
Max:    .2150   .5010   .0000
Min:    .0000   .0000  -.5010
Block   4
     :
Max:    .2150   .4450   .5010
Min:    .0000   .0000   .0000
Block   5
     :
Max:    .4250   .0400   .0400
Min:    .2150  -.0400  -.0400
Block   6
     :
Max:    .5650  -.0400   .1800
Min:    .2150   .0000   .0000


                ⋮


Block  27
     :
Max:  13.5650   .6100   .0000
Min:   8.5650   .0000  -.6100
Block  28
     :
Max:  13.5650   .0000   .0000
Min:   8.5650  -.6100  -.6100
Block  29
     :
Max:  13.5650  -.6100   .0000
Min:   8.5650   .0000 -1.2000
Block  30
     :
Max:  13.5650   .1800   .1800
Min:   8.5650  -.1800  -.1800
Block  31
```

```
     :
Max:  13.5650  -.1800   .6100
Min:   8.5650   .0000   .0000
Block  32
     :
Max:  13.5650   .0000  1.2000
Min:   8.5650 -1.2000   .0000
Topological assignments from file
m01.geo completed - all additional information will be read from the
Pcombust topology file, if specified.

 Reading Pcombust topology file combi_straw.topo
 Additional patches/patch groups to set:  1
 Assigning patch group(s)
 173 1 9 1 12 1 1 6 6
 174 1 9 1 12 1 1 6 9
 175 1 9 1 12 1 1 6 10
 176 1 9 1 12 1 1 6 12
 177 1 12 1 12 1 1 6 5
 PARTIN  CEN_INLET
 Creating topology integer array (iblank)
 Assigning fluid inlets
 Assigning fluid outlets
 Assigning particle inlet
 Initialising flow variables from FLOW3D dump file combi_hot_base.dmp
 Initialising combustion variables.
 Combustion and tracking - reading:
 U velocity (U)
 V velocity (V)
 W velocity (W)
 + Pressure (P)
 Turbulent kinetic energy (TKIN)
 Turbulent dissipation (EPS)
 Temperature (TEMP)
 CO mass fraction (YCO)
 Volatiles mass fraction (YVOL)
 Reading UNFORMATTED dump file combi_hot_base.dmp
 Success
 Done reading dump file...
 Interpolating variables to cell corners
 U velocity done...
 V velocity done...
 W velocity done...
 U vorticity done...
 V vorticity done...
 W vorticity done...
 Turbulent kinetic energy done...
 Turbulent dissipation done...
 READING PARTICLE START DATA FILE mks1_straw.dat
 INITIALISING A TOTAL OF  1250  PATHS

   **********      **********    ***************
```

```
INITIALISATION COMPLETE - STARTING RUN OF PCOMBUST
  **********      ***********    ***************


Path number  1
Particle surface area:  0.7835269906E-02 mm^2
Particle volume      :  0.6544982898E-04 mm^3
Equivalent spherical diameter (area):  0.4994040355E-01 mm
Equivalent spherical diameter (volume):  0.5001498014E-01 mm
Single particle and trajectory mass flow [micrograms]:  0.9817474522E-02 528000.0
Trajectory number flow:  53781652.00
Projected area ratio:  0.9993156791
Minor axis:  0.2499999851E-01
Aspect ratio:  1.000000000
Superelliptic exponent:  2.000000000
Initial block and cell:  5 9 9 2 0
Initial velocity:  16.20000076 0.0000000000E+00 0.0000000000E+00
Available char mass flow [kg/s]:  0.8500800323E-04 0.8500801050E-04
number of executed iterations:  4347
number of wall collisions:  0
total residence time [s] :  0.8295189589E-02
final position [m]:  0.3906139433 -0.9283187683E-03 -0.1525041647E-01
final cell number and type:  5 9 8 12 0
final velocity [m/s]:  19.59221268 -0.2365801781 0.4292835295
terminal mass fractions:
volatiles:  0.0000000000E+00
char     :  0.4777796101E-02
water    :  0.0000000000E+00
ash      :  0.9952222109
Supplied power:  652.4010010
Supplied fraction of power:  0.2875452638
Unburnt char mass flow  [kg/s]: 0.1148258448E-06
Converted char mass flow [kg/s]: 0.8489317406E-04
Final-to-initial volume ratio:  0.2209709734
Final particle temperature [K]: 2160.000488 288.0000000
path termination cause:
  particle burnout

Path number  2
Particle surface area:  0.8088752627E-02 mm^2
Particle volume      :  0.6862298324E-04 mm^3
Equivalent spherical diameter (area):  0.5074179545E-01 mm
Equivalent spherical diameter (volume):  0.5081045628E-01 mm
Single particle and trajectory mass flow [micrograms]:  0.1029344741E-01 528000.0
Trajectory number flow:  51294768.00
Projected area ratio:  1.035291076
Minor axis:  0.2510000020E-01
Aspect ratio:  1.036000013
Superelliptic exponent:  2.000000000
Initial block and cell:  5 9 9 2 0
Initial velocity:  16.20000076 0.0000000000E+00 0.0000000000E+00
Available char mass flow [kg/s]:  0.8500799595E-04 0.8500800323E-04
```

```
number of executed iterations:  12587
number of wall collisions:  0
total residence time [s] :  0.8359638974E-02
final position [m]:  0.3827108443 -0.2280296199E-01 -0.4222273454E-01
final cell number and type:  9 3 8 10 0
final velocity [m/s]:  19.72302055 -2.029853344 -0.8927672505
terminal mass fractions:
volatiles:  0.0000000000E+00
char     :  0.4192147404E-02
water    :  0.0000000000E+00
ash      :  0.9958078265
Supplied power:  651.5134888
Supplied fraction of power:  0.2871541083
Unburnt char mass flow  [kg/s]: 0.1006915724E-06
Converted char mass flow [kg/s]: 0.8490730397E-04
Final-to-initial volume ratio:  0.2208411396
Final particle temperature [K]: 2160.000488 288.0000000
path termination cause:
  particle burnout
```

⋮

```
Path number  1249
Particle surface area:  789.7787476 mm^2
Particle volume      :  956.7001953 mm^3
Equivalent spherical diameter (area):  15.85542107 mm
Equivalent spherical diameter (volume):  12.22222710 mm
Single particle and trajectory mass flow [micrograms]:  143505.0312 1056000.000
Trajectory number flow:  7.358626842
Projected area ratio:  12.65003872
Minor axis:  2.483999968
Aspect ratio:  9.959983826
Superelliptic exponent:  100.0000000
Initial block and cell:  9 8 11 2 0
Initial velocity:  16.20000076 0.0000000000E+00 0.0000000000E+00
Available char mass flow [kg/s]:  0.1700160065E-03 0.1700160210E-03
number of executed iterations:  115075
number of wall collisions:  0
total residence time [s] :  2.764646769
final position [m]:  13.56504631 0.5344035625 -0.2834555209
final cell number and type:  27 11 8 27 7
final velocity [m/s]:  5.454840660 1.918565989 3.415004969
terminal mass fractions:
volatiles:  0.7048959732
char     :  0.1619717628
water    :  0.8744136989E-01
ash      :  0.4569092765E-01
Supplied power:  13.17882347
Supplied fraction of power:  0.2904278459E-02
Unburnt char mass flow  [kg/s]: 0.1695787505E-03
```

```
Converted char mass flow [kg/s]: 0.4372433580E-06
Final-to-initial volume ratio:  0.9979949594
Final particle temperature [K]: 559.9140015 288.0000000
path termination cause:
  particle exit at outlet

Path number  1250
Particle surface area:  796.4337769 mm^2
Particle volume      :  967.9166260 mm^3
Equivalent spherical diameter (area):  15.92208385 mm
Equivalent spherical diameter (volume):  12.26980114 mm
Single particle and trajectory mass flow [micrograms]:  145187.5000 1056000.000
Trajectory number flow:  7.273353577
Projected area ratio:  12.67547894
Minor axis:  2.492000103
Aspect ratio:  9.980015755
Superelliptic exponent:  100.0000000
Initial block and cell:  9 8 11 2 0
Initial velocity:  16.20000076 0.0000000000E+00 0.0000000000E+00
Available char mass flow [kg/s]:  0.1700159919E-03 0.1700159773E-03
number of executed iterations:  114216
number of wall collisions:  0
total residence time [s] :  2.287548304
final position [m]:  13.56503773 0.5596352816 -0.2355963886
final cell number and type:  27 11 9 27 7
final velocity [m/s]:  4.599384308 1.718347430 3.937902451
terminal mass fractions:
volatiles:  0.7070158720
char     :  0.1608348191
water    :  0.8679804951E-01
ash      :  0.4535122961E-01
Supplied power:  10.53363609
Supplied fraction of power:  0.2321346430E-02
Unburnt char mass flow  [kg/s]: 0.1696497056E-03
Converted char mass flow [kg/s]: 0.3662843824E-06
Final-to-initial volume ratio:  0.9983204603
Final particle temperature [K]: 526.8828125 288.0000000
path termination cause:
  particle exit at outlet

****************************************
Calculation Statistics
 paths exitting at outlet :     148( 1.18%)
 abnormally terminated paths:      190( 1.52%)
  paths exceeding max. wall collisions:       0(  .00%)
----------------------------------------
 Combustion statistics - average values
----------------------------------------
Char converted to CO  [kg/s]:  0.1414996982
Char converted to CO2 [kg/s]:  0.4755403847E-02
Total char conversion [kg/s]:  0.1462551057
Total unburnt char    [kg/s]:  0.4943047091E-01
```

```
Total char mass flow  [kg/s]:  0.2125200033
Fraction unburnt carbon     :    .233
Power contributed from particles [MW]: 1.317515373
Available power at complete burnout  [MW]: 36.16111374
Available power from het. combustion [MW]: 5.672159195
Fraction of power from het. combustion:  0.2321380675
Power distribution:
  Heterogeneous combustion
     Remains in particle [kW]:  84.20327759
     Directly to gas [kW]    :  1087.367920
  Devolatilisation [kW]      :  616.9478149
  Convection [kW]            :  -0.6280276775
Total energy exchange [W]:  -0.6655531418E+12
Volatile mass flow [kg/s]:  0.8732492924 0.8557428718
H2O mass flow [kg/s]:       0.1049387306 0.1043439656
CO  mass flow [kg/s]:       0.3634165227 0.3634165227
CO2 mass flow [kg/s]:       0.1865113340E-01 0.1865113340E-01
O2 consumption [kg/s]:      -0.2211512327 -0.2211512327
Volume occupied by particles [m3]: 2.258356571
total calculation time [s]:  42987.53125
```

Appendix I

List of publications and presentations

Zachariassen, A. and L. Rosendahl (1994, June). Numerical modelling of particle combustion - a computer model of multidimensional reacting gas-particle flows. Master's thesis, Institute of Energy Technology, Aalborg University, Denmark.

Rosendahl, L., A. Zachariassen, T. Condra, and P.A. Jensen (1994). Numerical modelling of multi-dimensional gas-particle reacting flows in industrial furnaces. In *Proceedings of the Second CFDS International User Conference*, pp 85-94, 8.19 Harwell, Didcot, Oxfordshire OX11 0RA, UK, December 1994. Computational Fluid Dynamics Services, AEA Technology plc.

Rosendahl, L. (1995, October) Modelling of biomass combustion. Presentation at the STVF Combustion Seminar, Institute of Energy Technology, Aalborg University.

Rosendahl, L. (1995, November) On numerical modelling of particle combustion. In R. Larsson and N.-E- Wiberg (Eds.), *NSCM VIII - the Eighth Nordic Seminar on Computational Mechanics*, Gothenburg, Sweden.

Rosendahl, L. and T. Condra (1996, August). A new basis for the description of the dispersed phase in gas-particle systems. The 19th International Congress on Theoretical and Applied Mechanics (ICTAM), Kyoto, Japan. (Also in: IONES no 10, October 1996)

Rosendahl, L. (1996, August). Analysis of combi-burner for coal and straw using FLUENT - Using FLUENT to prepare experimental campaigns at ENEL-CRT. Technical report, ENEL-CRT, Centro Riserca Termica, Pisa, Italy.

Rosendahl, L. (1996, September) Using Computational Fluid Dynamics as a tool in biomass and waste combustion Analysis. In *Proceedings of The Finnish- Swedish Flame Days (IFRF)*, Naantali, Finland.

Rosendahl, L. and T. Condra (1996, October). Tracking non-spherical particles in combustion systems. In *NSCM IX The Ninth Nordic Seminar on Computational Mechanics*, Copenhagen, Danmark.

Rosendahl, L. (1996, October) Using the CFX Fortran User Interface to model non- spherical particles in furnace geometries. In *Third CFX International Users Conference*, pp 459-475. 8.19 Harwell, Didcot, Oxfordshire OX11 0RA, UK. Computational Fluid Dynamics Services, AEA Technology plc.

Kær, S., K. Nielsen, T. Condra, L. Rosendahl and H. Widell (1996, October). Numerical modelling of non-reacting and reacting non-swirling methanol sprays. In *Third CFX International Users Conference, London, UK*, pp 429-442, 8.19 Harwell, Didcot, Oxfordshire OX11 0RA, UK. Computational Fluid Dynamics Services, AEA Technology plc.

Rosendahl, L., S. Kær and T. Condra (1997, October). Verifying empirical correlations of superelliptic particle lift and drag characteristica using CFD. In *NSCM X - the Tenth Nordic Seminar on Computational Mechanics*, pp. 247-250. Tallinn, Estonia.

Rosendahl, L. (1997, October). Qualitative CFD and experimental prediction of the aerodynamic properties of superelliptic particles. In *Fourth CFX International Users Conference, Chicago, USA*, pp 210-215 , 8.19 Harwell, Didcot, Oxfordshire OX11 0RA, UK. Computational Fluid Dynamics Services, AEA Technology plc.

Rosendahl, L. (1998, May). Numerical prediction of non-spherical particles. Workshop on Experimental and Numerical Modelling of Pneumatic Particle Transport, 27-28 May 1998, Dept. of Mechanical Engineering, The University of Edinburgh, Scotland.

Kær, S., L. Rosendahl and P. Overgaard (1998, September). Numerical analysis using complex particle formulations of a full-scale utility boiler co-firing coal and straw at MIDTKRAFT ENERGY COMPANY, Denmark. Proceedings of the Fourth European Computational Fluid Dynamics Conference, 7-11 September, Athens, Greece. K.D. Papailiou, D. Tsahalis, J. Priaux, C. Hirsch, M. Pandolfi (Eds.), John Wiley & Sons, Chichester 1998, Vol.1, Part 2, September 1998, pp. 1194-1199.

Andersen, C.F., J.B. Christiansen, B.B.B. Jensen, S.K. Kær and L. Rosendahl. Simulation of biomass combustion - Alternative idea of modelling large particles. Poster session at "Numerical Simulation of Industrial Flows", San Feliu de Guixols, Spain, October 1998.

Submitted for publication

Rosendahl, L. Using a multi-parameter particle shape description to predict the motion of non-spherical particle shapes in swirling flow. Submitted for publication in Applied Mathematical Modeling, April 1997.